QUANTUM COMPLEXITY: QUANTUM MUTUAL INFORMATION, COMPLEX NETWORKS, AND EMERGENT PHENOMENA IN QUANTUM CELLULAR AUTOMATA

by

David L. Vargas

© Copyright by David L. Vargas, 2016

All Rights Reserved

A thesis submitted to the Faculty and the Board of Trustees of the Colorado School of Mines in partial fulfillment of the requirements for the degree of Master of Science (Applied Physics).

Golden, Colorado

Date _____

Signed: _____
David L. Vargas

Signed: _____
Dr. Lincoln D. Carr
Thesis Advisor

Golden, Colorado

Date _____

Signed: _____
Dr. Jeff A. Squier
Professor and Head
Department of Physics

ABSTRACT

Emerging quantum simulator technologies provide a new challenge to quantum many body theory. Quantifying the emergent order in and predicting the dynamics of such complex quantum systems requires a new approach. We develop such an approach based on complex network analysis of quantum mutual information. First, we establish the usefulness of quantum mutual information complex networks by reproducing the phase diagrams of transverse Ising and Bose-Hubbard models. By quantifying the complexity of quantum cellular automata we then demonstrate the applicability of complex network theory to non-equilibrium quantum dynamics. We conclude with a study of student collaboration networks, correlating a student's role in a collaboration network with their grades. This work thus initiates a quantitative theory of quantum complexity and provides a new tool for physics education research.

We find that network density, clustering coefficient, disparity, and Pearson R correlation show systematic finite size scaling towards critical points of the transverse Ising model and the Bose-Hubbard model. Using matrix product state methods we are able to simulate lattices of hundreds of qubits, allowing us to verify the critical point of the transverse Ising model to within 0.001% of its known value. Furthermore, we find that complex network analysis identifies the Berezinskii-Kosterlitz-Thouless critical point of the Bose-Hubbard to within 3.6% of its accepted value. Finally, we identify the boundary separating the Mott Insulator phase from a superfluid phase in the Bose-Hubbard model by extremizing network density, clustering coefficient, and disparity.

After studying the static properties of quantum many body systems, we study the entanglement and complexity generated by Hamiltonian based quantum cellular automata. In quantum cellular automata one defines a set of local rules that govern the evolution of the quantum state. A site in a quantum lattice evolves if the set of sites around it are in certain

configurations. Configurations are defined in terms of the number of sites in the "alive" state about a site. We quantify entanglement in terms of the central bond entropy, and complexity in terms of persistent fluctuations of the central bond entropy, complex network measures of quantum mutual information networks far from their values for random/well known quantum states, and robust dynamical features. These Hamiltonians are a generalization of the Bleh, Calarco, Montangero Hamiltonian. Before beginning our study of the entanglement and complexity generated by these Hamiltonians we first perform a convergence analysis of the dynamics of the Bleh, Calarco, Montangero Hamiltonian using an open source matrix product state code, Open Source Matrix Product States. We find that the Bleh, Calarco, Montangero Hamiltonian rapidly saturates the entanglement cutoff of Open Source Matrix Product States for all initial conditions studied and is thus not a viable numerical method for studying the dynamics of quantum cellular automata. We conclude our convergence study with a case study of an emergent quantum blinker pattern also observed in exact simulation and a case study of a nearest neighbor quantum cellular automata. We conclude that while for generic initial conditions Open Source Matrix Product States is unable to meet its internal convergence criteria, for particular initial conditions and quantum cellular automata it is able to provide reliable estimates of entanglement and complexity measures. The failure of OpenMPS to provide reliably converged quantum states leads us to study our quantum cellular automata using a Trotter-based time evolution scheme.

We quantify the entanglement and complexity generated by 13 next-nearest neighbor quantum cellular automata. We also define Goldilocks rules, rules that produce activity at a site if there are exactly the right number of alive sites in the neighborhood of a site, not too few, not too many. We identify a Goldilocks rule, rule 4, as the best complexity-generating rule out of the 13 rules tested, verifying our hypothesis that only Goldilocks rules are complexity generating. We also find that non-Goldilocks rules tend toward thermalization as quantified by reduced fluctuations in the central bond entropy. We find that both highly entangled quantum states and lowly entangled quantum states have complex structure in

their quantum mutual information adjacency matrices.

Finally, in keeping with the strong physics education research focus at the Colorado School of Mines, we apply complex network analysis to a key issue germane to the student experience, namely student collaboration networks. We compute nodal centrality measures on the collaboration networks of students enrolled in three upper-division physics courses at the Colorado School of Mines. These are networks in which links between students indicate assistance with homework. The courses included in the study are intermediate classical mechanics, introductory quantum mechanics, and intermediate electromagnetism. We find that almost all of the measures considered correlate with analytical homework grades. In contrast only *net out-strength* correlates with exam grade. The benefits of collaboration do not extend from homework to exams, and students who help more than they are helped perform well on exams. Centrality measures between simultaneous collaboration networks (analytical vs. numerical homework collaboration) composed of the same students correlate with each other. Students take on similar roles in response to analytical vs. numerical homework assignments. Changes in collaboration across semesters are also considered as students transition from classical mechanics in the fall to quantum mechanics and electromagnetism in the spring. We find the most frequent transition is that students that help many others and have high grades will continue to help many others and have high grades. Students that help few more frequently transition from low grades to high grades than students that help many.

TABLE OF CONTENTS

LIST OF FIGURES AND TABLES

LIST OF SYMBOLS

A quantum state	$\|\psi\rangle$
The number of sites in a lattice or nodes in a network	L
Density matrix	$\hat{\rho}$
A Hilbert space	$\mathcal{H}$
Linear operators on $\mathcal{H}$	$\mathcal{L}(\mathcal{H})$
Single-site density matrix	$\hat{\rho}_i$
Two-site density matrix	$\hat{\rho}_{ij}$
Single-site von Neumann entropy	S_i
Two-site von Neumann entropy	S_{ij}
Central bond entropy	S_{bond}
Quantum mutual information matrix	$\mathcal{I}$
Quantum mutual information between two sites	$\mathcal{I}_{ij}$
Adjacency matrix	A
Entry of an adjacency matrix	A_{ij}
A set of nodes	V
A set of links	E
A network	G
A Hamiltonian	$\hat{H}$
A rule operator	$\hat{R}_i$
Rule number of Hamiltonian-based quantum cellular automata	R

Projector onto subspace in which site i has n neighbors in the alive state for a QCA of radius r . . . . . $\mathcal{N}^{(i),r}$

Hadamard gate . . . . . $\hat{H}_D$

Phase shift gate . . . . . $\hat{P}(\theta)$

Rule number of unitary-base quantum cellular automata . . . . . S

Number of singular values kept in a singular value decomposition of a quantum state . χ

Energy variance tolerance in Open Source Matrix Product State Code . . . . . ϵ_v

Singular value tolerance in Open Source Matrix Product State Code . . . . . ϵ

Maximum number of singular values kept by Open Source Matrix Product State Code . . . . . $\chi_{\max}$

Out-strength . . . . . s_i^{out}

In-strength . . . . . s_i^{in}

Network density . . . . . D

Disparity . . . . . Y

Out-disparity . . . . . Y^{out}

In-disparity . . . . . Y^{in}

Clustering coefficient C

Local clustering coefficient . . . . . c^L

Pearson R similarity . . . . . R

Closeness centrality . . . . . c^C

Harmonic centrality . . . . . c^H

Betweenness centrality . . . . . c^B

Time . . . . . t

Final time . . . . . t_f

Time step . . . . . Δt

Sum of analytical homework grades for course in classical mechanics . . . . . G_A^{CM}

Sum of numerical homework grades for course in classical mechanics . . . . . G_N^{CM}

Sum of homework and exam grades for course in classical mechanics . . . . . G_T^{CM}

Sum of homework and exam grades for course in quantum mechanics . . . . . G_T^{QM}

Sum of homework and exam grades for course in electromagnetism . . . . . G_T^{EM}

Analytical collaboration network for course in classical mechanics . . . . . A_A^{CM}

Numerical collaboration network for course in classical mechanics . . . . . A_N^{CM}

Total collaboration network for course in classical mechanics . . . . . A_T^{CM}

Total collaboration network for course in quantum mechanics . . . . . A_T^{QM}

Total collaboration network for course in electromagnetism . . . . . A_T^{EM}

LIST OF ABBREVIATIONS

Transverse Ising Model	TIM
Bose-Hubbard Model	BHM
Berezinskii-Kosterlitz-Thouless	BKT
Quantum Cellular Automata	QCA
Bleh, Calarco, Montangero	BCM
Open Source Matrix Product States	OpenMPS
Carr Theoretical Physics Research Group	CTPRG
Matrix product state	MPS
Alternate mode of unitary-based quantum cellular automata	ALT
Greenberger-Horne-Zeilinger	GHZ
Superfluid	SF
Mott insulator	MI
First derivative	FD
Second derivative	FD
Local minima	LM
Local maximum	LMA

ACKNOWLEDGMENTS

Thank you to my family for their love and support. The love of my family is what has allowed me to endure the difficult times during my degree. I also thank my advisor Lincoln Carr for his constant encouragement, positive energy, and thoughtful criticism. Next, I thank Cecilia Behn, Pat Kohl, and Eric Toberer for serving as members of my committee. My committee's critique of my presentation skills and thesis greatly improved both. I have had countless conversations with members of the Carr Theoretical Physics Research Group, and they have shaped my view of physics. I enjoyed arguing about the subtleties of entanglement with Daniel Jaschke, and I am grateful for Gavriil Shchedrin's constant insistence on understanding the physical meaning of calculations. I thank Diego Alcala for his reassurances and his perspective on life as a graduate student. I thank Marie Patton-McLain for her constant positive energy, her skeptical encouragement, and for submitting my paperwork to the graduate school when I had to fly away to Maryland. Next, I thank Michael Wall for his implementation of Open Source Matrix Product States. I would also like to thank Nicole Halpern, Ning Bao, Patrick Rall, Simone Montangero, and Logan Hillberry for conversations on quantum cellular automata. I am particularly grateful to Logan Hillberry for the quantum cellular automata code he developed. I thank Monika Schleier-Smith for sharing her ideas on the implementation of quantum cellular automata in experiment. I am grateful to Assistant Dean Jahi Simbai for granting me a graduate fellowship that enabled me to pursue my master's degree without incurring debt and to Fernando Guzman for advocating me receiving this fellowship. Thank you to Andrea Salazar for seeing something in a high school senior not sure of his next steps in life, and for providing another perspective on my trajectory through Mines. Finally, I am deeply grateful to Dean Tina Voelker for her help. Dean Voelker reached out to me and helped me coordinate the final submission of my thesis. Thank you again Dean Voelker.

Great fleas have little fleas upon their backs to bite 'em,

And little fleas have lesser fleas, and so ad infinitum.

-Augustus de Morgan

CHAPTER 1
INTRODUCTION

Complexity is a difficult concept to define. There are precise definitions of complexity. For example, the authors of [1] adapt concepts from theoretical computer science in order to provide a definition of complexity. However, much research now advocates identifying features of complexity rather than trying to provide a single definition of the concept. Such features include systems with a hierarchy of scales like the food webs of the Coachella Valley [2], in which predator-prey relationships are modeled at multiple trophic levels. The interconnections of the internet also have a hierarchical structure, with a global structure connecting local networks [3]. Both of these systems consist of many interacting components that are connected in intricate ways [4]. The interconnections and interdependencies of such systems make them very difficult to predict and control, as described in [5, 6].

Conventional studies of single particle quantum mechanics typically assume that only a few degrees of freedom interact. The success of this assumption for single particle quantum systems has made quantum theory one of the most quantitative and predictive theories of modern science [5]. For example the spectra of the Hydrogen atom can be accurately predicted by only considering the interaction between a single electron and a single proton, in isolation from the rest of the universe. There have also been successful theories of quantum many body physics, for example Heisenberg models describing antiferromagnetism. Heisenberg models describe interacting spins on a lattice in the presence of a magnetic field. The spins of the Heisenberg model are all identical two-dimensional quantum systems. However, generic quantum many body systems may involve the interactions of many different types of atoms or molecules. There may also be no clear distinction between the system and its environment. Furthermore, the structure of the interactions between particles need not be a simple lattice and may instead take the form of a *complex network* [4, 7]. Already quantum

simulator technologies based on ultracold molecules [8], trapped ions [9], and Rydberg gases [10] have been developed that couple the degrees of freedom of hundreds of individual quantum systems. As we move towards more and more complex quantum systems, involving a hierarchy of scales, diverse interacting components, and a structured environment, we expect to observe long-lived dynamical features, fat-tailed distributions, and other key identifiers of complexity [11, 6, 12]. How are we to synthesize and understand the data from these emerging complex quantum systems?

Systems like the food webs of the Coachella Valley and the internet are often studied within the field of *complex network theory*. A *network* is any system that consists of a collection of individual objects that have connections to each other. The individual objects are termed *nodes*, and nodes are connected by *links*. The various species of the Coachella Valley are the nodes of its corresponding network, and the predator-prey relationships are the links between nodes. The internet can be represented as a network by considering individual computers as nodes, and the wires connecting them as links. A useful representation of a network is its *adjacency matrix*. In the adjacency matrix entries are numbered by the nodes in the network and weighted according to the links between these nodes [4]. Complex network theory quantifies the structure of complex networks via measures on the adjacency matrix. Complex network measures like *network density*, *clustering coefficient*, and *disparity* have allowed researchers to quantify the non-random structure of social networks and the existence of backbone structures in chemical reaction networks [13, 14]. Complex networks have been studied in the context of quantum systems [15, 16, 17, 18, 19]. For instance studies have been conducted that "rewire" the couplings defining the Bose-Hubbard model and the transverse Ising model, structuring the couplings in their Hamiltonians as *small world networks* (as social networks are structured), and examining the modifications to finite temperature and mean field quantum phase diagrams [20, 21, 22]. Our work focuses on utilizing and developing complex network measures as new tools to quantify the emergence of complexity in quantum many body systems. We identify *quantum mutual information* as an effective

choice for the adjacency matrix of our studies. Quantum mutual information has been shown to be a measure of the quantum and classical correlations present between two subsystems [23], and is bounded from below by any possible two point correlator [24]. By computing complex network measures on quantum mutual information networks we provide a succinct description of the structure of correlations in quantum systems. Furthermore, classical mutual information, the classical analog of quantum mutual information, is a well-established and useful tool in complex network based diagnostics of the brain [25]. Finally, independently of complex network theory, *information theory* forms the basis of many quantifications of complexity [1, 12, 26].

Information is a measure of the average unexpectedness of measurement outcomes. For instance, if one flips a fair coin, where the probabilities of heads and tails are equal, one is maximally surprised by the result. Compare this to a biased coin where the probability of heads is equal to 0.9, and the probability of tails is equal to 0.1. Most flips of this coin will result in heads, which is the less surprising result, however occasionally the result will be tails, the more surprising result. Another way to state this is that information quantifies how much we learn on average by repeated measurements of random events. The definition of information is very general, and so it is applicable to many different systems. *Mutual information* is a measure of the correlations between events. It is defined in terms of the shared information of independent systems. That is, one may compare the measurement results of simultaneously flipping two coins and find that the result of one coin tends to predict the result of the other. Both information and mutual information have been used as complexity measures in classical complex systems, for instance [27] applies both to quantify the complexity of classical cellular automata. Mutual information has also quantified the correlation between voltages of different regions of the brain predicted by simulations as in [25]. Furthermore information theory has been used to quantify complexity of arbitrary data, for instance [26] defines complexity in terms of an entropy defined over the probability of an epsilon machine being in a particular causal state. An epsilon machine predicts the data

that it will observe in measurement via a model it constructs. This model consists of causal states and transitions between these causal states. The transition between causal states of an epsilon machine results in the emission of data. This data is the epsilon machine's prediction of the data it will observe in experiment. Other researchers have also defined complexity in terms of entropies over ensembles of data [12].

Our work does not focus on providing a precise definition of complexity, rather we quantify an important aspect of complexity, connectivity, by studying the structure of quantum mutual information complex networks. Our complex network based approach does not define a single scalar measure of complexity, rather different complex network measures characterize different aspects of the structure of correlations of quantum mutual information networks. Furthermore, by considering all two-point correlations simultaneously one can define order parameters for non-translationally invariant systems, for example of the kind described in [28]. This is particularly useful for studying simulations of quantum dynamics where the entanglement may become clustered or localized to a particular region. Complex network analysis thus gives a more complete description of quantum many body states than has been studied previously.

In Chapter 4 we quantify the ability of complex network measures to detect emergent phenomena in quantum systems by applying them to reproduce the known quantum phase diagrams of the transverse Ising and Bose-Hubbard models. We emphasize that both these models are studied heavily in quantum simulator experiments and are standard workhorses of quantum many body physics [29, 8, 9, 30, 31]. Quantum phase transitions are collective phenomena, in which an entire quantum many body ground state undergoes an abrupt change at a quantum critical point. In classical systems phase transitions are often driven by temperature. For instance as temperature is increased ice melts into water and water evaporates into steam. However quantum phase transitions occur at absolute zero temperature. Instead of temperature, the phase transition is induced by magnetic fields or quantum mechanical tunneling of particles in optical lattices [32, 33]. The transverse Ising model is

a model of 1-D ferromagnets like $CoNb_2O_6$ [32]. Moreover the emphasis in quantum phase transitions is on second-order transitions, which exhibit an abrupt change in the correlation structure: for instance, a correlation length may diverge at a critical point. The transverse Ising model consists of interacting spins on a 1-D lattice in the presence of an external magnetic field. The spins minimize energy by aligning their spins with their nearest neighbors, thus forming a ferromagnet. However as the external magnetic field grows in strength it tends to align the spins perpendicularly to the axis of magnetization, disordering the spins with respect to this axis due to the Heisenberg uncertainty principle. This disorder results in a quantum phase transition from a ferromagnet to a quantum paramagnet at a particular strength of the external field, with an accompanying change in correlation structure [34]. The Bose-Hubbard model can be realized by atoms trapped in 1-D optical lattices [33]. These lattices are standing waves of light. The troughs or peaks of these waves form potential wells in which atoms are trapped. By tuning the properties of such lattices experimentalists can change the depth of the potential well allowing atoms to tunnel between nearest neighboring wells [35]. As the particles become more free to move about the 1-D lattice they undergo a transition to a superfluid in which all atoms occupy the same delocalized single particle state [35].

Conventionally quantum phase transitions are studied via an order parameter defined in terms of local observables, or in terms of long range correlations. Recent work has shown that entanglement measures like concurrence, von Neumann entropy, and quantum mutual information can identify quantum phase transitions [36, 37, 38]. Note that we refer to quantum mutual information as an entanglement measure since if the entire system is in a pure quantum state non-zero quantum mutual information between any two subsystems implies the pure quantum state is entangled. However, this does not necessarily imply entanglement amongst the subsystems, since quantum mutual information quantifies both quantum and classical correlation amongst subsystems [39]. Since entanglement measures like quantum mutual information are non-local, they characterize the collective response of

quantum systems to external perturbations. Furthermore, entanglement measures are not defined in terms of any particular observable and so they have been used to identify quantum phase transitions in both transverse Ising and extended Hubbard models. However, no work has yet considered the quantum mutual information between all lattice sites simultaneously. By studying quantum mutual information complex networks we summarize the collective and emergent response of quantum many body systems as they undergo quantum phase transitions.

Having established the ability of complex network measures to detect emergent phenomena in quantum many body systems, in Chapter 6 we quantify the complexity generated by Hamiltonian-based quantum cellular automata (QCA). These quantum cellular automata are generalizations of the Bleh, Calarco, and Montangero (BCM) Hamiltonian introduced in [40]. Quantum cellular automata are inspired by classical cellular automata like Conway's game of life [41], in which simple rules govern the evolution of a two-dimensional grid of cells. Considering the possibility that simple quantum-mechanical rules could simulate arbitrary quantum systems lead Feynman to propose the possibility of a universal quantum computer in [42], initiating the field of quantum computation. The simple rules of Conway's game of life give rise to remarkably complex patterns, like blinkers that oscillate at a fixed position, gliders that travel across the grid, and even universal computers [43]. Besides generating complexity, classical cellular automata have also been developed to model phenomena as diverse as surface growth, percolation, forest fires, Ising spin dynamics, traffic, and strings [44]. Since simple rules give rise to complex dynamics in these classical automata, one may expect that quantum cellular automata will also give rise to complex dynamics. We both confirm and constrain this expectation in Chapter 6 by identifying multiple rules that give rise to complexity. Complexity is quantified by robust emergent dynamics, quantum states far from known/random states, and persistent fluctuations of the central bond entropy. In [45], rule 6 (out of 16 reversible nearest-neighbor 1D rules) was identified as the only rule that generated robust and complex dynamics as we quantify in chapter 6. Rule 6 belongs to

a class of rules known as *Goldilocks rules*. Goldilocks rules are rules that produce dynamics when there are just the right number of sites in the neighborhood of a site, not too few, and not too many. Extending the work of [45] to Hamiltonian next-nearest neighbor QCA we hypothesize that only Goldilocks rules will be complexity generating. Furthermore, we hypothesize that non-Goldilocks rules tend towards thermalization as quantified by reductions in entropy fluctuations. Unlike classical mechanics, in quantum mechanics entanglement becomes possible. Therefore in Chapter 6 we also study the relationship between entanglement and complexity, addressing the question, "Is complexity lowly, highly, or both lowly and highly entangled?" Such questions of entanglement determine the ability to follow the dynamics of such systems on classical computers: in other words, is a quantum computer required to study quantum cellular automata in no, few, many, or all circumstances? They also help us to understand how quantum complexity limits to classical complexity, as there may be features of quantum complexity that are only present in highly entangled systems.

This work will make use of tensor network methods (different than complex network methods) to efficiently simulate on a classical computer the exponentially large Hilbert spaces that arise in the study of quantum many body systems. Tensor network methods rely on the singular value decomposition as a method of data compression on the quantum state [46]. They allow us to find ground states and time evolved states under various Hamiltonians for hundreds of lattice sites. Tensor network methods therefore go beyond exact diagonalization methods which are only capable of simulating approximately thirty qubits due to the memory required to store the quantum state. Such methods also allow for the efficient computation of local observables and two-point correlators. An important limitation of tensor network methods is that they are only able to efficiently represent quantum states that obey an area law. These are quantum states that have entropy of subsystems proportional to the boundary of those subsystems; in nature, we find such area laws for instance for black holes, where entropy is contained on the surface, not in the interior [47]. Since the ground states of many physical many body Hamiltonians obey an area law [48], we are able to conduct our

study of quantum phase transitions in Chapter 4 using an open source matrix product state code, Open Source Matrix Product States (OpenMPS) [49]. This code is formulated in terms of tensor networks and is written and maintained by former and current group members of the Carr Theoretical Physics Research Group (CTPRG). Using OpenMPS we compute both local and non-local observables, as well as measures from quantum information theory like quantum mutual information. Thus OpenMPS enables us to study systems consisting of 100's of spins and 100's of particles in Chapter 4.

While tensor network methods have been successful in the study of physically motivated quantum states, like the ground states of transverse Ising and Bose-Hubbard Hamiltonians, before this thesis there have been no systematic convergence studies of the dynamics generated by Hamiltonian-based quantum cellular automata using tensor network methods. Therefore in Chapter 5 we test whether the BCM Hamiltonian (a quantum cellular automata) can be efficiently simulated using OpenMPS. We demonstrate that OpenMPS is not capable of efficiently simulating the dynamics generated by the BCM Hamiltonian for arbitrary initial states because for nearly all of the initial conditions we study the BCM Hamiltonian generates too much entanglement. Since OpenMPS is not able to accurately represent these highly entangled quantum states we study the entanglement dynamics of Hamiltonian-based quantum cellular automata in Chapter 6 using a Trotter-Exact time evolution scheme. We conclude Chapter 5 with two case studies. In a case study of a quantum blinker pattern we find that OpenMPS is able to accurately compute complex network measures and the frequency and amplitude of fluctuations of the central bond entropy. Although typical initial conditions result in dynamics too highly entangled for OpenMPS to accurately simulate, this single exceptional initial condition produces dynamics that OpenMPS is able to accurately follow. Next in chapter 5 we perform a case study of a Hamiltonian version of rule 6 of [45]. We find that in contrast to the BCM Hamiltonian, the rule 6 Hamiltonian does not generate highly entangled states, at least for a single initial condition. These two case studies set the stage for the more detailed study of Chapter 6 where we quantify the complexity and

entanglement generated by 13 Hamiltonian-based QCA.

Finally, Chapter 7 of this thesis applies complex network theory to student collaboration networks (SCN), as an application of complex network methods to physics education research, an important focus of the physics department at the Colorado School of Mines and the CTPRG. Our study of SCN focuses on how the importance of a student to the structure of SCN correlates with a student's performance in coursework. Correlating nodal centrality measures with student grades allows us to evaluate whether well-connected students have good grades, and our attention to homework vs. exam grades allows us to study how collaboration impacts student grades when students are with and without their collaborators. Furthermore, we quantify how students collaboration strategies change between semesters, and observe how this relates to changes in the grades of students between semesters. Many of these ideas seem straightforward, however hardly any work has been done to understand the influence of student collaboration on student grade, we know of only one prior work [50]. By applying the new tool of complex network theory to student collaboration networks we offer new

By applying complex theory to both static and dynamic quantum mutual information networks we provide new tools for the analysis of complex quantum systems. Our proof of principle study of the ground state properties of the transverse Ising and Bose-Hubbard models establishes the relevance of complex network theory to quantum systems. By quantifying the complexity of quantum cellular automata we show that complex network analysis is also an effective approach to analyzing equilibrium quantum dynamics. Our complex network based approach also allows us to quantify how a student's role in a student collaboration network correlates with their grades. While the collaboration of students on quantum mechanics homework seems to have nothing to do with quantum mechanics itself, our work demonstrates that complex network theory presents a common approach to studying such disparate systems. Finally, in the appendix we provide a derivation suggesting a future direction for research, continuous quantum games of life.

CHAPTER 2
FROM INFORMATION THEORY TO TIME EVOLUTION METHODS: THEORETICAL TOOLS

In this chapter we introduce the theoretical tools that will be used in the remaining chapters. We start by defining the term information within the context of classical information theory and show how this connects to quantum information theory via von Neumann entropy. We also introduce complex network theory and demonstrate how it may used to study networks of quantum mutual information. Next we provide a brief discussion of quantum phase transitions and finite size scaling theory. We then provide definitions of both continuous time Hamiltonian-based quantum cellular automata and discrete time unitary-based quantum cellular automata. The chapter concludes by describing the numerical methods behind Open Source Matrix Product States and the Suzuki-Trotter expansion used to evolve Hamiltonian-based quantum cellular automata.

2.1 Classical Information Theory

The *information* to be gained by performing measurements on a discrete random variable X with outcomes x is defined as [51]

$$S(X) = -\sum_{x} p(x)\log(p(x)). \tag{2.1}$$

S is termed the information or entropy of the corresponding probability distribution $p(x)$. Entropy measures how random a probability distribution is. If there are N outcomes of the random variable X and all are equally likely then $S = \log(N)$ as calculated in Eq. (2.2). This is the connection of information to the entropy computed in statistical mechanics, where $S = k_B \log(\Omega)$.

$$S = -\sum_{i=1}^{N} \frac{1}{N}\log\left(\frac{1}{N}\right) = -\frac{N}{N}\log\left(\frac{1}{N}\right) = \log(N)\,. \tag{2.2}$$

The formula $S = k_B \log(\Omega)$ is therefore due to the assumption that every configuration of a thermodynamic system is equally likely.

Another way to think of information is as the average number of questions one must ask about the outcome of a random variable to uniquely identify the outcome using the most effective line of questioning. If we set the base of the logarithm to 2 then the unit of information is bits, and therefore our questions are all yes or no questions. For example, given two biased coins one may find that the probability of the first coin landing tails and the second landing tails is $p_{TT} = 0.5$. Similarly one may find that the first coin lands heads and the second coin lands heads with probability $p_{HH} = 0.5$, so that $p_{HT} = p_{TH} = 0.0$. The most effective question to determine the outcome uniquely is "Did the second coin land heads?" This will uniquely determine the state of both coins and so one always requires 1 bit to uniquely identify the state of the coins. Computing the entropy we find that

$$S = -2\frac{1}{2}\log_2\left(\frac{1}{2}\right) = 1\,. \tag{2.3}$$

The entropy formula identifies the average number of questions one must ask to identify the outcome of a random variable. Given two random variables X and Y, there may be correlations between the measurement outcomes of X and the measurement outcomes of Y. For instance, in the previous example the outcomes of the two coins are correlated. The coins always land either HH or TT, but never HT or TH. The quantity that quantifies the correlation between the measurement outcomes of two random variables is *mutual information*. Mutual information is defined as

$$I(X,Y) = S(Y) - S(Y|X) = S(X) + S(Y) - S(X,Y)\,. \tag{2.4}$$

Where $S(Y|X)$ is the conditional entropy and is defined as [51]

$$S(Y|X) = \sum_x p(x) S(Y|X=x) = -\sum_x p(x) \sum_y p(y|x)\log(p(y|x))\,. \tag{2.5}$$

Where $p(y|x) = \frac{p(y\cap x)}{p(x)}$. The conditional entropy $S(Y|X)$ is the average entropy of the random variable Y upon reconditioning of its probability distribution on the outcomes of X. The

mutual information between two random variables is maximized when $S(Y|X) = 0$. This only occurs when each outcome of X uniquely identifies the outcome of Y. The mutual information is minimized when $S(Y|X) = S(Y)$. This only occurs when the outcomes of X do not modify the probability of outcomes of Y. Therefore the mutual information between two random variables tells us how much measurements on one variable tell us about the measurements of another variable. The two coins that always land either TT or HH have 1 bit of mutual information. To compute this we must first compute marginal probability distributions of each coin. Both coins have $p_T = p_{TT} + p_{TH} = 0.5$, and $p_H = p_{HH} + p_{HT} = 0.5$. If their measurement outcomes are considered independently each have entropy $S = 1$. The mutual information between the two coins is

$$I(X,Y) = 1 + p_H \left(p_{T|H} \log(p_{T|H}) + p_{H|H} \log(p_{H|H}) \right) + p_T \left(p_{T|T} \log(p_{T|T}) + p_{H|T} \log(p_{H|T}) \right) \tag{2.6}$$

$$= 1 + 0 + 0 = 1 \,. \tag{2.7}$$

Where $0 \log(0) \equiv 0$ since $\lim_{x \to 0} x \log(x) = 0$. Mutual information quantifies the correlations between measurement outcomes on two random variables. If a system consists of many random variables with probability distribution $p_{X_1, X_2, \ldots, X_N}$, then one computes the mutual information between any two random variables by computing the marginal probability distributions p_{X_i, X_j}, p_{X_i}, and p_{X_j}, and computing S_{Xi, X_j}, S_{X_i}, and S_{X_j}.

2.2 Quantum Information Theory

In quantum theory the state of a system is an element of a Hilbert space, $|\psi\rangle \in \mathcal{H}$. We will always assume the Hilbert space can be written as a tensor product over local Hilbert spaces $\mathcal{H} = \otimes_{i=1}^{L} \mathcal{H}_i$ each spanned by a basis $\mathcal{B}_i$ and of dimension $d = \dim(\mathcal{H}_i)$. These local basis vectors correspond to the set of measurement outcomes on the local degrees of freedom. When $d = 2$ the local state of site i is spanned by the states $|0\rangle$ and $|1\rangle$. The states $|0\rangle$ and $|1\rangle$ form the standard basis for the local state space of dimension 2,

$$|\psi\rangle_i = c_0 |0\rangle + c_1 |1\rangle \,. \tag{2.8}$$

Such an object is referred to as a qubit, short for quantum bit. The basis vectors of the full quantum state are tensor products over the basis vectors of the local Hilbert spaces. As in the classical case we will define an entropy that quantifies the randomness of measurement outcomes. However in quantum mechanics the state of the system is quantified by a set of complex probability amplitudes c_i, not by a probability distribution,

$$|\psi\rangle = \sum_{i=1}^{d^L} c_i \, |i\rangle \ . \tag{2.9}$$

However for any quantum state $|\psi\rangle$ there is a corresponding density matrix $\hat{\rho} = |\psi\rangle \langle\psi| \in \mathcal{L}(\mathcal{H})$. The density matrix is a positive semi-definite operator on the Hilbert space with $\mathrm{Tr}(\hat{\rho}) = 1$. Thus the density matrix can be written as

$$\hat{\rho} = \sum_k \lambda_k \, |\psi_k\rangle \langle\psi_k| \ . \tag{2.10}$$

Where $\lambda_k \in [0, 1]$, and $\sum_k \lambda_k = 1$. One can interpret λ_k as the probability that the system is in the state $|\psi_k\rangle$. Interpreting the λ_k as probabilities one defines the von Neumann entropy of a density matrix as the entropy of its eigenvalues,

$$S(\hat{\rho}) = -\sum_{k=1}^{d^L} \lambda_k \log_d (\lambda_k) \ . \tag{2.11}$$

Note that for pure states $\hat{\rho} = |\psi\rangle \langle\psi|$, so that $S(\hat{\rho}) = 0$. As in the classical case we want to quantify the correlations between subsystems of the lattice. The state of a subsystem is computed by computing the partial trace of $\hat{\rho}$, tracing out the degrees of freedom outside of the subsystem. The partial trace is analogous to the classical procedure of computing a marginal probability distribution, it is defined linearly on $\mathcal{L}(\mathcal{H} = \mathcal{H}_\mathcal{A} \otimes \mathcal{H}_\mathcal{B})$,

$$\mathrm{Tr}_B \left(|a_i\rangle \langle a_j| \otimes |b_i\rangle \langle b_j| \right) = |a_i\rangle \langle a_j| \langle b_i| b_j\rangle \ . \tag{2.12}$$

The subscript on Tr denotes the Hilbert space to be traced out, the resulting operator $|a_i\rangle \langle a_j| \in \mathcal{H}_\mathcal{A}$. The reduced density matrix associated with a single site i is defined as the partial trace of $\hat{\rho}$ over all sites except site i,

$$\hat{\rho}_i = \mathrm{Tr}_{k \neq i} \hat{\rho} \, . \tag{2.13}$$

Similarly we may compute the state of any two site subsystem by tracing out the degrees of freedom of all sites except sites i and j,

$$\hat{\rho}_{ij} = \mathrm{Tr}_{k \neq i,j} \hat{\rho} \,. \tag{2.14}$$

The single-site von Neumann entropy is denoted as

$$S_i = S(\hat{\rho}_i) \,, \tag{2.15}$$

while the two-site von Neumann entropy is denoted as

$$S_{ij} = S(\hat{\rho}_{ij}) \,. \tag{2.16}$$

Finally, the reduced density matrix associated with the interval $[1, L/2]$ is denoted by $\hat{\rho}_{[1:L/2]} = \mathrm{Tr}_{j>L/2} \, (\hat{\rho})$. We denote the entropy of $\hat{\rho}_{[1:L/2]}$ by S_{bond},

$$S_{\mathrm{bond}} = S(\hat{\rho}_{[1:L/2]}) \,. \tag{2.17}$$

Throughout the remainder of this thesis an S with a subscript indicates the von Neumann entropy of a subsystem of a quantum lattice and not the classical entropy. In Sec. 2.6 we introduce a rule numbering scheme for the quantum cellular automata we define and denote rule numbers by the symbol S; this can always be distinguished from the von Neumann entropy of a subsystem as it never has a subscript.

The quantum mutual information between any two sites i and j is defined in terms of the entropies of the individual sites and the entropy of the sites jointly. In analogy with Eq. (2.4)

$$\mathcal{I}_{ij} = \frac{1}{2} \left(S_i + S_j - S_{ij} \right) \,. \tag{2.18}$$

The quantum mutual information is bounded from below by all equal time two point correlators defined on the degrees of freedom of sites i and j [24]. These $g^{(2)}$ correlators are measures of noise on top of the density measurement of a quantum state. For instance to measure $g^{(2)}$ in experimental measurements of matter density of a condensate one subtracts the local mean density to compute $g^{(2)} = \langle \hat{n}_i \hat{n}_j \rangle - \langle \hat{n}_i \rangle \langle \hat{n}_j \rangle$ [52]. In this thesis we multiply the quantum mutual information between any two sites by $1/2$, so that $0 \leq \mathcal{I}_{ij} \leq 1$. An

interesting subtlety in the definition of quantum mutual information is that Eq. (2.4) can be quantized in more than one way, this has led to the definition of quantum discord as defined in [53].

2.3 Complex Network Theory

A *Network* a.k.a. *Graph* is a collection of *nodes* and *links*. A graph G is denoted as follows

$$G = \{V, E\} \,. \tag{2.19}$$

Where V is the set of nodes and E is the set of links connecting nodes. In the simplest case a links is not directed, and it connects only two nodes to each other, we can summarize these facts for a particular link $E_1 \in E$ by the following equation

$$E_1 = (v_1, v_2) = (v_2, v_1) \ , \tag{2.20}$$

where v_1 and v_2 are two nodes, that is $v_1, v_2 \in V$.

A less abstract description of a network than the set of nodes and links that it consists of is the adjacency matrix of the graph. For each node in the network there is a corresponding row in the adjacency matrix, adopting some ordering of the nodes $v_1, v_2, ..., v_n$ we define $A_{ij} = 1$ if $E_k = (v_i, v_j) \in E$, and $A_{ij} = 0$ otherwise. Many real world situations can be described by networks. For example the nodes in a network can correspond to people, where the links summarize the pattern of friendship between them. In Chapter 7 we study student collaboration networks, where a link corresponds to assistance. If one student assists another student with homework a link is placed between these students. Note that this is not a symmetric relation, i helps j does not imply j helps i. This is the defining feature of a directed network, its connections are asymmetrical. Therefore, for directed networks one says that a link goes from node i to node j to indicate the direction of the link. Perhaps each node in a network represents a state of a situation ψ and each link represents the interconnection of these states under the Hamiltonian H of that physical situation. Sometimes it makes sense to say that a connection is stronger or weaker. For instance certain friendships may be weaker

or stronger than others depending on how much two people like each other. To model this we can introduce a weight to the links representing a friendship. These could be real numbers between 0 and 1, with 0 corresponding to two people without a friendship and 1 corresponding to connection between best friends. The quantum mutual information networks defined in Sec. 2.4 are of this weighted form. There the weight of a connection is a summary of the correlations between two sites. From our analysis of quantum mutual information we would like to determine the location of quantum critical points and understand whether our time evolution schemes generate a new physical class of states displaying high complexity and non-random structure. Complex network theory is a natural tool for our study because researchers have developed quantitative measures like the clustering coefficient to distinguish between random and non-random networks.

One way to define a random network is as follows: take a set of n nodes and place a link between any two of the nodes with probability p. The number of connections of a node is termed the degree of the node and is denoted by k. The network resulting from placing connections will have a Poissonian degree distribution as $n \to \infty$. The degree distribution of a network of n nodes is equal to [4]

$$p_k = \binom{n}{k} p^k (1-p)^{n-k} \approx \frac{z^k \mathrm{e}^{-p(n-1)}}{k!} \,. \tag{2.21}$$

This result helps quantify what researchers mean when they say that the connections in a network are non-random. Often complex networks have more nodes of a higher degree than would be expected by assuming that connections are formed at random. For example many networks have degree distributions that follow a power-law for large values of k. However measures like the clustering coefficient offer a more quantitative means of quantifying non-random structure than comparing probability distributions.

An example of the usefulness of scalar measures like the clustering coefficient is the development of small world networks by Watts and Strogatz. They demonstrated that their small world parameterization of complex networks could explain the high clustering and

low characteristic path length seen in social networks as compared to random networks [13]. To construct a small world network one begins by initializing a network in which c nearest neighbors are connected. One then rewires connections with a certain probability by replacing each link with a link connecting two nodes chosen uniformly at random [3]. When this probability is equal to zero one recovers the initial condition of the network, a state in which c nearest neighbors are connected. As this probability approaches 1 the network becomes a random graph. By using measures like the clustering coefficient and characteristic path length Watts and Strogatz were able to quantitatively show that many real world networks have non-random structure. They also found that this structure held implications for disease spreading and synchronization across nodes [13].

2.4 Quantum Mutual Information Networks

To understand the structure of correlations of quantum many body ground states we will study the quantum mutual information between every pair of lattice sites in 1-D quantum systems. For the systems under discussion we will always assume that $\rho = |\psi\rangle\langle\psi|$. The quantum mutual information network $\mathcal{I}$ is a subtle quantity to interpret. Let us progress by looking at examples.

2.4.1 Networks of two spins

The quantum state of two qubits can be written as

$$|\psi\rangle = c_{00}|00\rangle + c_{01}|01\rangle + c_{10}|10\rangle + c_{11}|11\rangle \ . \tag{2.22}$$

The most general state that will exhibit no correlation between two sites is

$$|\psi\rangle = (c_0|0\rangle + c_1|1\rangle)(d_0|0\rangle + d_1|1\rangle) \tag{2.23}$$

with all $c, d \in \mathbb{C}$, and all $|\cdot\rangle \in \mathcal{H}$. To construct the adjacency matrix describing the correlations between two qubits we will compute the quantum mutual information between them. All states that can be factorized into the form of Eq. (2.23) have quantum mutual information between qubits of zero, that is $\mathcal{I}_{ij} = 0$ for all i, j. Pure states that can be factorized in

this way are called product states. All other states are called entangled. Note that we set $\mathcal{I}_{ii} = 0$ by convention, although Eq. (2.18) would result in $\mathcal{I}_{ii} = S_i + S_i - S_i = S_i$. That is one learns as much about the state of the universe at position i as one would if they measured the state of the universe at position i. In contrast to product states, the spin singlet is a state of two qubits that features maximal entanglement between the two qubits. The spin singlet is

$$|\psi\rangle = \frac{1}{\sqrt{2}} \left(|01\rangle - |10\rangle \right) . \tag{2.24}$$

The density matrix $\hat{\rho}$ of the spin singlet is therefore

$$\begin{aligned} \hat{\rho} \equiv |\psi\rangle \langle\psi| &= \frac{1}{2} \left(|01\rangle - |10\rangle \right) \left(\langle 01| - \langle 10| \right) & (2.25) \\ &= \frac{1}{2} \left(|01\rangle \langle 01| - |01\rangle \langle 10| - |10\rangle \langle 01| + |10\rangle \langle 10| \right) . & (2.26) \end{aligned}$$

The reduced density matrix for the first spin is

$$\begin{aligned} \hat{\rho}_1 = \mathrm{Tr}_{i=2} \hat{\rho} &= \frac{1}{2} \left(|0\rangle \langle 0| \langle 1| 1\rangle - |0\rangle \langle 1| \langle 1| 0\rangle - |1\rangle \langle 0| \langle 0| 1\rangle + |1\rangle \langle 1| \langle 0| 0\rangle \right) & (2.27) \\ &= \frac{1}{2} \left(|0\rangle \langle 0| + |1\rangle \langle 1| \right) , & (2.28) \end{aligned}$$

and the reduced density matrix for the second spin is

$$\begin{aligned} \hat{\rho}_2 = \mathrm{Tr}_{i=1} \hat{\rho} &= \frac{1}{2} \left(|1\rangle \langle 1| \langle 0| 0\rangle - |1\rangle \langle 0| \langle 0| 1\rangle + |0\rangle \langle 1| \langle 1| 0\rangle + |0\rangle \langle 0| \langle 1| 1\rangle \right) & (2.29) \\ &= \frac{1}{2} \left(|0\rangle \langle 0| + |1\rangle \langle 1| \right) . & (2.30) \end{aligned}$$

Using Eq. (2.18) we find that $\mathcal{I}_{12} = 1$. Before the quantum mutual information is multiplied by a normalization factor of $\frac{1}{2}$ the singlet has quantum mutual information equal to 2 bits. This indicates the non-classical correlation of this quantum state. Classically the mutual information between two observed random bits is maximally 1. The difference in quantum mechanics is that the combination of two subsystems with maximally random states does not result in a maximally random state of the entire system. For the spin singlet the quantum

state of the entire system is a single quantum state with entropy $S(|\psi\rangle\langle\psi|) = 0$. This feature of quantum mechanics has no classical analogue and is due to quantum entanglement between the two qubits. Completing the entries for the quantum mutual information adjacency matrix we have $\mathcal{I}_{12} = \mathcal{I}_{21} = 1$ and $\mathcal{I}_{11} = \mathcal{I}_{22} = 0$. Our adjacency matrix for the spin singlet is thus

$$\mathcal{I} = \begin{pmatrix} 0 & 1 \\ 1 & 0 \end{pmatrix} . \tag{2.31}$$

We generalize the spin singlet by parameterizing the relative weight between $|01\rangle$ and $|10\rangle$ by θ and allowing for a relative phase ϕ between the two states. The resulting state is

$$|\psi(\theta)\rangle = \cos(\theta)|01\rangle + \sin(\theta)\,\mathrm{e}^{i\phi}|10\rangle , \tag{2.32}$$

this has reduced density matrices $\hat{\rho}_1 = \hat{\rho}_2$, with

$$\hat{\rho}_1 = \cos(\theta)^2 |0\rangle\langle 0| + \sin(\theta)^2 |1\rangle\langle 1| . \tag{2.33}$$

The resulting von Neumann entropy is equal to

$$S_1 = -\cos(\theta)^2 \log\left(\cos(\theta)^2\right) - \sin(\theta)^2 \log\left(\sin(\theta)^2\right) , \tag{2.34}$$

so that the quantum mutual information between two such qubits is

$$\mathcal{I} = -\begin{pmatrix} 0 & S_1 \\ S_1 & 0 \end{pmatrix} . \tag{2.35}$$

The quantum mutual information between the two qubits is maximized when $\theta = \pi/4$, where $|\psi(\pi/4)\rangle$ is the spin singlet state, and is minimized when $\theta = 0, \pi/2$ where the quantum state factorizes. In Fig. 2.1 we show how the quantum mutual information between the two qubits changes as a function of θ.

In Sec. 2.4 we have studied the quantum mutual information networks of simple quantum states. In Sec. 2.5 we provide a definition of quantum phase transitions. In Chapter 3 we will define useful measures on quantum mutual information complex networks. Finally, in Chapter 4 we will apply these techniques to find the critical points of two quantum many body Hamiltonians.

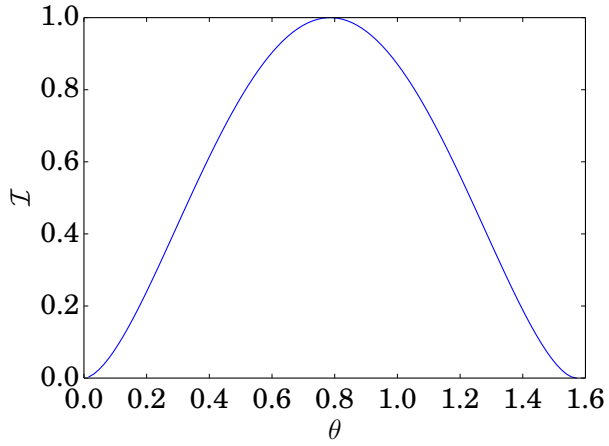

Fig. 2.1: *Quantum mutual information between two qubits.* The quantum mutual information between two qubits is maximized when the states $|01\rangle$ and $|10\rangle$ are in equal superposition, and minimized for either state alone.

2.5 Quantum Phase Transitions

A quantum phase transition is a non-analyticity in the ground state energy of an infinite lattice system [34]. Near a quantum phase transition the length scale characterizing correlations diverges according to a power law as defined in Eq. (2.36) [34]

$$\xi^{-1} \sim \Lambda |g - g_c|^{\nu} \tag{2.36}$$

where g is some parameter of a model Hamiltonian. For example in the transverse Ising model an external field g disorders spins in the z-direction. For small external field strength spins spontaneously align along the z-direction. For large external field strengths the z components of spins become disordered and the ground state enters a paramagnetic phase. In the disordered phase, correlations decay exponentially as summarized in Eq. (2.37), while in the ordered phase, the degrees of freedom become correlated across the entire system [34]

$$\langle 0| \hat{\sigma}_i^z \hat{\sigma}_j^z |0\rangle \sim \mathrm{e}^{-|x_i - x_j|/\xi} \,. \tag{2.37}$$

For $g < 1$, the divergence in the length scale of correlations at the quantum critical point of the transverse Ising model gives rise to a non-zero value of an order parameter as defined

in Eq. (2.38)

$$\lim_{n\to\infty} \langle 0| \sigma_i^z \sigma_{i+n}^z |0\rangle = (1-g^2)^{1/4} . \tag{2.38}$$

While for $g > 1$, $\lim_{n\to\infty} \langle 0| \sigma_i^z \sigma_{i+n}^z |0\rangle = 0$. The transverse Ising quantum phase transition is a second order phase transition, therefore a divergence occurs in the derivative of the order parameter, as shown in Eq. (2.39)

$$\frac{\mathrm{d}}{\mathrm{d}g} \lim_{n\to\infty} \langle 0| \sigma_i^z \sigma_{i+n}^z |0\rangle = \frac{\mathrm{d}}{\mathrm{d}g}(1-g^2)^{1/4} = \frac{-g}{2}(1-g^2)^{-3/4} . \tag{2.39}$$

The divergence in the derivative of the infinite range correlations gives rise to a finite size scaling law [54]. The effective critical point of a finite size system $g_c(L)$ is displaced from the thermodynamic critical point g_c according to the equation

$$g_c(L) = g_c + AL^{-1/\nu} . \tag{2.40}$$

In Chapter 4 of this thesis we will apply finite size scaling analysis to complex network measures applied to quantum mutual information adjacency matrices of finite systems in order to estimate the location of quantum critical points in two model Hamiltonians, the transverse Ising model and the Bose-Hubbard model. For the BKT transition studied in Chapter 4 we use the same form for the scaling law

$$(J/U)_c(L) = (J/U)_c + AL^{-1/\nu} . \tag{2.41}$$

However the BKT transition "does not yield a singularity in any derivative of the thermodynamic potential at the transition, and therefore is sometimes called an infinite order transition."[55] Therefore Eq. (2.41) is only an ansatz.

2.6 Quantum Cellular Automata

In this section we define two types of quantum cellular automata, Hamiltonian-based quantum cellular automata and unitary-based quantum cellular automata. Inspired by Conway's game of life Bleh, Montangero, and Calarco created the BCM Hamiltonian shown in Eq. (2.42) [40]. A site can either be in the dead state $|0\rangle$ or the alive state $|1\rangle$. If a site has

two or three neighbors in the alive state $|1\rangle$ then this site undergoes evolution according to the term $\hat{b}_i + \hat{b}_i^\dagger$, otherwise the site remains static. The BCM Hamiltonian is defined as

$$\hat{H} = \sum_{i=1}^{L} \left(\hat{b}_i + \hat{b}_i^\dagger\right) \left(\hat{\mathcal{N}}_i^{(2)} + \hat{\mathcal{N}}_i^{(3)}\right) . \tag{2.42}$$

Where $\hat{\mathcal{N}}_i^{(2)}$ is the projector onto the subspace spanned by states in which site i has two neighbors in the alive state and $\hat{\mathcal{N}}_i^{(3)}$ is the projector onto the subspace spanned by states in which site i has three neighbors in the alive state. The neighborhood of site i of the BCM Hamiltonian is defined as all sites within two lattice spacings of site i, $N_i \equiv \{j : 0 < |i-j| \leq 2\}$. Note that $\left[\hat{b}_i, \hat{b}_j^\dagger\right] = 0$ for $i \neq j$, $(\hat{b}_i)^2 = (\hat{b}_i^\dagger)^2 = 0$, $\{b_i, b_i^\dagger\} = 1$, and $\hat{n}_i \equiv \hat{b}_i^\dagger \hat{b}_i$. The operators $\hat{\mathcal{N}}_i^{(2)}$ and $\hat{\mathcal{N}}_i^{(3)}$ can be written in terms of number operators as

$$\hat{\mathcal{N}}_i^{(2)} = \sum_{\sigma} \hat{\bar{n}}_{\sigma(i)} \hat{\bar{n}}_{\sigma(i-1)} \hat{n}_{\sigma(i+1)} \hat{n}_{\sigma(i+2)} , \tag{2.43}$$

and

$$\hat{\mathcal{N}}_i^{(3)} = \sum_{\pi} \hat{\bar{n}}_{\pi(i)} \hat{n}_{\pi(i-1)} \hat{n}_{\pi(i+1)} \hat{n}_{\pi(i+2)} \tag{2.44}$$

where the sums over σ and π denote the sum over all permutations of the site indices and where $\hat{\bar{n}}_i \equiv \hat{1} - \hat{n}_i$. This amounts to $\binom{4}{2} = 12$ terms for $\hat{\mathcal{N}}_i^{(2)}$, and $\binom{4}{3} = 4$ terms for $\hat{\mathcal{N}}_i^{(3)}$. Generalizing the BCM Hamiltonian we study Hamiltonians of the form

$$\hat{H} = \sum_{i} \left(\hat{b}_i + \hat{b}_i^\dagger\right) \hat{R}_i . \tag{2.45}$$

We refer to $\hat{b}_i + \hat{b}_i^\dagger$ as the main operator and $\hat{R}_i$ as the rule operator of our Hamiltonian-based QCA. The operator $\hat{R}_i$ defines the conditions for activity at site i in terms of the neighborhood of site i. The neighborhood of site i is defined as $N_i \equiv \{j : 0 < |i-j| \leq r\}$. The operator $\hat{b}_i + \hat{b}_i^\dagger$ defines the action of the Hamiltonian at site i. It maps $|0\rangle \to |1\rangle$ and $|1\rangle \to |0\rangle$. That is, it swaps $|0\rangle$ with $|1\rangle$ and no superposition is induced. In the standard basis $\hat{b}_i + \hat{b}_i^\dagger$ has matrix representation

$$\left[\hat{b}_i + \hat{b}_i^\dagger\right]_{\mathcal{B}_i} = \begin{pmatrix} 0 & 1 \\ 1 & 0 \end{pmatrix} . \tag{2.46}$$

When the Hamiltonian is exponentiated to form the propagator $\hat{b}_i+\hat{b}_i^\dagger$ induces a superposition of $|0\rangle$ and $|1\rangle$ at site i if the conditions of the neighborhood are right as determined by the rule operator. The operator $\hat{R}_i$ is the rule operator defining the conditions for activity at site i.

$$\hat{R}_i = \sum_{j=0}^{2r} c_j \mathcal{N}_i^{(j),r} \,, \tag{2.47}$$

with $c_j \in \{0,1\}$. The symbol $\mathcal{N}_i^{(j),r}$ denotes the projector onto the subspace in which site i has j neighbors in the alive state. If the number of neighbors of site i in state $|1\rangle$ is j then $\mathcal{N}_i^{(j),r} = \hat{1}$, otherwise $\mathcal{N}_i^{(j),r} = \hat{0}$. The activity of a site is determined only by the total number of living sites in the neighborhood of that site. If $c_j = 0$ a site is inactive if there are exactly j living sites in the neighborhood of site j. If $c_j = 1$ a site is active if there are exactly j living sites in the neighborhood of a site. Such rules are analogous to the classical totalistic automata defined in [56]. However, the dynamics of our Hamiltonian-based quantum cellular automata are different. Firstly, under continuous time evolution the main operator induces local superposition between $|0\rangle$ and $|1\rangle$. Secondly, as the main operator of site i induces superposition at site i the rule operators of site $i+1$ now sees a superposition at site i. Since the different states composing the superposition will have different numbers of living sites in the neighborhood of site $i+1$, $\hat{R}_{i+1}$ may determine site $i+1$ to be active in some and inactive in others.

We enumerate our rules in terms of the binary expansion $c_{2r}c_{2r-1}...c_2...c_1c_0$ of each rule,

$$R = \sum_{i=0}^{2r} c_i 2^i \,. \tag{2.48}$$

For instance the BCM Hamiltonian has $c_0 = c_1 = c_4 = 0$ and $c_2 = c_3 = 1$. Therefore its binary expansion is $c_4c_3c_2c_1c_0 = 01100$. Its resulting number is $R = 12 = 0\times 2^0 + 0\times 2^1 + 1\times 2^2 + 1\times 2^3 + 0\times 2^4$. The quantum state of Hamiltonian-based quantum cellular automata evolves according to the Schrödinger equation, since our Hamiltonians are time independent

$$|\psi(t)\rangle = \mathrm{e}^{-\mathrm{i}\hat{H}t}\,|\psi(0)\rangle \ . \tag{2.49}$$

Unitary-based quantum cellular automata are defined in a similar way to Hamiltonian-based quantum cellular automata. In Hamiltonian-based quantum cellular automata we define the conditions for activity at site i in terms of projectors defined on the neighborhood of site i. In unitary-based quantum cellular automata we instead define the conditions for application of the unitary operator $\hat{V}_i$ to site i in terms of projectors defined on the neighborhood of site i. Therefore $\hat{V}_i$ is like the main operator of our Hamiltonian-based QCA: it performs the action. We will refer to such operators as main operators in the context of both Hamiltonian and unitary-based QCA. For nearest neighbor unitary-based quantum cellular automata the rule defining the conditions for application of $\hat{V}_i$ can be encoded into a 2×2 matrix S with elements $s_{mn} \in \{0, 1\}$ [45]. The operator applied to sites $i-1, i, i+1$ to update the state of site i is

$$\hat{U}_S(\hat{V})_i \equiv \sum_{m,n=0}^{1} |m\rangle \langle m|_{i-1} \otimes \hat{V}_i^{mn} \otimes |n\rangle \langle n|_{i+1} \ , \tag{2.50}$$

where $\hat{V}_i^{mn}$ is either $\hat{V}_i$ or the identity operator as determined by s_{mn},

$$\hat{V}_i^{mn} = s_{mn}\hat{V}_i + (1 - s_{mn})\hat{1}_i \, . \tag{2.51}$$

Instead of evolving the entire lattice simultaneously, in unitary-based quantum cellular automata the lattice is evolved by first evolving all even sites through an entire discrete time step, and then evolving all odd sites through an entire discrete time step. This is referred to as the alternate (ALT) mode of a quantum cellular automata [45]

$$|\psi(t+1)\rangle = \prod_{i \in \mathrm{ALT}} \hat{U}_S(\hat{V}) \, |\psi(t)\rangle \equiv \prod_{i'\%2=1} \hat{U}_S(\hat{V})_{i'} \prod_{i\%2=0} \hat{U}_S(\hat{V})_i \, |\psi(t)\rangle \ . \tag{2.52}$$

The unitary-based quantum cellular automata we study have a different enumeration scheme than the Hamiltonian-based quantum cellular automata. The rule number of a unitary-based quantum cellular automata is defined in terms of the matrix elements of S, specifically [45]

$$S = s_{11}2^3 + s_{10}2^2 + s_{01}2^1 + s_{00}2^0 \, . \tag{2.53}$$

In Chapter 6 we will study the equilibrium entanglement properties of unitary-based QCA. In contrast to Hamiltonian-based quantum cellular automata where the main operator is $\hat{b}_i + \hat{b}_i^\dagger$, for unitary-based quantum cellular automata we will study the dynamics generated with $\hat{V}_i = \hat{H}_D \hat{P}(\theta)$ as the main operator. The operator $\hat{H}_D$ denotes the Hadamard gate. The Hadamard gate maps $|0\rangle \to 1/\sqrt{2}\,(|0\rangle + |1\rangle)$ and maps $|1\rangle \to 1/\sqrt{2}\,(|0\rangle - |1\rangle)$, placing states in equal superposition. In the standard basis $\hat{H}_D$ has matrix representation

$$H_D = \frac{1}{\sqrt{2}} \begin{pmatrix} 1 & 1 \\ 1 & -1 \end{pmatrix} . \tag{2.54}$$

The superposition induced by $\hat{H}_D$ highlights an important difference between Hamiltonian-based and unitary-based QCA. In Hamiltonian-based QCA the superposition results from continuous time evolution, even for the main operator $\hat{b}_i + \hat{b}_i^\dagger$. For unitary-based QCA using $\hat{b}_i + \hat{b}_i^\dagger$ as the main operator does not result in superposition since $\hat{b}_i + \hat{b}_i^\dagger$ just swaps $|0\rangle$ with $|1\rangle$. The resulting time evolution is entirely classical. Therefore in unitary-based QCA it is necessary to use operators like $\hat{H}_D$ to induce superposition. The operator $\hat{P}(\theta)$ is a phase shift gate with phase shift θ. It maps $|0\rangle \to |0\rangle$ and $|1\rangle \to \mathrm{e}^{\mathrm{i}\theta}\,|1\rangle$. Thus $\hat{P}(\theta)$ induces a relative phase between $|0\rangle$ and $|1\rangle$. The phase shift gate has matrix representation

$$P(\theta) = \begin{pmatrix} 1 & 0 \\ 0 & \mathrm{e}^{\mathrm{i}\theta} \end{pmatrix} . \tag{2.55}$$

2.7 OpenMPS vs. Trotter Exact Diagonalization

An arbitrary quantum state can be expressed in terms of d^L complex numbers as described in Eq. (2.9). A quantum state defined on a lattice of L sites generated uniformly random under the Haar measure will have an average von Neumann entropy of a subset of sites I of [48]

$$\mathbb{E}[S(\hat{\rho}_I)] > |I| \log_2(d) - \frac{d^{2|I|-L}}{2} , \tag{2.56}$$

where $|I|$ is the number of sites in subsystem I. This result tells us that a random quantum state has von Neumann entropy near its maximum value of $|I|\log_2(d)$ for the entropy of its subsystems as $L \to \infty$. Thus asymptotically $S(\hat{\rho}_I) \propto |I|$ for random quantum states.

Such states are highly entangled and are said to obey a volume law. It has been found that the ground states of many physical Hamiltonians instead satisfy an area law in the entropy of subsystems. In one dimension this implies the entropy is proportional to a constant $S(\hat{\rho}_I) \propto O(1)$ [48]. States satisfying an area law have less entanglement between subsystems. This limited entanglement allows these states to be efficiently represented as matrix product states [48]. The matrix product state (MPS) representation of a quantum state is

$$|\psi_{\mathrm{MPS}}\rangle = \sum_{i_1,\ldots,i_L=1}^{d} \mathrm{Tr}\left(A^{[1]i_1}\ldots A^{[L]i_L}\right)|i_1\ldots i_L\rangle \tag{2.57}$$

where $A^{[k]i_k}$ is a matrix of dimensions $\chi_k \times \chi_{k+1}$ and $\chi = \max_k \chi_k$ [49]. Thus the number of parameters necessary to describe an MPS is approximately $O(dL\chi^2)$, that is polynomial in the system size instead of exponential. Such states satisfy an area law by construction [48] assuming χ is not function of L. The matrices in Eq. (2.57) are computed from singular value decompositions computed on tensors formed from the coefficients of the quantum state. The χ_k are the number of singular values that are kept in a singular value decomposition. Highly entangled states require more singular values to be kept in order to accurately represent them. Since the ground states of many physical Hamiltonians obey an area law, in Chapter 4 we use OpenMPS to variationally find the ground states of the transverse Ising and Bose-Hubbard Hamiltonians. To find the ground state of quantum many body Hamiltonians OpenMPS initializes the quantum state to an MPS form. OpenMPS then performs a series of local minimizations of the energy by solving eigenvalue problems associated to sets of s sites of the matrix product state $A^{[j]}\ldots A^{[j+s-1]}$ [49]. By sweeping over the lattice until the variance of the energy of the MPS satisfies inequality (2.58)

$$\langle \hat{H}^2 - \langle \hat{H} \rangle^2 \rangle < \epsilon_v \tag{2.58}$$

OpenMPS converges to the ground state of quantum many body Hamiltonians. In OpenMPS the number of singular values that are kept in a decomposition is determined by two numbers, ϵ and $\chi_{\max}$. When the singular value decomposition is computed OpenMPS constructs a vector of singular values $\vec{\sigma}$. In determining how many of these to keep OpenMPS assures

that inequality (2.59) is satisfied

$$\sum_{i=1}^{\chi} \frac{\sigma_i^2}{\vec{\sigma} \cdot \vec{\sigma}} \leq \epsilon. \tag{2.59}$$

Decreasing ϵ results in a better characterization of the true quantum state. However, since there is no upper bound on χ the OpenMPS algorithm may increase χ without limit and run out of memory. The $\chi_{\max}$ parameter assures that the algorithm will not increase χ without limit.

In Chapter 5 we apply one of the latest MPS based time evolution algorithms to study the dynamics of the BCM Hamiltonian, the Zaletel time evolution scheme [57]. The OpenMPS variational ground state search algorithm and Zaletel time evolution scheme were implemented by members of the CTPRG and are available at [58]. The main limitation of MPS methods applied to dynamics is that the entanglement of quantum many body states evolved under a global quench of a Hamiltonian parameter increases linearly in time, implying that χ grows exponentially in time [49, 59]. Unlike statics, in dynamics there is no area law guaranteeing the success of the MPS ansatz. In Chapter 5 we find that the entanglement generated by the BCM Hamiltonian quickly reaches $\chi_{\max}$ and OpenMPS is not able to accurately compute the late-time entanglement properties of quantum many body states. Therefore in Chapter 6 we conduct a study of quantum cellular automata generalizations of the BCM Hamiltonian using a Trotter-based time evolution scheme. This scheme uses an exact representation of the quantum state. We refer to this code as Trotter exact in Chapter 5. This code was developed by L. Hillberry [45]. While the representation of the quantum state is exact in the Trotter based code, the propagator is approximated via the Suzuki-Trotter decomposition [60]

$$\mathrm{e}^{\left(\hat{A}+\hat{B}\right)\Delta t} = \mathrm{e}^{\hat{A}\Delta t/2}\mathrm{e}^{\hat{B}\Delta t}\mathrm{e}^{\hat{A}\Delta t/2} + O(\Delta t^3)\,. \tag{2.60}$$

For a quantum cellular automata in which the neighborhood of site i is $N_i \equiv \{j : 0 < |i-j| \leq r\}$, the corresponding Suzuki-Trotter decomposition of the propagator is given by Eq. (2.63):

$$\hat{U}(\Delta t) = \mathrm{e}^{-\mathrm{i}\hat{H}\Delta t} = \mathrm{e}^{-\mathrm{i}\sum_i \hat{H}_i \Delta t} \tag{2.61}$$

$$= \mathrm{e}^{-\mathrm{i}\sum_{j=0}^{r'-1}\sum_{i\%r'=j}\hat{H}_i\Delta t} \tag{2.62}$$

$$= \prod_{j=0}^{r'-2} \mathrm{e}^{-\mathrm{i}\sum_{i\%r'=j}\hat{H}_i\Delta t/2}\mathrm{e}^{-\mathrm{i}\sum_{i\%r'=r'-1}\hat{H}_i\Delta t}\prod_{j=0}^{r'-2}\mathrm{e}^{-\mathrm{i}\sum_{i\%r'=j}\hat{H}_i\Delta t/2} + O(\Delta t^3)\,, \tag{2.63}$$

where $r' = 2r+1$. Since the operators in the sum $\sum_{i\%r'=j}\hat{H}_i$ are defined on non-overlapping sites and since the off site commutation relations are all zero the exponential of such a term factorizes exactly

$$\mathrm{e}^{-\mathrm{i}\sum_{i\%r'=j}\hat{H}_i\Delta t} = \prod_{i\%r'=j}\mathrm{e}^{-\mathrm{i}\hat{H}_i\Delta t}\,. \tag{2.64}$$

Thus the only error introduced by the Suzuki-Trotter expansion is $O(\Delta t^3)$. Finally, in Chapter 5 we demonstrate the convergence of our Trotter exact code by comparing it to exact diagonalization (ED) code that computes the propagator $\hat{U}$ directly. The only error made by the ED code is due to the finite precision with which the computers represent floating-point numbers. The exact diagonalization code does not have the additional $O(\Delta t^3)$ of the Trotter-based code. We consider the error made by the ED code to be negligible throughout the entire thesis.

CHAPTER 3

COMPLEX NETWORK MEASURE DEVELOPMENT

In this chapter we provide definitions of our complex network measures, error analysis of our network measures, and a study of our complex network measures applied to random networks, random quantum states, and cluster states.

3.1 Definitions of Complex Network Measures

In this section we provide definitions of all complex network measures that appear in this thesis. The complex network measures defined in this section are: *out-strength*, *in-strength*, *network density*, *disparity*, *clustering coefficient*, *local clustering coefficient*, *Pearson R similarity*, *closeness centrality*, *harmonic centrality*, and *betweenness centrality* [3, 61, 62]. These are well-established complex network measures which we review here for the reader's convenience. The present study uses a mixture of unweighted and weighted complex network measures. The use of unweighted complex network measures for the analysis of our quantum mutual information networks is formally justified by averaging over a hypothetical ensemble of unweighted networks [63]. We emphasize that although we define our complex network measures in terms of quantum mutual information adjacency matrices, they are well defined for arbitrary matrices.

The *out-strength* of a node is the sum of its outgoing connections to other nodes. Strength is defined as

$$s_i^{\text{out}} = \sum_{j=1}^{L} \mathcal{I}_{ij} \,. \tag{3.1}$$

A node can have high out-strength if it has connections to many other nodes, or if it has strong connections to only a few other nodes. In Chapter 7 nodes with connections to many other nodes correspond to students that collaborate with many other students. Nodes with strong connections to only a few other nodes correspond to students that collaborate

frequently with only a few other students. The *in-strength* is similarly defined and quantifies the importance of a node by the number of incoming connections $s_i^{\text{in}} = \sum_{j=1}^{L} \mathcal{I}_{ij}^{T}$.

Network density is the fraction of links that exist in a network compared to the total number possible in a network with L nodes. In the case of weighted networks network density measures not the density of connections, but the average strength of connection. For quantum mutual information adjacency matrices, the average quantum mutual over all two sites is equal to the network density

$$D \equiv \frac{1}{L(L-1)} \sum_{i,j=1}^{L} \mathcal{I}_{ij} \,. \tag{3.2}$$

Network density has been shown to correlate with robustness of food-webs to random removal of species [2][1]. In a network in which most of the connections that can exist do exist the removal of any given link becomes less important. In our study of quantum mutual information networks network density measures the average level of correlation between sites.

The *disparity* of a node's connections is a measure of the non-uniformity of the connection strengths. If a node has a single strong connection with all other connections being much weaker, then that node has high disparity. If the connection strengths of a node are all of approximately equal strength, then that node has a low disparity. Disparity is defined as

$$Y_i \equiv \frac{1}{(s_i)^2} \sum_{j=1}^{L} (\mathcal{I}_{ij})^2 = \frac{\sum_{j=1}^{L} (\mathcal{I}_{ij})^2}{\left(\sum_{j=1}^{L} \mathcal{I}_{ij}\right)^2} \,. \tag{3.3}$$

We define the disparity of a network to be the average of disparity over all nodes in the network

$$Y = \frac{1}{L} \sum_{i=1}^{L} Y_i \,. \tag{3.4}$$

Observe that if the mutual information between lattice sites adopts a constant value $\mathcal{I}_{ij} = a$, that $Y_i = a^2 (L-1) / a^2 (L-1)^2 = 1/(L-1)$. If a node has relatively uniform weights

[1]Reference [2] uses the term connectance in place of density.

across its neighbors the disparity between nodes will be approximately $1/(L-1)$. On the other hand, if a particular $\mathcal{I}_{ij}$ takes on a dominant value b, then $Y_i \approx b^2/b^2 = 1$. Disparity has been used to study metabolic networks in Escherichia coli: in these metabolic networks a weighted link W_{ij} is placed between a metabolite i and a chemical reaction j if metabolite i is produced by reaction j. The weight of the link W_{ij} is the mass of the metabolite i that is produced by the chemical reaction [14]. Disparity enable these researchers to distinguish between two different forms of organization of the metabolic network and allowed them to quantify the presence of a backbone structure in which each metabolite has a dominant source reaction. In Chapter 7 we refer to the disparity of a node as its *out-disparity*, since in that chapter we are studying directed networks. The out-disparity of a node's connections is a measure of the non-uniformity of the outgoing connection strengths. Nodes with high out-disparity correspond to students that collaborate with certain students much more often than they collaborate with other students. Nodes with low disparity correspond to students that collaborate equally with all students that they collaborate with. The network measure *in-disparity* measures the non-uniformity of the incoming connection strengths. To compute Y_i^{in} one makes the substitution $\mathcal{I} \to \mathcal{I}^T$ in Eq. (7.6).

The *clustering coefficient* is a measure of the transitivity of connections. That is, the likelihood that a is connected to c, given that a is connected to b and b is connected to c. The clustering coefficient is defined as

$$C \equiv \frac{\text{Tr}(\mathcal{I}^3)}{\sum_{j\neq i}^{L}\sum_{i=1}^{L}[\mathcal{I}^2]_{ij}} \,. \tag{3.5}$$

The clustering coefficient C is 3 times the ratio of triangles (three mutually connected vertices) to connected triples in an unweighted network. The clustering coefficient has been used in studies of social networks. In that context a link A_{ij} between two nodes i and j corresponds to a social relationship between two people. Therefore in social networks clustering measures the probability that the friend of a friend is also a friend [4]. It has been found that social networks and many real world networks have larger clustering coefficients

than random networks.

The *local clustering coefficient* is also a measure of the transitivity of connections. However unlike the clustering coefficient the local clustering coefficient quantifies the transitivity of connections of individual nodes. The local clustering coefficient is defined as

$$c_i^L \equiv \frac{[\mathcal{I}^3]_{ii}}{\sum_{j\neq ik\neq i} \mathcal{I}_{ij}\mathcal{I}_{ik}} \,. \tag{3.6}$$

That is, one divides the total number of triangles node i is in by the total number of connected triples centered on node i.

Pearson R similarity is a measure of how similar two nodes in a network are. We also refer to this measure as the Pearson correlation coefficient in Chapter 4. It is a linear correlation computed on the link weights of the two nodes i and j. A large value for Pearson R similarity means that two nodes share many of the same neighbors, and with approximately equal connection strengths. The Pearson R similarity between two nodes is defined as

$$r_{ij} \equiv \frac{\sum_{k=1}^{L} \left(\mathcal{I}_{ik} - \langle \mathcal{I}_i \rangle\right)\left(\mathcal{I}_{jk} - \langle \mathcal{I}_j \rangle\right)}{\sqrt{\sum_{k=1}^{L} \left(\mathcal{I}_{ik} - \langle \mathcal{I}_i \rangle\right)^2}\sqrt{\sum_{k=1}^{L} \left(\mathcal{I}_{jk} - \langle \mathcal{I}_j \rangle\right)^2}} \,. \tag{3.7}$$

In previous studies this quantity has been used to study the similarity of connections in unweighted networks [3], in our study we compute the Pearson R similarity R to quantify the similarity of connection strengths of two sites on a quantum lattice. In Chapter 4 we compute

$$R \equiv r_{L/2,L/2+1} \,. \tag{3.8}$$

to study the quantum phase transitions of the transverse Ising and Bose-Hubbard models.

In Chapter 7 we study weighted directed networks that summarize the patterns of collaboration between students in three physics courses. To analyze these networks we introduce three additional network quantities implemented in NetworkX [62], closeness centrality, harmonic centrality, and betweenness centrality.

Closeness centrality is a measure of how close a node is on average to other nodes when one must travel along directed links in the direction of the link. The closeness centrality of

node u is defined as

$$c^C(u) = \frac{n-1}{|A|-1} \sum_{v \neq u} d(v,u), \tag{3.9}$$

where $d(u,v)$ is the shortest path distance between v and u, n is the number of nodes reachable from u, and $|A|$ is the number of nodes in the network [62, 64].

For unweighted networks the distance between two nodes is the number of links separating the two nodes. In a weighted network one can also associate a distance between any pair of nearest neighbor nodes. For our analysis we will define the distance between nearest neighbors i and j to be the inverse of the weight connecting them, $1/w_{ij}$. One then computes the distance between any two nodes by summing over the inverse edge weights of the links separating the two nodes. In the context of social networks, closeness centrality can be thought of as a measure of independence as described in [64]. This is because a node with a large closeness centrality does not have to rely on other nodes to transmit messages across the network [64].

As an example of a shortest path between two nodes consider the paths in the network shown in Fig. 3.1, where links are labeled by their corresponding distances. In traveling from node 1 to node 4 in Fig. 3.1, if one travels along the path from node 1 to node 2, from node 2 to node 3, and from node 3 to node 4, one will have traveled a distance of 3. Similarly along the path from 1 to 6, and from 6 to 4 one travels a distance of 3. However, along the path from 1 to 5 and from 5 to 4 one travels a distance of 4. So there are two distinct shortest paths from node 1 to node 4.

Harmonic centrality is also a measure of how close a node is to other nodes in the network when one must travel along directed links in the direction of the link. The harmonic centrality of node u is defined as

$$c^H(u) = \sum_{v \neq u} \frac{1}{d(v,u)}, \tag{3.10}$$

where $d(v,u)$ is the shortest path distance between nodes v and u [62, 65]. A quantity termed the efficiency of a network was the inspiration for the definition of harmonic centrality [65].

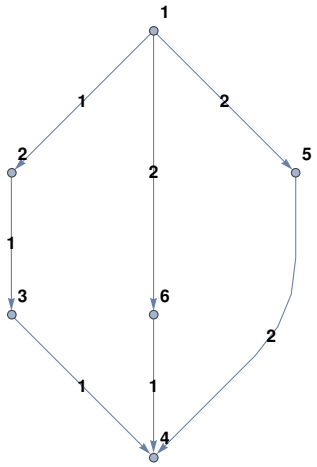

Fig. 3.1: *Directed network illustrating concept of multiple shortest paths.* Multiple shortest paths connect nodes 1 and 4. Links are labeled by their weight, and nodes are given an integer label to distinguish them from other nodes. The length of a path connecting two nodes is the sum of the weights of the links connecting them. Closeness centrality, harmonic centrality, and betweenness centrality all quantify the importance of a node via its shortest paths to other nodes.

The efficiency of a network has been used to characterize non random structure and fault tolerance in the neural network of C. elegans and transportation networks [66].

Betweenness centrality is measure of how important a node is as a go-between for message transmission between nodes in a network, assuming that information travels along the shortest path connecting two nodes [3]. The betweenness centrality of node u is defined as

$$c^B(u) = \sum_{s,t \in V} \frac{\sigma(s,t|u)}{\sigma(s,t)}, \tag{3.11}$$

where $\sigma(s,t|v)$ is the number of shortest paths between nodes s and t that pass through node u and where $\sigma(s,t)$ is the number of shortest paths between nodes s and t [62, 67]. For example $\sigma(1,4|6) = 1$ in Fig. 3.1 because there is exactly one shortest path from 1 to 4 that passes through node 6. While $\sigma(1,4) = 2$ since there are two distinct shortest paths between nodes 1 and 4. Betweenness centrality has been used to study networks of film actors, where a connection between two nodes in a network corresponds to two actors appearing in a film together [3]. In Chapter 7 betweenness centrality is a measure of the importance of each student to information transfer throughout the network.

3.2 Error Analysis of Network Measures

The mathematical definitions of our network measures lead to some difficulties in implementing them numerically as described in the following paragraph.

The value of disparity is not singly defined about the zero network. This can be seen by the following argument. Given a constant number a and a quantum mutual information adjacency matrix $\mathcal{I}$ the value of disparity does not change upon a multiplying $\mathcal{I}$,

$$Y_i \equiv \frac{1}{(as_i)^2} \sum_{j=1}^{L} (a\mathcal{I}_{ij})^2 = \frac{\sum_{j=1}^{L} (a\mathcal{I}_{ij})^2}{\left(\sum_{j=1}^{L} a\mathcal{I}_{ij}\right)^2} = \frac{\sum_{j=1}^{L} (\mathcal{I}_{ij})^2}{\left(\sum_{j=1}^{L} \mathcal{I}_{ij}\right)^2} \,. \tag{3.12}$$

As we make a smaller we can change it continuously to zero. Given two distinct quantum mutual information adjacency matrices $\mathcal{I}_1$ and $\mathcal{I}_2$ they may have different values for network disparity, say y_1 and y_2. If we now consider the above procedure of continuously varying a to zero for each of these matrices we see that this makes disparity multiply defined for the adjacency matrix consisting of all zeros, this is the adjacency matrix for a network consisting of all nodes disconnected from each other. Since disparity is multi-valued about the zero network we impose a lower bound on our quantum mutual information adjacency matrices; for our studies we have chosen this to be $\epsilon_{\mathcal{I}} = 10^{-14}$. If a link is found to have quantum mutual information less than 10^{-14} it is set equal to 10^{-14}. In Fig. 3.2 we display the results of a simulation with disparity computed using different values of $\epsilon_{\mathcal{I}}$. The details of the simulations are unimportant; the important point is that disparity converges to a well defined value as $\epsilon_{\mathcal{I}}$ approaches 10^{-14}. Finally, in our numerical implementation a small imaginary part $\approx 10^{-16}$ is added to the denominator of disparity before taking the real part of the resulting division.

3.3 Network Measures Applied to Random Networks and Random Quantum States

In order to understand what our measures are telling us about the structure of complex networks we applied our measures to random adjacency matrices with L nodes for $L \in [3, 20]$.

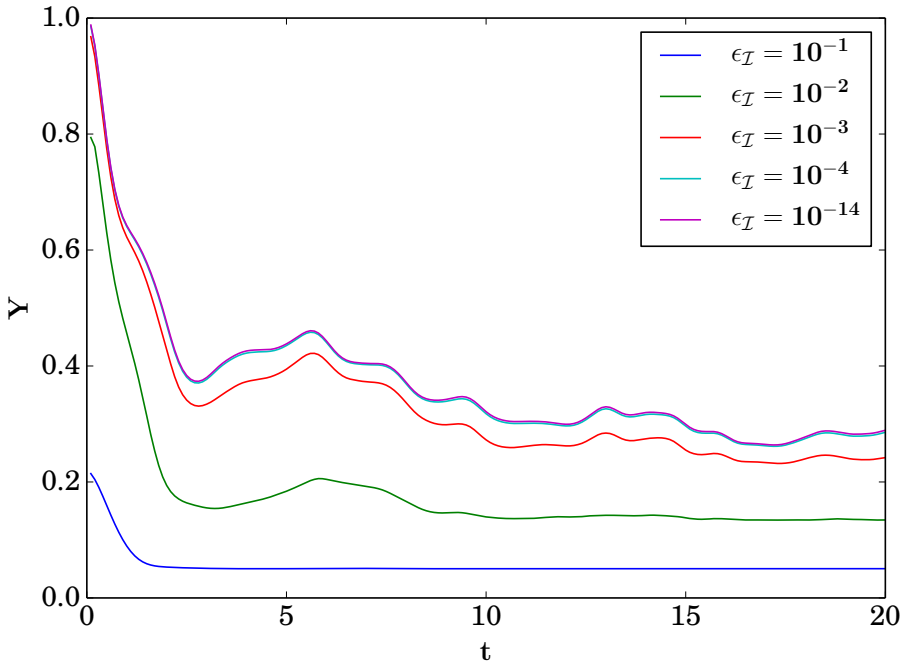

Fig. 3.2: *Convergence of disparity as a function of* $\epsilon_{\mathcal{I}}$. Horizontal axis is time, t. Disparity converges to the curve with $\epsilon_{\mathcal{I}} = 10^{-14}$ as we decrease $\epsilon_{\mathcal{I}}$. Our lower bound on quantum mutual information makes disparity single valued about the zero network. The curves for $\epsilon_{\mathcal{I}} < 10^{-5}$ overlap with the curve with $\epsilon_{\mathcal{I}} = 10^{-14}$ so we do not show them.

To generate a random adjacency matrix we generate $(L^2 - L)/2$ numbers uniformly sampled from the interval $[0, 1)$. We then set the matrix elements $\mathcal{I}_{ij}$ with $j > i$ to these values. Next we then set the matrix elements $\mathcal{I}_{ij}$ with $j < i$ equal to the elements with $j > i$ since our networks are undirected. Random numbers are generated using the NumPy function `random.rand` [68]. In Fig. 3.3 we see that the clustering coefficient asymptotically approaches $C = 0.5$ as we increase L. Similarly for network density we find that as L is increased,

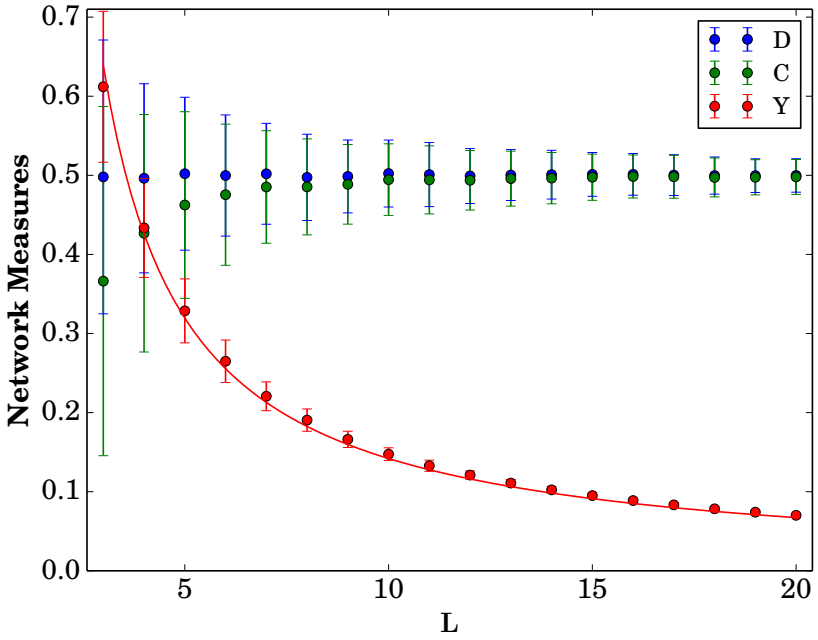

Fig. 3.3: *Network measures applied to random adjacency matrices.* The clustering coefficient asymptotically approaches $C = 0.5$ as L is increased, and has smaller fluctuations. Network density approaches $D = 0.5$ as L is increased, consistent with Eq. (3.13). Random adjacency matrices minimize disparity as L is increased. We fit the curve $\frac{1.28}{L-1}$ to Y, the fit has normalized sum of squared residuals of $R^2 = 4 \times 10^{-3}$. The scaling of disparity demonstrates that random adjacency matrices tend to minimize disparity.

network density approaches $D = 0.5$ as shown in Fig. 3.3 and the standard deviation of the data tends towards zero as shown in Fig. 3.4. Disparity displays much different behavior than the clustering coefficient and network density. We remind the reader that the minimum value of disparity is $\frac{1}{L-1}$. It appears that random networks minimize disparity since in Fig. 3.3 we observe that disparity appears to decay approximately as $\frac{1.28}{L-1}$. The observation that random

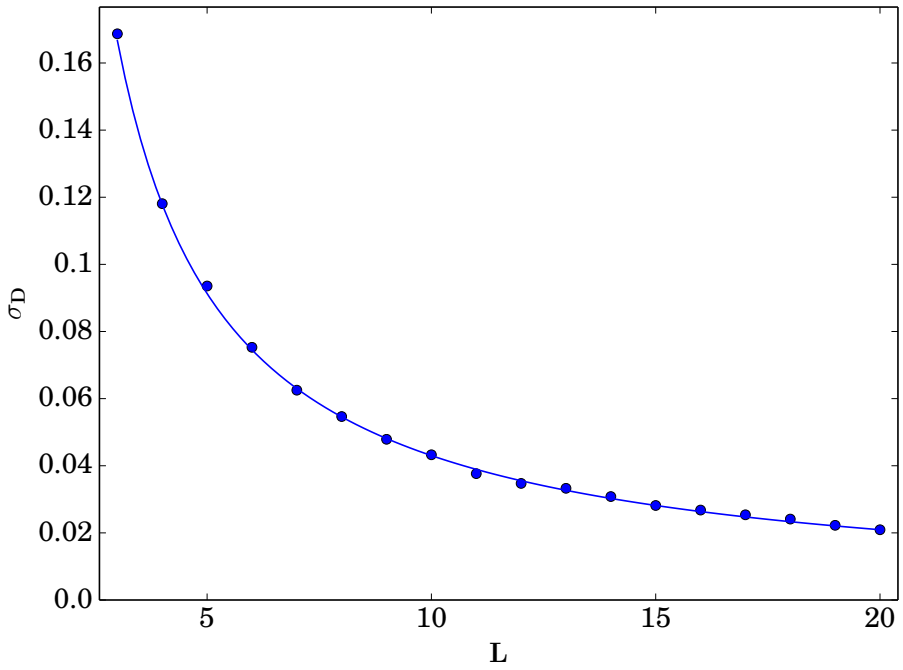

Fig. 3.4: *Fluctuations of network density applied to random adjacency matrices.* The standard deviation of network density decays as a function of L according to $\sigma_D = \sqrt{\frac{1}{6}\frac{1}{L^2-L}}$.

networks have $Y \approx \frac{1}{L-1}$ can be understood from observing that networks with $Y \approx 1$ must have nodes that have only one or a few strong connections. Suppose $0.9 < \mathcal{I}_{ij} \leq 1$, with all other connections $0 < \mathcal{I}_{ij} \leq 0.1$. The probability of these connection strengths for a single node is $(\frac{1}{10})^L$. For the entire network of L nodes the probability of them all having a large value for disparity is then $\approx (\frac{1}{10})^{L^2}$. We can understand both the variance and the mean of network density from the following derivation. We choose an ordering of the links so that we may replace $\mathcal{I}_{ij}$ with x_i and we note that there are $N = \frac{L^2-L}{2}$ links, all being independent random variables. The average network density of random adjacency matrices is

$$\langle D(\mathcal{I})\rangle = \int D(\mathcal{I})P(\mathcal{I})\mathrm{d}\mathcal{I} = \int_0^1 ... \int_0^1 \frac{2}{L(L-1)} \sum_{i,j>i} \mathcal{I}_{ij} \prod_{i,j>i} \mathrm{d}\mathcal{I}_{ij} \tag{3.13}$$

$$= \frac{1}{N} \int_0^1 ... \int_0^1 \sum_{i=1}^{N} x_i \prod_{i=1}^{N} \mathrm{d}x_i \tag{3.14}$$

$$= \frac{1}{N} N \int_0^1 ... \int_0^1 x_1 \prod_{i=1}^{N} \mathrm{d}x_i \tag{3.15}$$

$$= \frac{1}{N} N \int_0^1 ... \int_0^1 \frac{1}{2} \prod_{i=2}^{N} \mathrm{d}x_i \tag{3.16}$$

$$= \frac{1}{2}\,. \tag{3.17}$$

Performing a similar calculation for the evaluation of $\langle D(\mathcal{I})^2\rangle$ we get

$$\langle D(\mathcal{I})^2\rangle = \frac{1}{4} + \frac{1}{6}\frac{1}{L^2 - L}\,. \tag{3.18}$$

This accounts for why the network density is always near $\frac{1}{2}$ and for why the variance decreases as a function of L. We observe that since $Y \approx 1/(L-1)$ for random networks

$$\sigma_D \approx \frac{Y}{6L}\,. \tag{3.19}$$

We confirm this in Fig. 3.5.

For comparison to random networks we also applied our network measures to 100 random quantum states for system sizes $L \in [3, 10]$ as shown in Fig. 3.6. A random quantum state of L qubits is generated by generating 2^L complex numbers with real and imaginary parts distributed according the normal distribution. Random numbers are generated with the numpy function `random.randn` [68]. We observe that network density and clustering coefficient behave very differently than for random adjacency matrices. Network density decays as a function of system size for random quantum states while it is constant for random adjacency matrices. One explanation for this decay is that significant levels of correlation for average quantum states only exist for higher level correlations than can be observed with $\mathcal{I}$. Similarly clustering also decays as a function of system size: generic quantum states have low transitivity of connections. Finally, we observe that disparity decays as $\frac{1}{L-1}$ for random

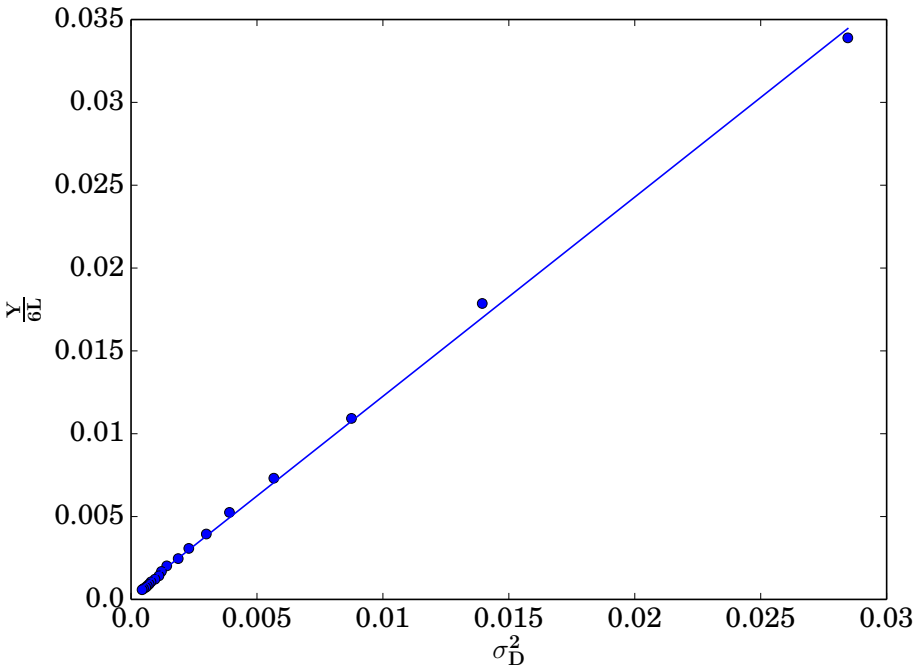

Fig. 3.5: *Relation between disparity and variance of network density for random adjacency matrices.* The average disparity of random networks normalized by system size is proportional to the variance of network density. A line of best fit is shown $Y/6L = 1.21\sigma_D^2$ with an $R^2 = 4 \times 10^{-6}$.

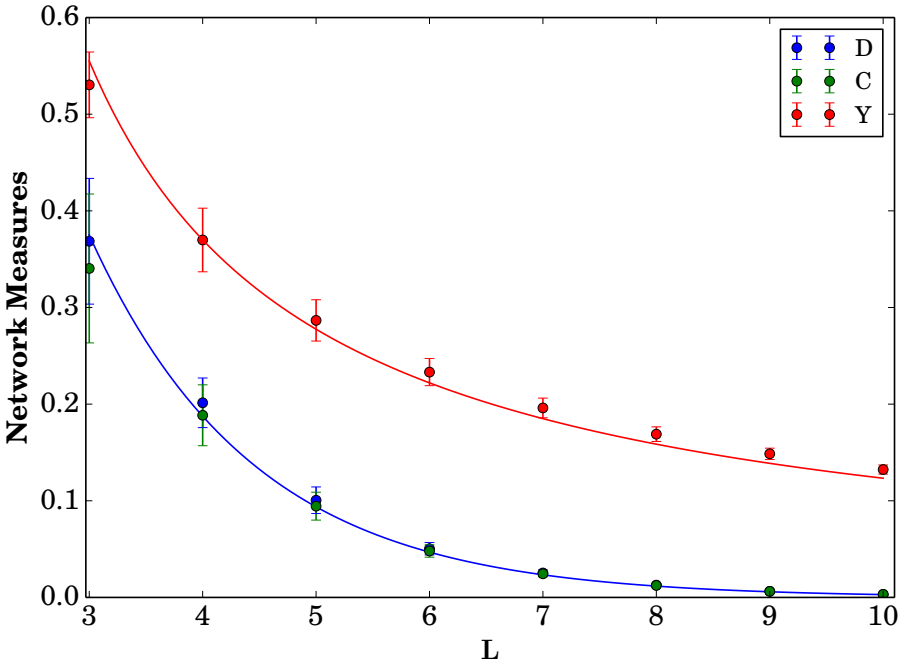

Fig. 3.6: *Network measures applied to adjacency matrices of random quantum states.* Network density, clustering coefficient, and disparity all decay as a function of L. Disparity is fit by the curve $\frac{1.1}{L-1}$ with $R^2 = 10^{-2}$, while network density and the clustering coefficient are fit by 3×2^{-L} with $R^2 = 2 \times 10^{-3}$ and $R^2 = 10^{-2}$ respectively. These estimates allow us to distinguish random quantum states from non-random quantum states in Chapter 6.

adjacency matrices and random quantum states. This tells us that networks from random adjacency matrices and random quantum states tend to have uniform connection strengths. From inequality (2.56) we can estimate the average mutual information between any two sites on a lattice of L qubits as

$$\mathcal{I}_{ij} = \frac{1}{2}\left(S_i + S_j - S_{ij}\right) \approx \frac{1}{2}\left(2\left(\log_2(2) - \frac{2^{2-L}}{2}\right) - 2\log_2(2) + \frac{2^{4-L}}{2}\right) = 2^{1-L}\,. \qquad (3.20)$$

Since network density is equal to the average quantum mutual information between all two sites in the lattice, we fit network density with functions of the form $a2^{-L}$. We find that network density is well fit by 3×2^{-L} as shown in Fig. 3.6. Since the clustering coefficient is equal to network density within error for large system sizes we use the same fit to estimate the clustering coefficient of networks of random quantum states. Using these fits we are able to estimate the value of our complex network measures for arbitrary system sizes. In Chapter 6 this allows us to quantify non-random structure in the quantum mutual information networks generated by Hamiltonian-based quantum cellular automata.

In Chapter 6 we also compare the quantum states generated by our QCA to well known quantum states like the $|W\rangle$ state, the $|GHZ\rangle$ state, and a cluster state $|C\rangle$. Cluster states are also known as graph states as they can be described by the links of a graph. A node in the graph corresponds to the degrees of freedom of a certain site. To prepare a cluster state one initializes the quantum state to an equal superposition of all states in the standard basis, $\psi = 1/\sqrt{2^L}\,|+ + ...+\rangle$. One then applies a controlled phase gate between each pair of sites in the lattice with an link in the corresponding graph. We choose to compare the quantum states generated by our quantum cellular automata to the cluster state corresponding to a network in which all nearest neighbors are connected. Since the controlled phase gate between sites 1 and 2 performs the mapping $|i_1 i_2\rangle \rightarrow (-1)^{i_1 i_2}\,|i_1 i_2\rangle$ [69] in the standard basis we can express the cluster state as

$$|C\rangle = \frac{1}{\sqrt{2^L}} \sum_{i_1,..i_L=0}^{1} \prod_{j=1}^{L-1} (-1)^{i_j i_{j+1}} |i_1 i_2 ... i_L\rangle \ . \tag{3.21}$$

Computing the quantum mutual information adjacency matrices of $|C\rangle$ for $L \in [2, 8]$ we find that for $L \geq 4$ the entries of the adjacency matrix are $\mathcal{I}_{12} = \mathcal{I}_{21} = \mathcal{I}_{L-1L} = \mathcal{I}_{LL-1} = \frac{1}{2}$, with all other entries being zero. This corresponds to the network with a link between sites 1 and 2, and a link between sites $L-1$ and L. The quantum mutual information network of the cluster state has

$$D = \frac{2}{L(L-1)} \, , C = 0 \, , \text{ and } Y = 4/L \, . \tag{3.22}$$

There are only ever two links, so the network becomes more sparse as system size is increased. Furthermore the links are always intransitive since there are no closed loops of length three. The nodes at the boundaries have a single dominant connection to their nearest neighbor, and all other nodes have zero disparity, resulting in disparity decaying as $1/L$ instead of $1/(L-1)$ as for random quantum states. We also verified our calculation of the quantum mutual information adjacency matrices of the cluster state by comparing to numerics as shown in Fig. 3.7. We observe that the quantum mutual information adjacency matrices of $|C\rangle$ are very similar to those of

$$|\phi_-\rangle = |0\rangle^{\otimes L/2-1} \otimes \frac{1}{\sqrt{2}} \left(|00\rangle - |11\rangle\right) \otimes |0\rangle^{\otimes L/2-1} \ , \tag{3.23}$$

a spin singlet centered on a lattice of L qubits. In [45] it was found that the network density, clustering coefficient, and disparity of the network of the spin singlet centered on a lattice of L qubits

$$D = \frac{2}{L(L-1)} \, , C = 0 \, , \text{ and } Y = 2/L \, . \tag{3.24}$$

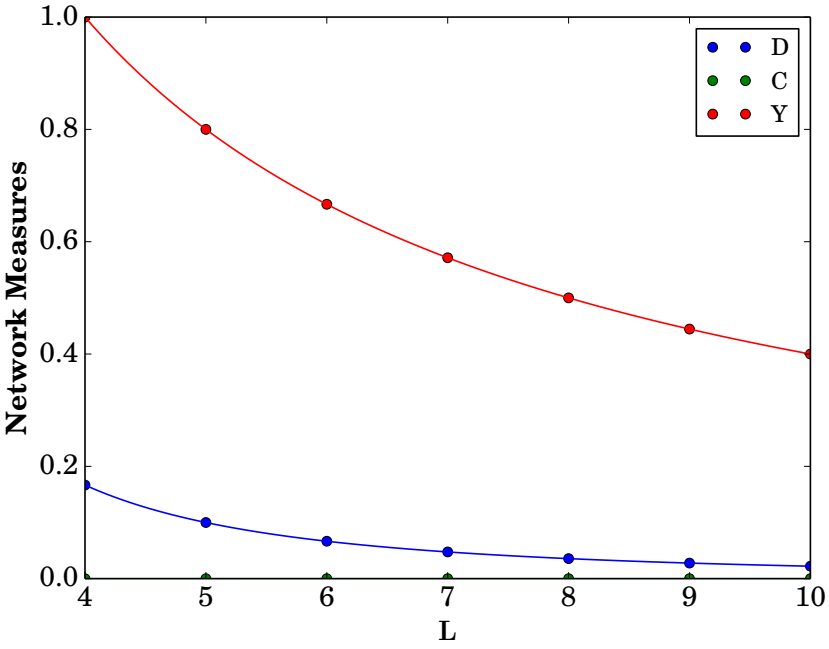

Fig. 3.7: *Network measures applied to adjacency matrices of cluster states.* Numerical calculations of complex network measures computed on quantum mutual information matrices of a cluster state are compared to analytic prediction. Unlike random quantum states, density of the cluster state decays algebraically and the clustering coefficient is always exactly zero. Finally disparity scales as $1/L$ for cluster states instead of $1/(L-1)$ as observed for random quantum states.

L. Hillberry also derived formulas for the network density, clustering coefficient, and disparity of

$$|S\rangle = \frac{1}{\sqrt{2^{L/2}}} \left(|01\rangle - |10\rangle\right)^{\otimes L/2} , \tag{3.25}$$

an array of singlets. The quantum mutual information adjacency matrices of the singlet array, $|S\rangle$, have

$$D = \frac{1}{L-1} , C = 0 , \text{ and } Y = 1 . \tag{3.26}$$

It was also shown in [45] that the $|GHZ\rangle$ state,

$$|GHZ\rangle = \frac{1}{\sqrt{2}} \left(|0\rangle^{\otimes L} + |1\rangle^{\otimes L}\right) , \tag{3.27}$$

has quantum mutual information adjacency matrices with

$$D = \frac{1}{2} , C = \frac{1}{2} , \text{ and } Y = \frac{1}{L-1} . \tag{3.28}$$

Finally, by deriving the constant quantum mutual information adjacency matrix of the $|W\rangle$ state

$$|W\rangle = \frac{1}{\sqrt{L}} \left(|10...0\rangle + |010...0\rangle + ... + |0...01\rangle\right) , \tag{3.29}$$

it was shown in [45] that the network density, clustering coefficient, and disparity of these networks are

$$D = \mathcal{I}^W , C = \mathcal{I}^W , \text{ and } Y = \frac{1}{L-1} \tag{3.30}$$

where $\mathcal{I}^W = \frac{1}{L} + \frac{1}{2}\log_2(L) + \frac{L-2}{2L}\log(L-2) - \frac{L-1}{L}\log(L-1)$. We have also computed the central bond entropy, S_{bond}, of $|C\rangle$, $|\phi_-\rangle$, $|GHZ\rangle$, and $|W\rangle$. We have found that they all have $S_{\text{bond}} = 1$ independent of system size. The singlet array has $S_{\text{bond}} = 1$ for $L \in \{10, 14, 18\}$ and $S_{\text{bond}} = 0$ for $L \in \{12, 16, 20\}$. This is because for $L \in \{10, 14, 18\}$ sites $L/2$ and $L/2+1$ are completely entangled while for $L \in \{12, 16, 20\}$ sites $L/2$ and $L/2+1$ are not entangled.

In Chapter 6 this analysis allows us to differentiate the states produced by our QCA from these well-known states.

CHAPTER 4

COMPLEX NETWORK ANALYSIS OF QUANTUM PHASE TRANSITIONS

In this chapter we apply the complex network measures developed in Chapter 3 to study quantum phase transitions in two models of quantum many body physics, the transverse Ising and Bose-Hubbard models. We find that network density, clustering coefficient, disparity, and Pearson R correlation all show systematic finite-size scaling towards the critical points of these two models. Furthermore, we identify the boundary separating the Mott Insulator phase from the superfluid phase in the Bose-Hubbard model by extremization of network density, clustering coefficient, and disparity. By successfully identifying phase transitions in models of distinct many body physics we show that complex network measures are able to detect emergent phenomena in quantum many body systems. For the phase transitions we consider we find that our complex network measures are low in one phase, higher in the other phase, and intermediate at the quantum critical points of both models. This is similar to the intermediate values of complex network measures observed in Chapter 6 where we find that quantum cellular automata generate quantum states with complex network measures intermediate between random states and well characterized quantum states. Intermediate values are one of our quantifications of complexity, so that in some sense quantum critical points have the highest complexity of all static ground states explored in the quantum phase diagrams of these systems.

While complex networks have appeared in the context of quantum systems in previous work [18, 70] our development of quantum mutual information complex network analysis is an innovation. The authors of [18] provide a new theoretical scheme for the distribution and transmission of quantum entanglement. The authors of [70] develop a transmission scheme for photons in cavities. Our complex network approach is different. We focus on quantifying the structure of quantum mutual information networks. We thereby provide a

new tool to analyze data from the networked quantum systems proposed in [70]. While both transverse Ising and Hubbard phase diagrams have been understood with more standard approaches, we chose to study these models as a proof of principle for quantum mutual information complex network analysis. We emphasize that in emerging quantum simulator technologies identifying the relevant order parameter may be nontrivial. However, since quantum mutual information is bounded from below by all possible two point correlations it will always identify the relevant correlations in such systems [24]. Furthermore, such systems may break translation invariance as described in [28]. Therefore the correlations in these systems will likely not exhibit simple monotonic decay. In the absence of monotonic decay of correlations there is no clear correlation length defining the system. Instead the order of such systems may be characterized by patterns of two point correlations. We propose that complex network measures are an ideal tool to quantify the patterned correlations that will be observed in quantum simulators.

4.1 Transverse Ising and Bose-Hubbard Quantum Many-Body Hamiltonians

The Hamiltonian of the transverse Ising model is defined as

$$\hat{H}_I = -J \sum_{i=1}^{L-1} \hat{\sigma}_i^z \hat{\sigma}_{i+1}^z - Jg \sum_{i=1}^{L} \hat{\sigma}_i^x \,, \tag{4.1}$$

where $\left[\hat{\sigma}_j^\alpha, \hat{\sigma}_k^\beta\right] = 2\mathrm{i}\delta_{jk}\epsilon_{\alpha\beta\gamma}\hat{\sigma}_k^\gamma$. The first term of the Hamiltonian is the coupling between nearest neighbors on the lattice. For $J > 0$ the spins interact ferromagnetically, minimizing energy by aligning with each other. We set $J = 1$ in our study. The second term models an external magnetic field in the x direction. The parameter g controls the strength of an external magnetic field that the spins align with as $g \gg 1$. For small values of the external magnetic field strength spins align in their ground state. For finite systems the ground state respects the Z_2 symmetry of the model forming a GHZ-like state as depicted in Fig. 4.1. The external field disorders spins in the z direction and induces a quantum phase transition from a ferromagnetic phase to a paramagnetic phase at the critical point $g_c = 1$ in the

thermodynamic limit [34].

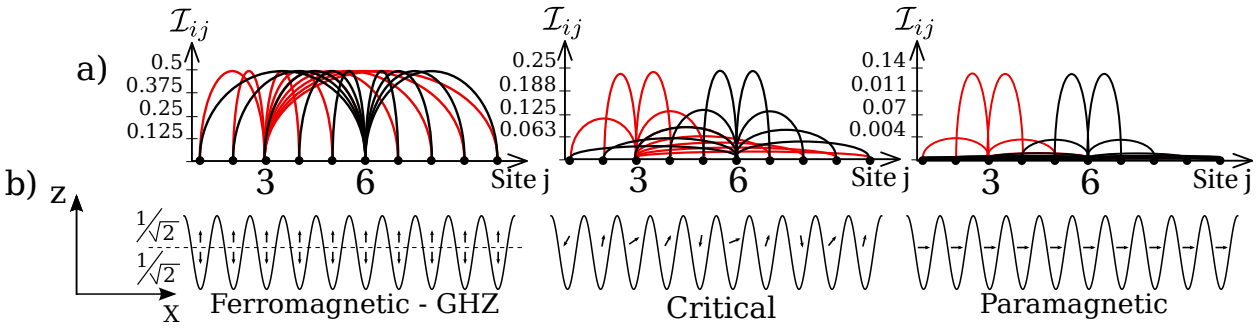

Fig. 4.1: *Sketch of mutual information complex network.* A chain of L quantum bits (qubits) in a sinusoidal potential, for the transverse Ising model, the "fruit-fly" of quantum many body physics. (a) Links originating from site 3 (red, $\mathcal{I}_{3j}$) and site 6 (black, $\mathcal{I}_{6j}$) for the mutual information complex network $\mathcal{I}_{ij}$, corresponding to phases and critical point in (b). In this weighted complex network, the height of the links in our sketch denotes their relative strength; note descending vertical axes from left to right. The entire complex network is far too dense to depict, so we show just two representative sites. (b) Sketch of ferromagnetic phase (left), critical point (center), and paramagnetic phase (right). The sinusoidal potential corresponds to an optical lattice for ultracold atoms or molecules. In the ferromagnetic case, the dashed line indicates a superposition between the Z_2 symmetric states all spin-up and all spin-down.

The Hamiltonian of the Bose-Hubbard model is defined as

$$\hat{H}_B = -J\sum_{i=1}^{L-1}(\hat{b}_i^\dagger \hat{b}_{i+1} + \hat{b}_i \hat{b}_{i+1}^\dagger) + \frac{1}{2}U\sum_{i=1}^{L}\hat{n}_i(\hat{n}_i - \hat{1}) - \mu\sum_{i=1}^{L}\hat{n}_i\,, \tag{4.2}$$

where $\left[\hat{b}_i, \hat{b}_j^\dagger\right] = \delta_{ij}$ are bosonic annihilation and creation operators and $\hat{n}_i = \hat{b}_i^\dagger \hat{b}_i$. The Bose-Hubbard Hamiltonian is a model for ultracold atoms in optical lattices. The first term of the Hamiltonian models the tunneling of atoms between nearest neighbor wells of the optical lattice. The parameter J sets the energy gained by atoms when they tunnel between sites of the lattice. The second term models the interaction between particles occupying the same well. The parameter $U > 0$ sets the strength of the repulsive on-site interaction felt by atoms occupying the same site. When the normalized tunneling J/U is large, atoms are free to tunnel between nearest neighbor sites and they delocalize across the lattice as a superfluid (SF). When J/U is small the atoms become localized so that there are a well defined number of particles on each site and the atoms enter the Mott insulator (MI) phase.

The final term of the Bose-Hubbard model is a chemical potential term. The parameter μ sets the energy to add a particle to the lattice. We study the Bose-Hubbard model in the canonical ensemble, for which the total number of particles on the lattice is fixed. Therefore, the third term of our Hamiltonian is a constant energy shift. The μ term in Fig. 4.3(a) and (c) is calculated from the difference in the ground state energy between simulations that have N particles and simulations that have $N+1$ particles, $\mu(N) = E(N+1) - E(N)$. The Mott insulator phase is characterized by an integer density N/L. For small values of J/U the energy required to add a particle or hole to the Mott insulator is large, characterizing the gapped nature of the Mott phase. as J/U increases this gap closes forming the boundaries of the Mott insulator phase in the $(\mu/U, J/U)$ plane. There are multiple Mott lobes in the phase diagram of the Bose-Hubbard model, each characterized by its density. We study the boundaries of the Mott lobe with unit filling $N/L = 1$. There are two kinds of phase transitions of the Bose-Hubbard model. There is a mean field phase transition in which the system transitions from integer to non-integer density as it enters the superfluid phase, this is known as the commensurate to incommensurate phase transition. There is also a BKT transition in which the system transitions from the Mott insulator phase to the superfluid phase at constant density $N/L = 1$. The best estimate of the BKT transition point is currently $(J/U)_c = 0.305$ [71]. The authors of [71] compute this estimate via a scaling ansatz for the single particle gap. They identify the critical point $(J/U)_c$ as the point for which the rescaled gaps of all system sizes intersect.

4.2 Complex Network Analysis of Transverse Ising and Bose Hubbard Ground States

We begin our analysis by computing the ground states of the transverse Ising and Bose-Hubbard models using OpenMPS. We set $\chi_{\max} = 2000$ and $\epsilon = 10^{-12}$. The energy variance of our ground states always satisfies inequality (2.58) with $\epsilon_v = L \times 10^{-8}$. In order to accurately converge our quantum ground states we have assured that inequality (2.58) is satisfied for $\chi < \chi_{\max}$. Since OpenMPS is a variational algorithm, if two states have nearly degenerate

energy levels the algorithm may converge to a superposition of these states, resulting in incorrect quantum mutual information networks. In the transverse Ising model the first excited state is nearly degenerate with the ground state for $g < 1$. We therefore add a perturbative parity field, $-\prod_i \hat{\sigma}_i^z$, to the transverse Ising model in order to separate these two energy levels [72]. This term commutes with the Hamiltonian, and since the ground state of the transverse Ising model is not degenerate it does not modify the ground state. In our numerical simulations of the Bose-Hubbard model we allow up to 5 particles on site, truncating the local dimension to $d = 6$. We chose $d = 6$ as in [73] it is noted that simulations with $d = 8$ do not produce visible changes in entanglement measures computed on the ground state of the Bose-Hubbard model for simulations with $0 < N/L < 2.5$. For the transverse Ising model we compute the ground states for 321 points evenly spaced in the interval $g \in [0, 2]$, for system sizes

$$L \in \{20, 40, 60, 80, 100, 140, 160, 200, 240, 280, 320, 360, 500\}\,.$$

We then compute network density, clustering coefficient, disparity, and Pearson R correlation on the quantum mutual information adjacency matrices of each of these quantum states as defined in Eqs. (3.2), (3.5) , (7.6), and (3.7) in Chapter 3. For the Bose-Hubbard model at unit filling we compute these network measures at 81 points evenly spaced in the interval $J/U \in [0, 0.4]$ for system sizes

$$L \in \{14, 18, 22, 26, 30, 34, 38, 42, 46, 60, 70, 80, 90, 100, 110, 120, 130, 140, 150\}$$

to study the BKT phase transition. We present these results in Fig. 4.2. To study the commensurate to incommensurate phase transition of the Bose-Hubbard model we compute the ground states of a lattice of length $L = 42$ for a total number of particles $N \in [0, 63]$ and for 81 points evenly spaced in the interval $J/U \in [0, 0.4]$. For each value of J/U we compute $\mu(N)$ for all $N \in [0, 63]$. We then compute network density, clustering coefficient,

and disparity for all values of $(J/U, \mu/U)$.

In the traditionally ordered (ferromagnetic) phase of the transverse Ising model correlations span the entire lattice as the system is in a many body superposition of all spin up and all spin down. If a measurement is made on any qubit of the lattice it collapses the quantum state of the entire system, determining the state of every other qubit in the lattice. This is an indication of the fragility of such states [74]. Since any two qubits in the lattice have become correlated in such a state all qubits have large quantum mutual information with all other qubits. Specifically, for the GHZ state $I_{ij} = 0.5$ between all qubits. For such networks all connections that can exist do exist, making the network density large in the ferromagnetic phase. Clustering behaves similarly to network density except that it develops a local minimum near the critical point of the transverse Ising model. This local minimum is due to the average number of connected triples temporarily growing faster than the transverse magnetic field strength for the average number of triangles. Physically this could be because the length scale of correlations has become as long as one lattice spacing but not two, resulting in a period of rapid increase in quantum mutual information between nearest neighbors relative to second nearest neighbors. In contrast with network density and clustering, disparity asymptotically approaches $\frac{1}{L-1}$ in the ferromagnetic phase and is thus governed by the size of the system. Disparity increases in the paramagnetic regime where correlations decay exponentially. This is due to spins becoming more correlated with their nearest neighbor relative to other qubits in the network. The Pearson correlation between the middle lattice sites, R, develops a non-analyticity near $g = 1$ as the system size is increased, evidenced by the cusp developing in Fig. 4.2. Qualitatively, R is low in both the ferromagnetic phase and paramagnetic phase due to the collapse of the data onto single points in the $\left(\mathcal{I}_{\frac{L}{2},i}, \mathcal{I}_{\frac{L}{2}+1,i}\right)$ plane when $g \ll 1$ and when $g \gtrsim 2$. In contrast near criticality the weights display an approximately linear relationship. In this way R measures non-trivial correlation that occurs near criticality. In the ferromagnetic phase the network is completely connected. In the paramagnetic phase the network is completely unconnected. Both net-

works are trivial to describe. In the paramagnetic phase there is negligible quantum mutual information between sites that are not nearest neighbors. In the ferromagnetic phase there is the other extreme; a completely connected network in some sense dual to the paramagnetic network. Near criticality the pattern of connections contains more structure than it does on either side of the critical point. Disparity and density both appear to approach limiting curves as we increase our system size. Normalizing each quantity results in a set of normalized curves ($\tilde{Y}$ and $\tilde{D}$) whose intersections approach $g_c = 1$ according to a power law as shown in Table 4.1. To normalize network density we divide it by its value at $g = 0$ for $L = 500$. In contrast, for disparity we divide it by its value at $g = 2$ for $L = 500$.

The Bose-Hubbard model at unit filling displays similar behavior in network density, clustering coefficient and disparity as is seen in the transverse Ising model. By increasing the strength of the normalized tunneling J/U the system transitions from a phase with low network density to a phase with high network density as the system enters the superfluid phase. In the superfluid phase particles all occupy the same non-local single particle state, and the system is spatially entangled. The quantum mutual information between lattice sites may be due to the density-density correlations between particles in different lattice sites. Interestingly, as system size is increased the network density of the superfluid phase decreases, in contrast to the entangled phase of the transverse Ising model where, for increasing system size, the network density increases. This may be due to the different statistics of the noise in these two models: as described in [52] the statistics of atomic noise measurements determines whether they are observable in macroscopic systems. From the Pearson R correlation we can also see that the networks of the superfluid in the Bose-Hubbard model are structured differently than the networks of the GHZ-like states in the ferromagnetic phase of the transverse Ising model. In the ferromagnetic phase of the transverse Ising model the quantum mutual information between any two qubits approaches the same constant value; in contrast the quantum mutual information between any two qubits decays as a function of separation distance in the superfluid phase of the Bose-Hubbard model.

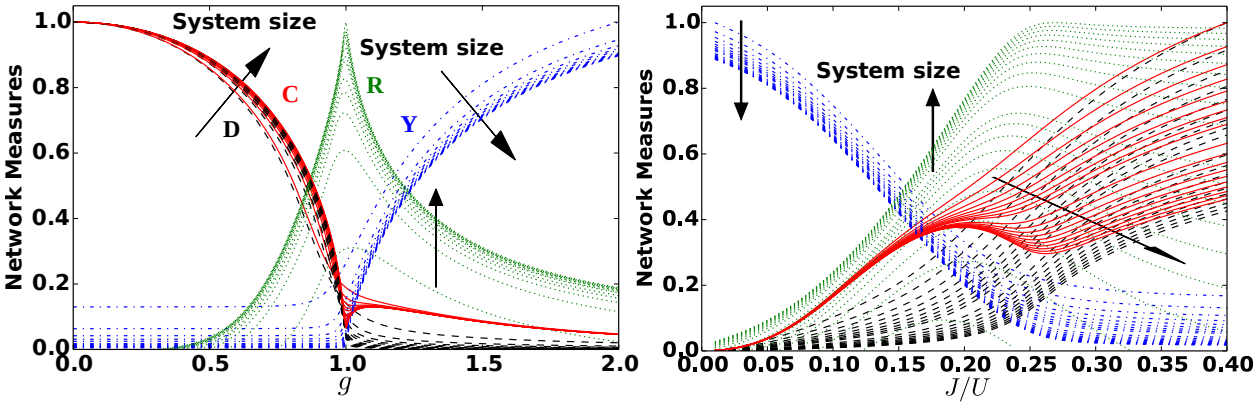

Fig. 4.2: *Complex network measures on the mutual information.* (a) Transverse quantum Ising model describing quantum spins (qubits). The clustering coefficient C (red) and density D (dashed black) serve as order parameters for the ferromagnetic phase. The disparity$Y$ (dot-dashed blue) identifies the short range correlations of the paramagnetic ground state. The Pearson correlation coefficient R (dotted green) develops a cusp near the critical point $g_c = 1$, identifying a structured nature to correlations near criticality. (b) Bose Hubbard model describing massive particles for commensurate lattice filling, with BKT crossover occurring in the limit $L \to \infty$ at a ratio of tunneling J to interaction U of $(J/U)_{\mathrm{BKT}} = 0.305$; for smaller system sizes, the effective critical point [73] can be as small as $(J/U)_{\mathrm{BKT}} \simeq 0.2$. The density and clustering coefficient grow as spatial correlations develop in the superfluid phase. The disparity is high in the Mott insulator phase where correlations are short-ranged. Critical/crossover behavior is most evident in derivatives of these measures, see Fig. 4.3 and Table 4.1. Note: all network measures have been self-normalized to unity for display on a single plot.

4.3 Finite Size Scaling

In order to estimate the location of the critical point of the transverse Ising model and the BKT transition point of the Bose-Hubbard model we perform finite size scaling analysis. We define the positions of the effective critical points $g_c(L)$ and $(J/U)_c(L)$ for these two models as points of maximum first and second derivative of our complex network measures. By tracking these effective critical points as a function of system size we are able to extrapolate to the thermodynamic critical point. We also track other features of our complex network measures like the maximum of the Pearson R correlation and the local minima of the clustering coefficient shown in Fig. 4.2. For each system size we interpolate the data shown in Fig. 4.2 with 5^{th} order polynomials using the scipy function `interpolate.splrep` [75]. We locate the position of maximum absolute value of the first and second derivative of clustering coefficient, network density, and disparity by sampling this polynomial at 10000 times the resolution of the original data and selecting the value of the control parameter (g for transverse Ising and J/U for Bose-Hubbard) that maximizes the absolute value of the first or second derivative. Some measures have multiple maxima in the absolute value of their first and second derivatives. To uniquely define the maximum we track we also impose the following conditions:

$$\frac{\mathrm{d}^2 D}{\mathrm{d}g^2}, \frac{\mathrm{d}^2 C}{\mathrm{d}g^2} > 0\,, \tag{4.3}$$

$$\frac{\mathrm{d}C}{\mathrm{d}g}, \frac{\mathrm{d}^2 R}{\mathrm{d}g^2} < 0\,, \tag{4.4}$$

$$\frac{\mathrm{d}^2 D}{\mathrm{d}(J/U)^2}, \frac{\mathrm{d}C}{\mathrm{d}(J/U)}, \frac{\mathrm{d}^2 C}{\mathrm{d}(J/U)^2}, \frac{\mathrm{d}^2 Y}{\mathrm{d}(J/U)^2}, \frac{\mathrm{d}R}{\mathrm{d}(J/U)} > 0\,, \tag{4.5}$$

and

$$\frac{\mathrm{d}^2 R}{\mathrm{d}(J/U)^2} < 0\,. \tag{4.6}$$

Even with these conditions imposed the maxima are not uniquely defined for the first and second derivatives of the clustering coefficient of the Bose-Hubbard model at unit filling. We

therefore also impose the condition $(J/U)_c(L) > 0.15$ for the clustering coefficient of the Bose-Hubbard model at unit filling. The inequality $(J/U)_c(L) > 0.15$ assures that we do not track a maximum at $J/U \approx 0.12$ in the derivative of the clustering coefficient.

All estimates of critical points included in Table 4.1 are made by fitting the effective critical points as a function of system size to power laws of the form defined in Eqs. (2.40) and (2.41) using the SciPy function `optimize.curve_fit` [75]. The `p0` argument of this module allows one to specify initial values for the parameters to be fit to. For the Bose-Hubbard model at unit filling the initial estimates of $(J/U)_c$, A, and $1/\nu'$ are set to 0.272, -0.211, and 1.67 respectively. We use these initial values for all estimates of the BKT critical point. We find that our complex network analysis estimates the critical point of the transverse Ising model to within 0.01% of its known value $g_c = 1$. Furthermore, we are able to estimate the position of the BKT transition to within 3.6% of its accepted value of $J/U = 0.305$ with just 150 lattice sites.

By extremizing network density, clustering coefficient, and disparity on a lattice of 42 sites as a function of each value of (J/U) we estimate the boundaries of the Mott lobe as shown in Fig. 4.3. Minimization of density results in similar estimates as maximization of disparity. However, minimization of the clustering coefficient leads to slightly worse estimates as shown in Fig. 4.3. Note that we extremize the data above and below the Mott lobe separately.

4.4 Conclusions

In conclusion, we have shown that complex network measures built on taking the quantum mutual information as a weighted adjacency matrix reliably estimate quantum critical points for well-known quantum-many body models, in particular the transverse Ising and Bose-Hubbard models. These models include three classes of phase transitions, Z_2, mean field superfluid/Mott insulator, and a BKT crossover; in each case we obtain rapidly converging accuracy for critical point values. Our work sets the stage for application of a new set of quantum measures to provide insight into the complexity of quantum systems where traditional correlation measures are at best weakly applicable. In Chapters 5 and 6 we will

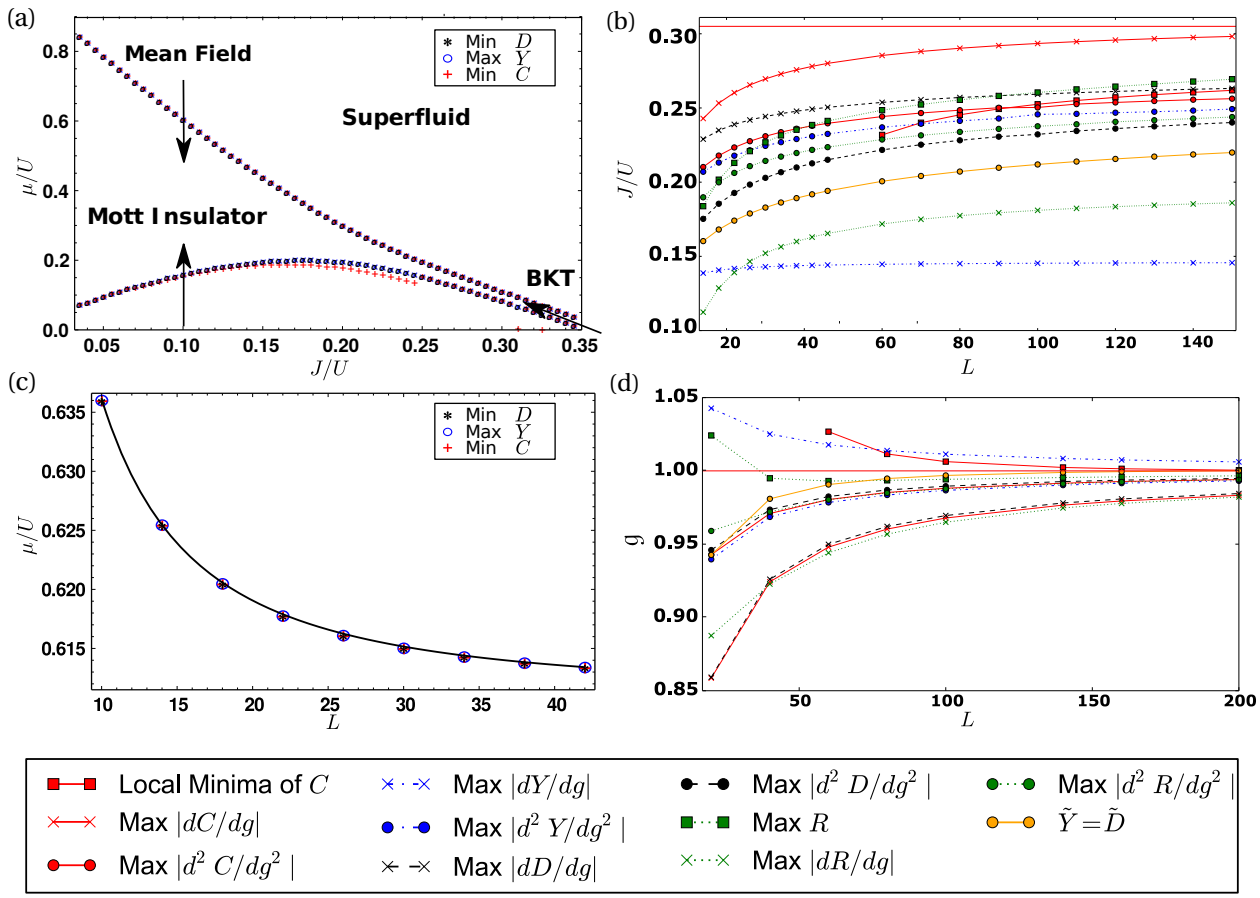

Fig. 4.3: *Finite-size scaling for the Bose-Hubbard model and transverse Ising model.* (a) BHM quantum phase diagram for fixed $L = 42$ showing superfluid and Mott Insulating phases with mean field phase transition along the Mott lobe and a BKT transition at its tip. (b) BHM BKT transition at unit filling. Scaling in $1/L$ places the critical point at $(J/U)_{\mathrm{BKT}} = 0.316$ (clustering, solid red), 0.284 (disparity, blue dot-dashed) and 0.282 (density, black dashed), respectively. Compare to the best value to date [76, 71] of 0.305, or the Luttinger liquid prediction of 0.328. (c) Approaching the BHM mean field superfluid/Mott insulator transition for fixed $(J/U) = 0.1$. Maximum disparity (blue circles), minimum clustering (red plus signs), and minimum density (black star) scale towards the commensurate-incommensurate phase boundary and lie closely on top of each other. (d) Scaling of multiple measures and their derivatives for the TIM, see also Table 4.1.

Table 4.1: *Quantitative finite-size scaling analysis of quantum critical points.* Estimates for the critical point g_c and $(J/U)_{\mathrm{BKT}}$ and scaling exponents ν, ν' for the transverse Ising and Bose Hubbard models, respectively, based on three complex network measures on the mutual information. We include in our analysis first and second derivatives (FD, SD) since bare measures are often insufficient, an effect well-known from one-point entanglement measures like von Neumann entropy. We also note three other features: the local minima (LM) in the clustering coefficient C, the local maximum in Pearson R correlation (LMA), and an intriguing point where normalized disparity is equal to normalized density ($\tilde{Y} = \tilde{D}$). Entries are left blank where no significant feature appears in the complex network curves. Our complex network measures clearly perform as well or better than standard measures, particularly for the still improving estimates for the BHM BKT point [76].

Fit Parameter	Network Density D		Disparity Y		Clustering Coefficient C			Pearson Correlation R			$\tilde{Y} = \tilde{D}$
	FD	SD	FD	SD	LM	FD	SD	LMA	FD	SD	
g_c	1.001 ±0.001	1.001 ±0.001	1.001 ±0.002	0.999 ±0.001	0.999 ±0.001	1.001 ±0.001	1.001 ±0.001		1.02 ±0.001	1.007 ±0.001	1.002 ±0.001
ν	1.07 ±0.01	1.02 ±0.03	1.2 ±0.05	1.03 ±0.02	0.36 ±0.01	1.09 ±0.01	1.05 ±0.02		1.76 ±0.16	1.82 ±0.15	0.65 ±0.01
$(J/U)_{\mathrm{BKT}}$	0.281 ±0.001	0.282 ±0.001	0.146 ±0.001	0.284 ±0.001	0.275 ±0.001	0.316 ±0.001	0.278 ±0.001	0.291 ±0.06	0.199 ±0.001	0.272 ±0.002	
ν'	2.27 ±0.06	2.58 ±0.04	0.933 ±0.02	2.88 ±0.17	0.79 ±0.03	1.69 ±0.01	2.07 ±0.07	1.56 ±0.06	1.25 ±0.01	2.3 ±0.1	

apply our new methods to study the dynamics of quantum cellular automata [40, 77].

CHAPTER 5

CONVERGENCE OF QUANTUM CELLULAR AUTOMATA

In Chapter 4 we implemented network-based complexity measures successfully in OpenMPS simulations of quantum phase transitions. We now turn to quantum cellular automata and far-from-equilibrium quantum many-body dynamics, and examine the applicability of powerful OpenMPS codes to this new context, in particular to the network-based complexity measures introduced in Chapter 3 and applied in Chapter 4. Specifically, we will evaluate matrix product state code as a means of evolving quantum states under the BCM Hamiltonian and a Hamiltonian motivated by rule 6 of [45]. We find that OpenMPS simulations of hundreds of random Fock states and local defect initial conditions abruptly reach the entanglement cutoff imposed by convergence parameter $\chi_{\max}$. This abrupt saturation of χ implies that OpenMPS is not a viable numerical method to study the dynamics of the BCM Hamiltonian for most initial conditions. We also perform a case study of the quantum blinker reported in [40]. Despite using one of the latest forms of time evolution available for OpenMPS methods [57] we are unable to reproduce the quantum blinker under the initial conditions specified in [40]. We find that this initial condition instead rapidly equilibrates to a highly entangled quantum state. However, under a different choice of initial condition we find that OpenMPS is able to reproduce a quantum blinker pattern observed in exact simulation. For this single exceptional initial condition OpenMPS is able to accurately compute several measures of complexity. We conclude the chapter by studying the evolution of a single initial condition under the rule 6 Hamiltonian. We find it produces lowly entangled dynamics for this initial condition. This suggests OpenMPS may be able to efficiently simulate the dynamics of the rule 6 Hamiltonian.

5.1 OpenMPS Convergence Analysis of BCM Hamiltonian

In contrast to the many and well-known studies [78, 79, 80, 81, 82, 83, 84, 85] of the dynamics of quantum quenches, in which the initial condition is a ground state, we instead study the evolution of various non-stationary initial conditions under the BCM Hamiltonian defined in Eq. (2.42). We begin our analysis of this Hamiltonian by performing a scaling study in the convergence parameter $\chi_{\max}$. As described in Chapter 2, χ is the number of singular values that are kept in the singular value decomposition of a quantum state. As such, χ is a measure of the many body entanglement of a quantum state. Matrix product state methods can simulate larger lattices than can be simulated using exact diagonalization because physically relevant quantum states often have singular values that decay exponentially quickly [46]. This approach results in an optimized low-dimensional representation in Hilbert space which is only polynomial, rather than exponential in the system size, effectively circumventing quantum blow-up. Therefore in simulating quantum states with matrix product state methods one may keep a small number of singular values and still achieve a useful representation of the quantum state. In simulating quantum many body dynamics OpenMPS increases χ in order to satisfy inequality (2.59) until $\chi = \chi_{\max}$. In inequality (2.59), ϵ determines how many singular values are kept by OpenMPS as long as $\chi < \chi_{\max}$. Once $\chi_{\max}$ is reached we no longer have a converged estimate of the quantum state. However, one may compute the Schmidt error ε_s of a simulation in order to estimate the error made by OpenMPS. The Schmidt error is the sum of the singular values that are neglected by OpenMPS during a simulation. We find that after saturation of $\chi_{\max}$ the Schmidt error is approximately constant for a few units of time before rapidly increasing. By performing analyses of χ, and ϵ we are able to quantify how many lattice sites our Hamiltonian is able to reliably evolve and under what choice of initial condition.

To assess the performance of OpenMPS we selected two kinds of initial conditions to evolve under the BCM Hamiltonian, defect initial conditions and random Fock state initial

conditions. Defect initial conditions are defined as

$$|\psi\rangle = |0\rangle^{\otimes \frac{L}{2}-n} |1\rangle^{\otimes 2n} |0\rangle^{\otimes \frac{L}{2}-n} , \tag{5.1}$$

for L even and

$$|\psi\rangle = |0\rangle^{\otimes \frac{L-(2n+1)}{2}} |1\rangle^{\otimes 2n+1} |0\rangle^{\otimes \frac{L-(2n+1)}{2}} . \tag{5.2}$$

for L odd. That is, for an even number of sites one initializes the quantum state with the $2n$ most central qubits in the $|1\rangle$ state, and all other qubits are initialized to the $|0\rangle$ state, while for an odd number of sites the $2n+1$ most central qubits are initialized to the $|1\rangle$ state while all others are initialized to the $|0\rangle$ state. The definition of defect initial conditions assures they are left-right symmetric. Random Fock state initial conditions are generated using the NumPy random number generator `random.rand` [68]. Each site i is initialized to the state $|1\rangle$ with probability p, and is initialized to the state $|0\rangle$ with probability $1-p$, resulting in L local states $|\psi_i\rangle$ for $i \in [1, L]$. We then form the tensor product of these L states to form a random Fock state

$$|\psi\rangle = \bigotimes_{i=1}^{L} |\psi_i\rangle . \tag{5.3}$$

The simulations we are capable of running using OpenMPS must have reasonable values for χ because simulation time scales $\approx \chi^3$ as shown in Fig. 5.1. The simulations of Fig. 5.1 have final time $t_f = 10.0$ and time step $\Delta t = 0.1$.

Running simulations with $\chi_{\max} = 320$ we found that for local defect initial conditions with $1 \leq n \leq 12$ all simulations reach $\chi_{\max}$ within 7 units of time, as shown in Fig. 5.2. Since all terms in our Hamiltonian are of order 1, the natural time scale for interaction within a single neighborhood is 1 unit of time.

Even with $\chi_{\max} = 320$ imposed these simulations take more than 96 hours to run for $t_f = 8$. If we did not impose this limitation on χ simulations would take even longer to complete. In Chapter 6, where we turn to Trotter-based time evolution, we will find that lattices of 20 qubits typically require at least 50 units of time to reach a central bond entropy

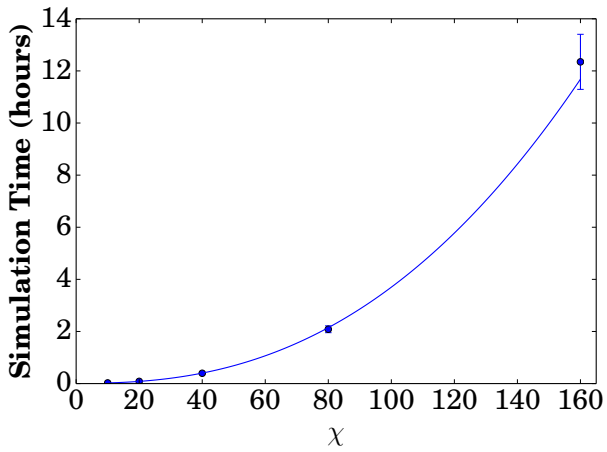

Fig. 5.1: *Scaling of OpenMPS simulation time with convergence parameter* χ. Here we show that for 26 qubits simulation time scales as $\chi^{2.54}$.

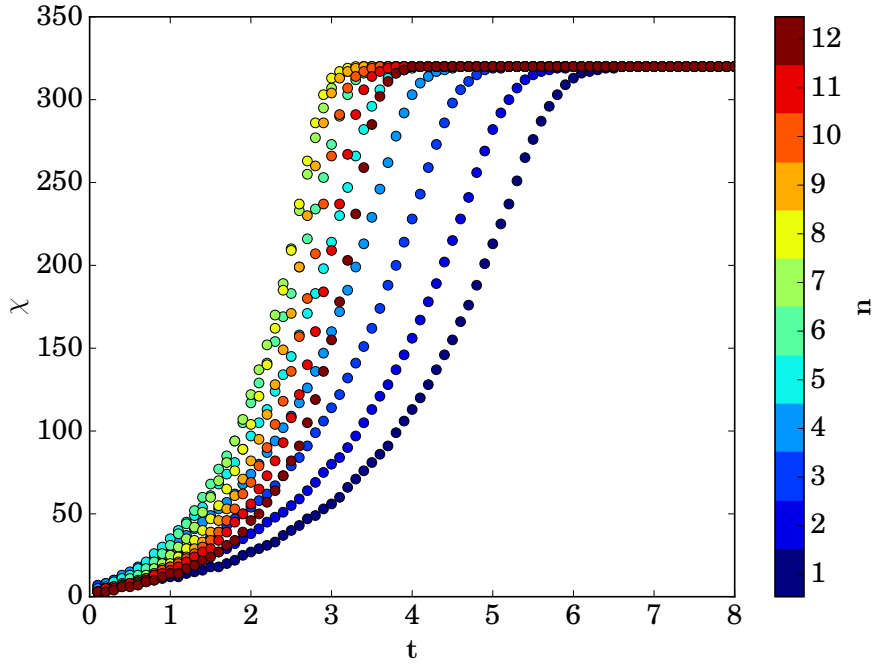

Fig. 5.2: *Saturation of* χ_{max} *for local defect initial conditions.* All local defect initial conditions with $1 \leq n \leq 12$ reach $\chi_{\max} = 320$ within 7 units of time when evolved under the BCM Hamiltonian and some take as little as 3 to 4 time units.

that is nearly constant. Since reaching this constant value takes longer for larger systems it is clear that OpenMPS is not a viable numerical method to simulate generic initial conditions over the relevant times scales of QCA.

We also studied the effect of the ϵ convergence parameter on the time to reach $\chi_{\max}$. As expected increasing ϵ increases the amount of time to reach $\chi_{\max}$ for random initial conditions with $p = 0.6$ as shown in Fig. 5.3. We choose $p = 0.6$ to avoid the extremes of $p = 0$ and $p = 1$

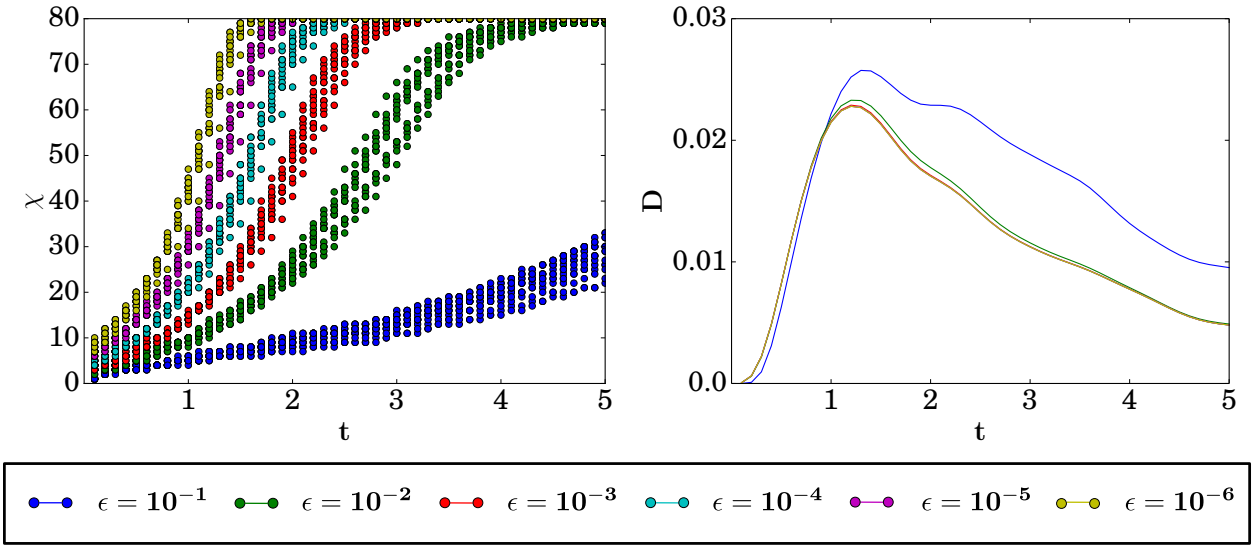

Fig. 5.3: *Dependence of χ on ϵ for random initial conditions.* Simulations with smaller values of ϵ are more accurate. However these simulations also require more time to simulate due to larger χ. Simulations with ϵ increased to 10^{-1} have large errors in network measures computed on the quantum mutual information complex networks.

as well as half filling at $p = 0.5$, which sometimes has special properties in quantum many body models, e.g. the Fermi Hubbard Hamiltonian [34]. We also spot-checked other values besides $p = 0.6$ and found similar results. These simulations have $\chi_{\max} = 80$. Increasing ϵ could allow simulations to be run more quickly, and thus make OpenMPS a viable numerical procedure. However, we find that increasing ϵ results in large errors of complex network measures as shown in Fig. 5.3.

We have also included a study of the time to reach $\chi_{\max}$ for random Fock state initial conditions with $p \in [0.2, 0.3, 0.4, 0.5, 0.6, 0.7, 0.8, 0.9]$ and as a function of the initial filling

factor $\rho = (1/L)\sum_{i=1}^{L}\langle\hat{n}_i(0)\rangle$. We display our results in Fig. 5.4 and Fig. 5.5. Both Fig. 5.4 and Fig. 5.5(a) demonstrate that for intermediate values of the filling factor the time to reach $\chi_{\max}$ is reduced. Interestingly, for local defect initial conditions we find that the time

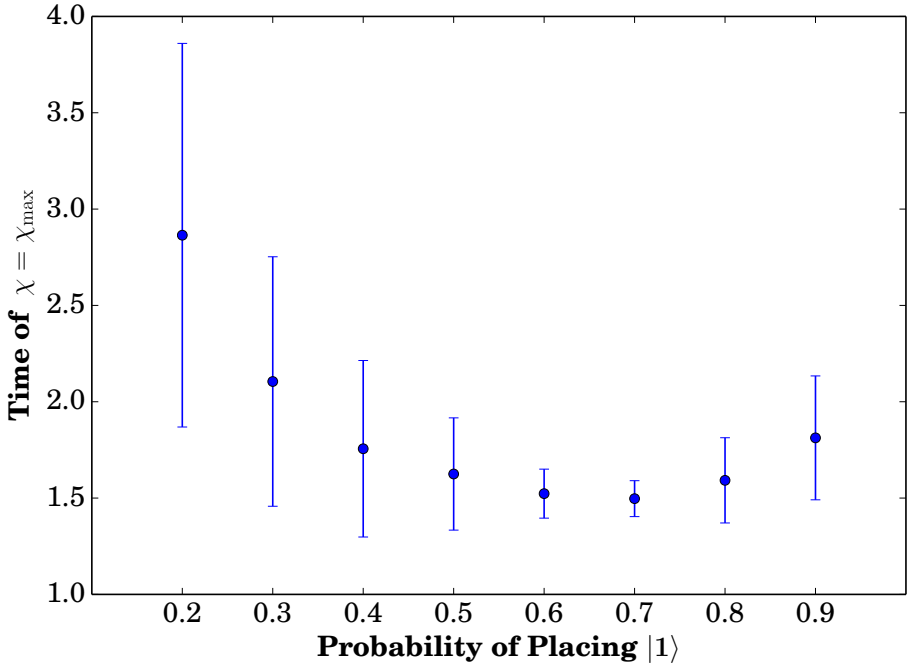

Fig. 5.4: *χ_{max} saturation time of random Fock state initial conditions.* Random Fock states with an intermediate value of the probability of placing $|1\rangle$ at any particular site reach $\chi_{\max}$ earlier.

to reach $\chi_{\max}$ changes linearly with density, with a slope that is different above and below some critical filling factor. For small values of p there is an increase in the variance of the time to reach $\chi_{\max}$. We believe this is due to the proximity of $|1\rangle$ states to the boundaries of the lattice. In order to test whether the proximity of $|1\rangle$ states to the boundaries changes the time to reach $\chi_{\max}$ we ran simulations with the defect displaced from the center of the lattice by j sites,

$$|\psi\rangle = |0\rangle^{\otimes\frac{L}{2}-n-j}|1\rangle^{\otimes 2n}|0\rangle^{\otimes\frac{L}{2}-n+j} \ . \tag{5.4}$$

For small values of the displacement we found that the time to reach $\chi_{\max}$ is not modified as shown in Fig. 5.5(b). For larger values of the displacement we found that the time to

reach $\chi_{\max}$ increases rapidly, accounting for the variance of the data in Fig. 5.4. If the sites initialized in the $|1\rangle$ state happen to be near a boundary then simulation time is increased.

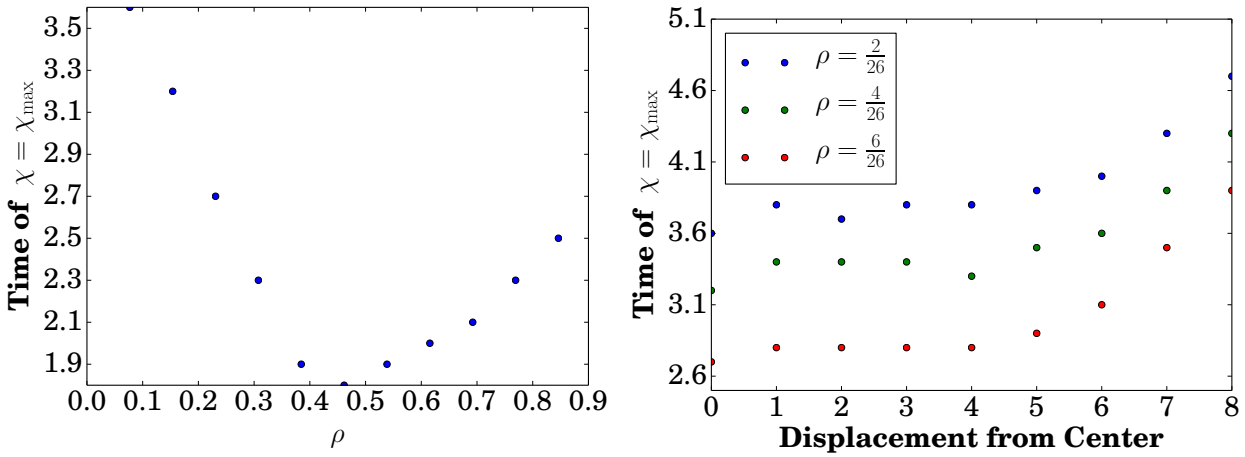

(a) (b)

Fig. 5.5: *χ_{max} saturation time of local defect initial conditions and displaced local defect initial conditions.* A critical filling factor minimizes the time to reach $\chi_{\max}$. Small displacements of local defect initial conditions do not modify the time to reach χ_{max}. Large displacements place $|1\rangle$ states near the boundaries of the lattice and the time to reach χ_{max} increases rapidly.

Because we cannot provide converged estimates of the quantum state after saturation of $\chi_{\max}$ we will conduct the analysis of Chapter 6 using a Trotter-based time evolution scheme written by L. E. Hillberry [45]. This code uses a second order Suzuki-Trotter decomposition to perform time evolution on the exact quantum state, and therefore entanglement does not effect simulation time. The main source of error in this code is due to the non-commutativity of operators in the Suzuki-Trotter decomposition, which approximates the matrix exponential of a sum of operators in terms of a product of exponentials of operators as described in Chapter 2. To establish the accuracy of the Trotter exact code we compare our Trotter-based simulations to simulations performed using exact diagonalization. As noted in Chapter 2 Sec. 2.7, exact diagonalization still contains numerical error due to the finite precision with which the computer represents floating-point numbers. These simulations have $t_f = 0.1$, and $\Delta t = 0.1/2^k$ for $k \in [1, 8]$. We define the error of our Trotter-based simulations for a

time step of Δt as the maximum difference in the 2-norm between the state produced using Trotter-based simulation and exact simulation over the entire simulation time, that is

$$\varepsilon_{\infty,\Delta t} = \max_t || \, |\psi(t)\rangle_{\text{Trotter},\Delta t} - |\psi(t)\rangle_{\text{ED},\Delta t} \, ||_2 \, . \tag{5.5}$$

Two versions of the Trotter-based code were implemented, a symmetric and an asymmetric version. In the symmetric version the decomposition of the matrix exponential results in an error that should be proportional to Δt^2. In the asymmetric version the decomposition of the matrix exponential should result in an error that is proportional to Δt. We confirm the scaling behavior of the error of both the asymmetric and symmetric time evolution schemes in Fig. 5.6. Fitting the error data on a log-log scale we find that the asymmetric

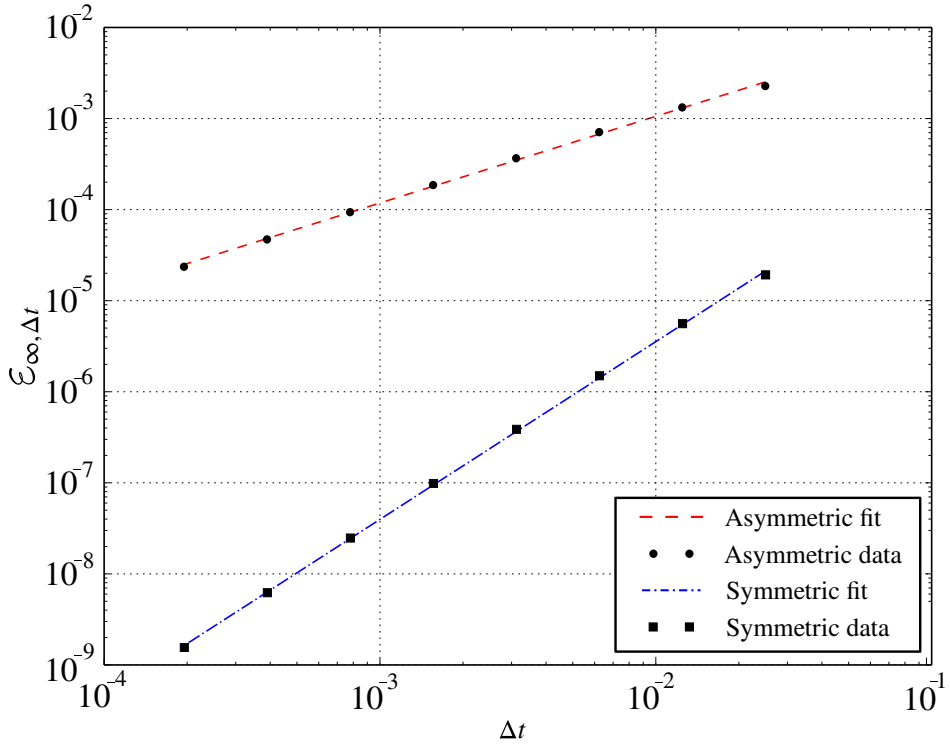

Fig. 5.6: *Error of Trotter time evolution schemes.* The error of our Trotter-based time evolution scheme is proportional to Δt^2 for the symmetric scheme and Δt for the asymmetric scheme. The slope of the asymmetric fit is 0.952 with a sum of squared residuals of 6×10^{-8}. The slope of the symmetric fit is 1.952 with a sum of squared residuals of 4×10^{-12}.

time evolution scheme has $\varepsilon_{\infty,\Delta t} \propto \Delta t^{0.952}$, while the symmetric time evolution scheme has $\varepsilon_{\infty,\Delta t} \propto \Delta t^{1.952}$. Since the symmetric time evolution scheme is more accurate than the

asymmetric time evolution scheme we use the symmetric time evolution scheme throughout the case studies in the sections below and in Chapter 6.

5.2 Blinker Case Study

In [40] an emergent quantum blinker pattern was reported in the dynamics generated by the BCM Hamiltonian simulated on a lattice of 32 qubits with $\chi_{\max} = 30$ and $\Delta t = 0.01$. Such patterns are one of our criteria for complexity. Therefore the ability of the BCM Hamiltonian to generate such an emergent feature suggests that it may support other complex patterns and thus be useful as a complexity generating Hamiltonian. In figure 2 of [40] the initial condition of the quantum blinker pattern is reported as "four alive sites separated by two dead ones". We take this to mean the initial condition $|0\rangle^{\otimes\frac{L-6}{2}} \otimes |110011\rangle \otimes |0\rangle^{\otimes\frac{L-6}{2}}$. In Figure 2 of [40] the resulting dynamics show localized oscillations of $\langle\hat{n}_i\rangle$ over the first 30 units of time evolution, and a blinker pattern in the discretized expectation value $\lfloor\langle\hat{n}_i\rangle+0.5\rfloor$. In figure 3 of [40] this pattern is described as oscillation between $|11011\rangle$ and $|00000\rangle$. In Fig. 5.7 we display the results of our OpenMPS simulations for this initial condition over 100 units of time with $\chi_{\max} = 32$ and $\Delta t = 0.1$. We do not observe localized oscillations

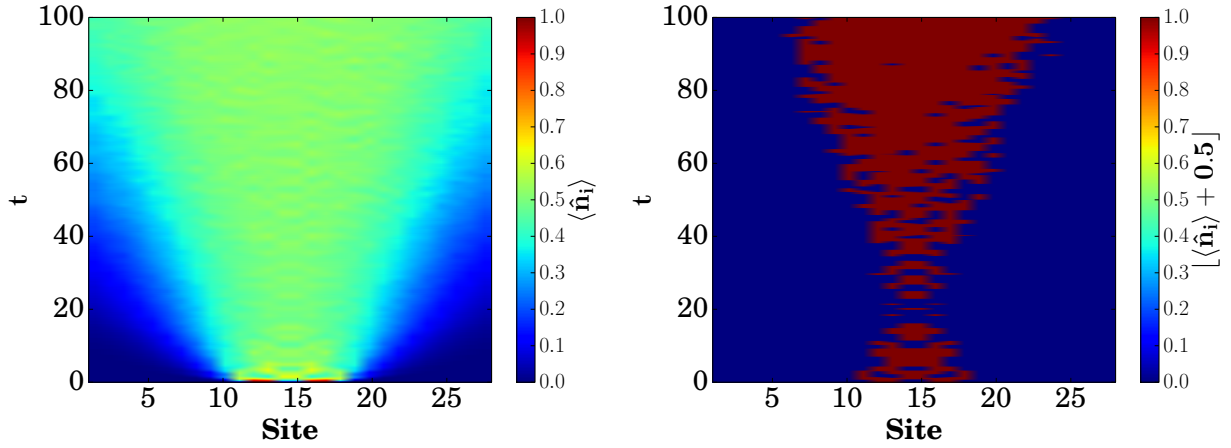

Fig. 5.7: *OpenMPS simulation of BCM blinker initial condition.* We do not observe localized oscillations of $\langle\hat{n}_i\rangle$ or $\lfloor\langle\hat{n}_i\rangle + 0.5\rfloor$.

in $\langle\hat{n}_i\rangle$ or the pattern described in the discretized expectation value. There appears to be

a transient oscillation between $|0110\rangle$ and $|1001\rangle$ for $20 < t < 40$, however this does not correspond to the pattern described in [40]. While the BCM paper uses a smaller time step we note that the pattern they describe in their paper has a period of approximately 10 units of time, so that we should be able to observe the dynamics with $\Delta t = 0.1$. Also note that our simulations of the BCM blinker initial condition are left-right symmetric for $t < 40$, while the data shown in Figure 2 of [40] is clearly not left right symmetric for $t > 10$. Furthermore, we have also confirmed that this pattern does not appear in Trotter-based simulations of 20 qubits.

Although we do not observe a blinker pattern for the initial condition considered in the BCM paper, we have found that the initial condition $|0\rangle^{\otimes\frac{L-3}{2}} \otimes |101\rangle \otimes |0\rangle^{\otimes\frac{L-3}{2}}$ does produce a quantum blinker pattern that is also observed in exact simulations. We refer to this initial condition as the blinker initial condition. Despite the abrupt saturation of $\chi_{\max}$ we have observed that OpenMPS is able to simulate particular observables for the quantum blinker with limited $\chi_{\max}$ as shown in Fig. 5.8 for $L = 20$, $t_f = 100$, and $\Delta t = 0.1$. We

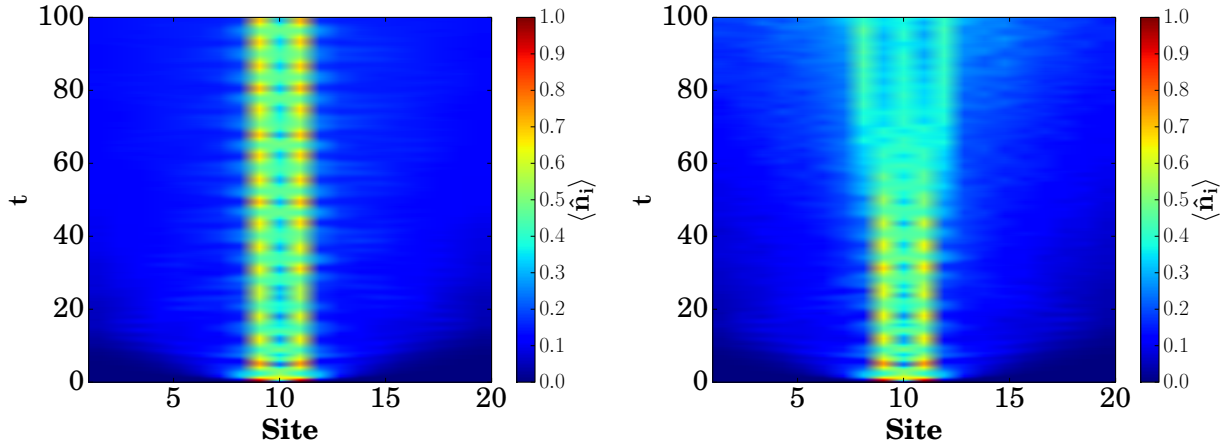

(a) $\chi = 128$ (b) $\chi = 16$

Fig. 5.8: *OpenMPS simulation of a quantum blinker.* OpenMPS is able to simulate the blinker initial condition with $\chi = 128$. Decreasing χ to 16 leads to a damping of oscillations and a delocalization of the blinker pattern. The blinker is therefore not a mean-field object, its dynamics are fundamentally entangled.

performed these simulations for $\chi_{\max} \in \{16, 32, 64, 128\}$. However, we only display results for

$\chi_{\max} \in \{16, 128\}$. We hypothesize that the blinker can be simulated in OpenMPS because it is a small compact object, soliton-like. However, it is not a mean-field type object since it is clearly unstable as we reduce χ. It is a fundamentally entangled robust emergent feature.

In Fig. 5.9 we show the complex network measures and the central bond entropy of OpenMPS simulations of the quantum blinker with $\chi_{\max} \in \{16, 32, 64, 128\}$ and a Trotter-based simulation. In contrast to most initial conditions, the central bond entropy of the

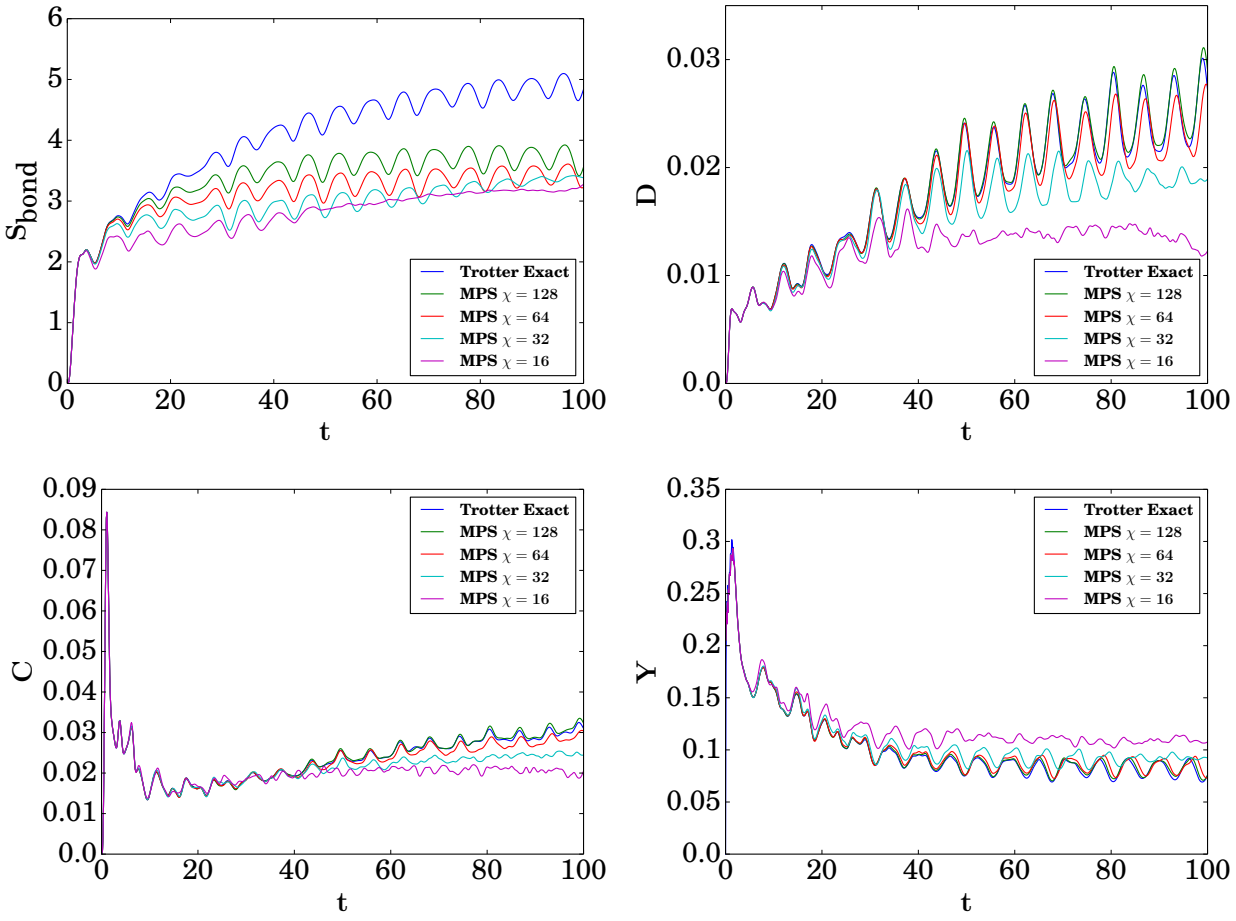

Fig. 5.9: *Complexity and entanglement measures for OpenMPS simulations of blinker.* OpenMPS is able to accurately converge complex network measures to the values computed by a Trotter-based simulation. OpenMPS is also able to reproduce the fluctuations of the central bond entropy despite χ saturating.

blinker increases logarithmically with time in Trotter-based simulations as we will find in Chapter 6. The small value of the central bond entropy of the blinker initial condition

implies the eigenvalues of $\hat{\rho}_{[1:L/2]}$ decay more quickly as a function of eigen index than the eigenvalues of other initial conditions. This is because the entropy measures the uniformity of the eigenvalues of the reduced density matrix. For example, highly entangled states have nearly maximal central bond entropy since the eigenvalues of the reduced density matrix are all approximately equal. The logarithmically slow increase in the central bond entropy observed in Trotter exact simulations of the blinker initial condition thus suggests that it may be possible to simulate this initial condition accurately over longer simulation times than generic initial conditions. In Fig. 5.10 we demonstrate that OpenMPS calculations of $\langle \hat{n}_i \rangle$, C, D, Y, and S_{bond} converge to the values computed using our Trotter-based time evolution scheme as $\chi_{\max}$ is increased. The error in each measure is define as the absolute difference in the measure between OpenMPS and Trotter-based simulations. Since OpenMPS simulations always underestimate the entanglement of the quantum state the error in the central bond entropy does not significantly decrease as $\chi_{\max}$ is increased.

Interestingly the dominant frequencies and scale of fluctuations of the central bond entropy are the same for exact simulations and OpenMPS simulations as shown in Fig. 5.11. To compute $\sigma_{S_{\text{bond}}}$ we first identify the dominant frequency f_0 of the oscillations of the central bond entropy for the blinker initial condition simulated using Trotter exact code. We then define the period of oscillation of the blinker as $T = 1/f_0$. We then compute the standard deviation of the central bond entropy for $t - T < t' < t$ for $t \in [T, t_f]$ for Trotter exact and OpenMPS simulations. This definition differs from the definition of fluctuations in Chapter 6, however both definitions predict persistent fluctuations of the central bond entropy for the blinker initial condition. In Chapter 6 we argue that persistent fluctuations of the central bond entropy and complex network measures far from known/random states are quantifiers of complexity. Therefore, for the blinker initial condition OpenMPS accurately computes the complexity of the quantum many body dynamics, but is not able to accurately compute the entanglement of the quantum many body dynamics.

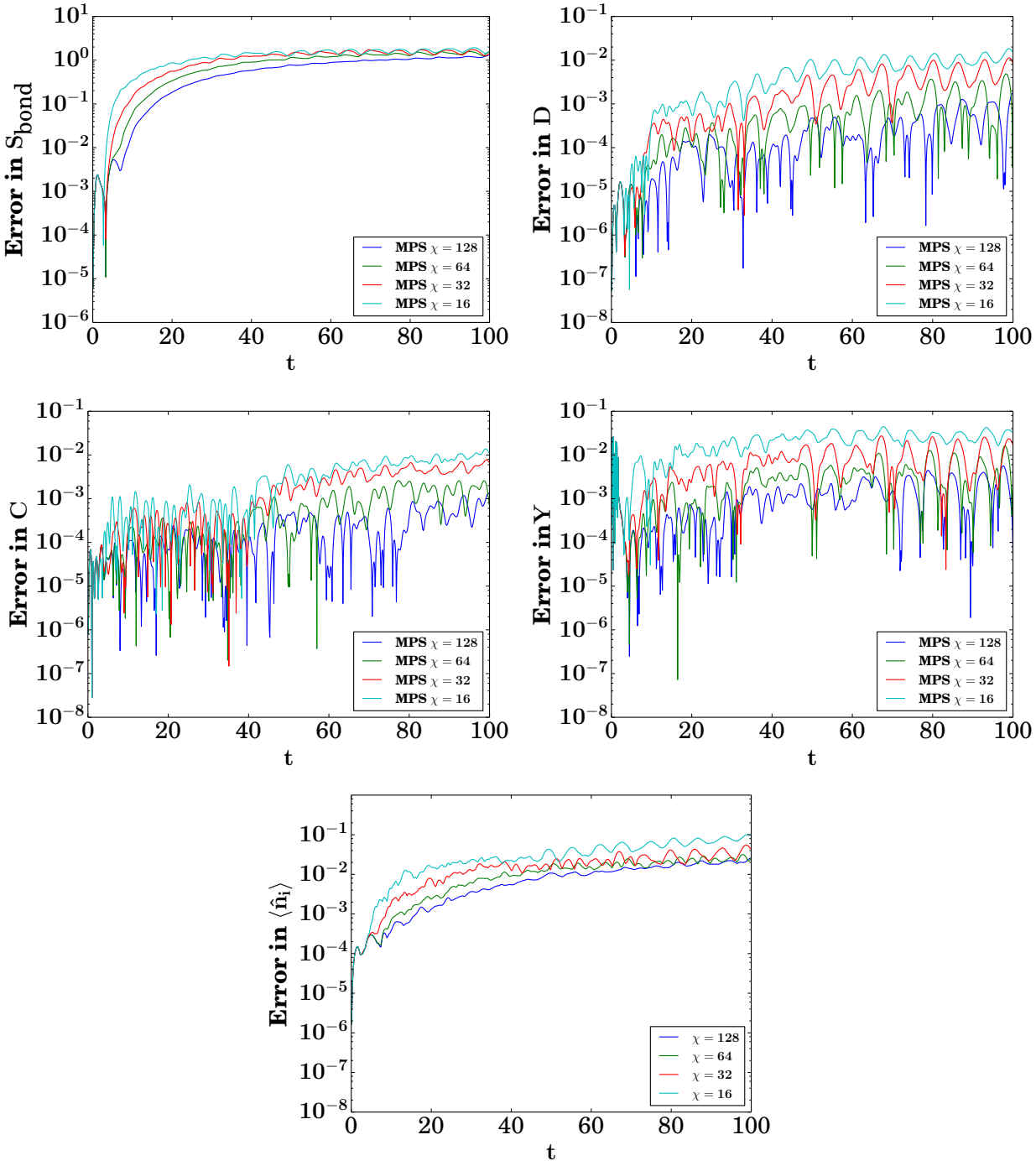

Fig. 5.10: *Error of complexity, entanglement, and local measures for OpenMPS simulations of blinker.* As χ is increased the absolute difference between complexity measures computed by OpenMPS and Trotter-based code is reduced. OpenMPS simulations of the local observable $\langle \hat{n}_i \rangle$ also converge to Trotter-based simulations as $\chi_{\max}$ is increased. The error in $\langle \hat{n}_i \rangle$ is computed by averaging over the absolute error at each site. The error in S_{bond} is not significantly reduced by increased $\chi_{\max}$. Although OpenMPS is able to converge local observables and complex network measures it does not provide reliable estimates of entanglement

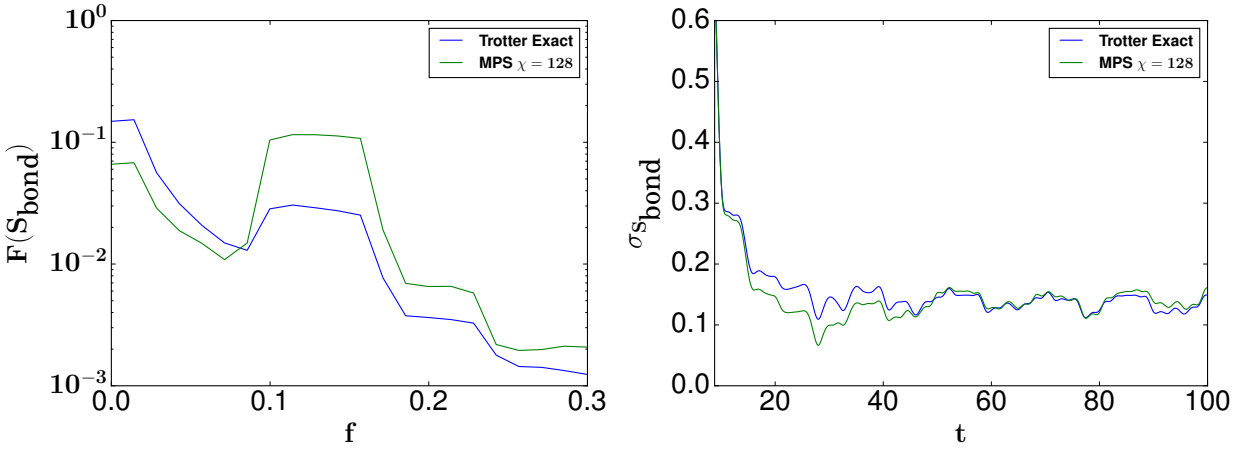

Fig. 5.11: *Power spectrum and fluctuations of blinker initial condition simulated with OpenMPS and Trotter-based code.* The dominant frequencies of the blinker initial condition simulated with OpenMPS and Trotter exact code are the same despite OpenMPS not accurately computing the central bond entropy. OpenMPS is able to compute the complexity of the quantum many body dynamics despite being unable to compute its entanglement.

5.3 Rule 6 Case Study

In Fig. 5.10 we found that OpenMPS can reliably compute measures of complexity for the blinker initial condition. However, it is not able to accurately compute the amount of entanglement generated by the BCM Hamiltonian. An interesting question is therefore, does a quantum game of life Hamiltonian exist for which OpenMPS is able to reliably compute both the entanglement and the complexity generated? We investigate this question by studying the evolution of the blinker initial condition for $L = 20$, $t_f = 100$, and $\Delta t = 0.1$ under another quantum cellular automata Hamiltonian, the rule 6 Hamiltonian. Rule 6 is simpler than the BCM Hamiltonian: the rule 6 Hamiltonian is defined as

$$\hat{H} = \sum_i \left(\hat{b}_i + \hat{b}_i^\dagger\right) \hat{\mathcal{N}}_i^{(1),1} . \tag{5.6}$$

That is, if a site has exactly one neighbor in the alive state, then this site undergoes evolution according to the term $\left(\hat{b}_i + \hat{b}_i^\dagger\right)$, otherwise the site remains static. Although we use the same rule operators in our Hamiltonian version of rule 6, we use the main operator $\hat{b}_i + \hat{b}_i^\dagger$ instead of the $\hat{H}_D \hat{P}(\theta)$ used for unitary-based QCA. In Fig. 5.12 we find that rule 6 produces solitons

that reflect from the boundaries of the lattice several times during the simulation. In Fig. 5.13

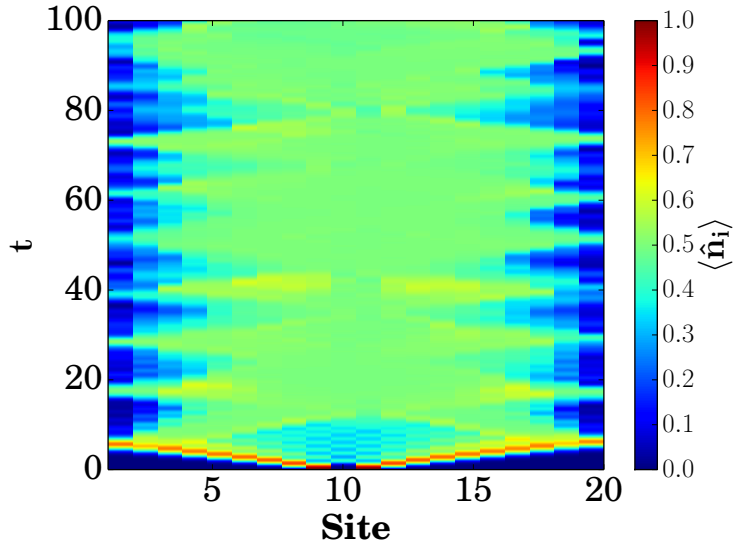

Fig. 5.12: *Spacetime plot of $\langle \hat{n}_i \rangle$ for OpenMPS simulation of rule 6* Rule 6 produces excitations that travel to the boundaries of the lattice and then induce oscillations near the boundaries. The existence of localized traveling solutions suggests the rule 6 Hamiltonian may be a complexity generating Hamiltonian. We hypothesize that only Goldilocks rules are complexity generating.

and Fig. 5.14 we find that OpenMPS is able to reliably compute the central bond entropy and complex network measures of quantum mutual information networks. This suggests that some quantum cellular automata can be simulated with OpenMPS while others can not. However, it would be necessary to perform simulations over many more initial conditions before concluding that the rule 6 Hamiltonian can be simulated with OpenMPS. In this chapter we have studied two forms of convergence of our OpenMPS simulations. We found that OpenMPS is not able to compute converged estimates of quantum states for any of the initial conditions or Hamiltonians studied according to the internal convergence parameters $\chi_{\max}$ and ϵ. However, for particular observables computed on the blinker initial condition we found that OpenMPS is able to reliably converge to the results of our Trotter-based evolution scheme. Finally, there is a third form of convergence that will be left to a future researcher, evaluating the sensitivity of OpenMPS to perturbations in the definition of quantum cellular

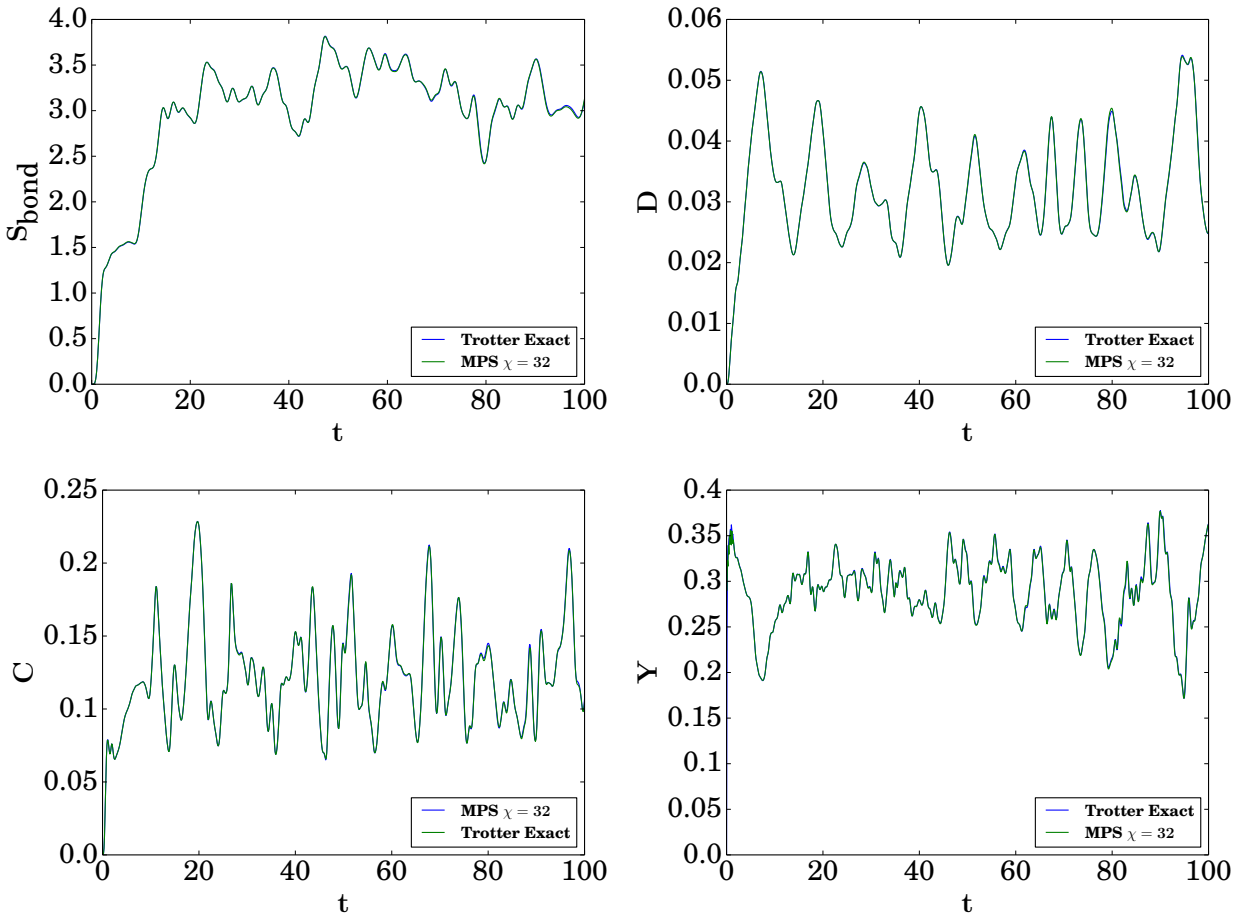

Fig. 5.13: *Entanglement and complexity measures of OpenMPS simulation of rule 6.* OpenMPS is able to accurately compute both the entanglement and complexity of a quantum state evolved under the rule 6 Hamiltonian. That is, OpenMPS accurately computes the central bond entropy and complex network measures of quantum mutual information complex networks when compared to a Trotter-based simulation.

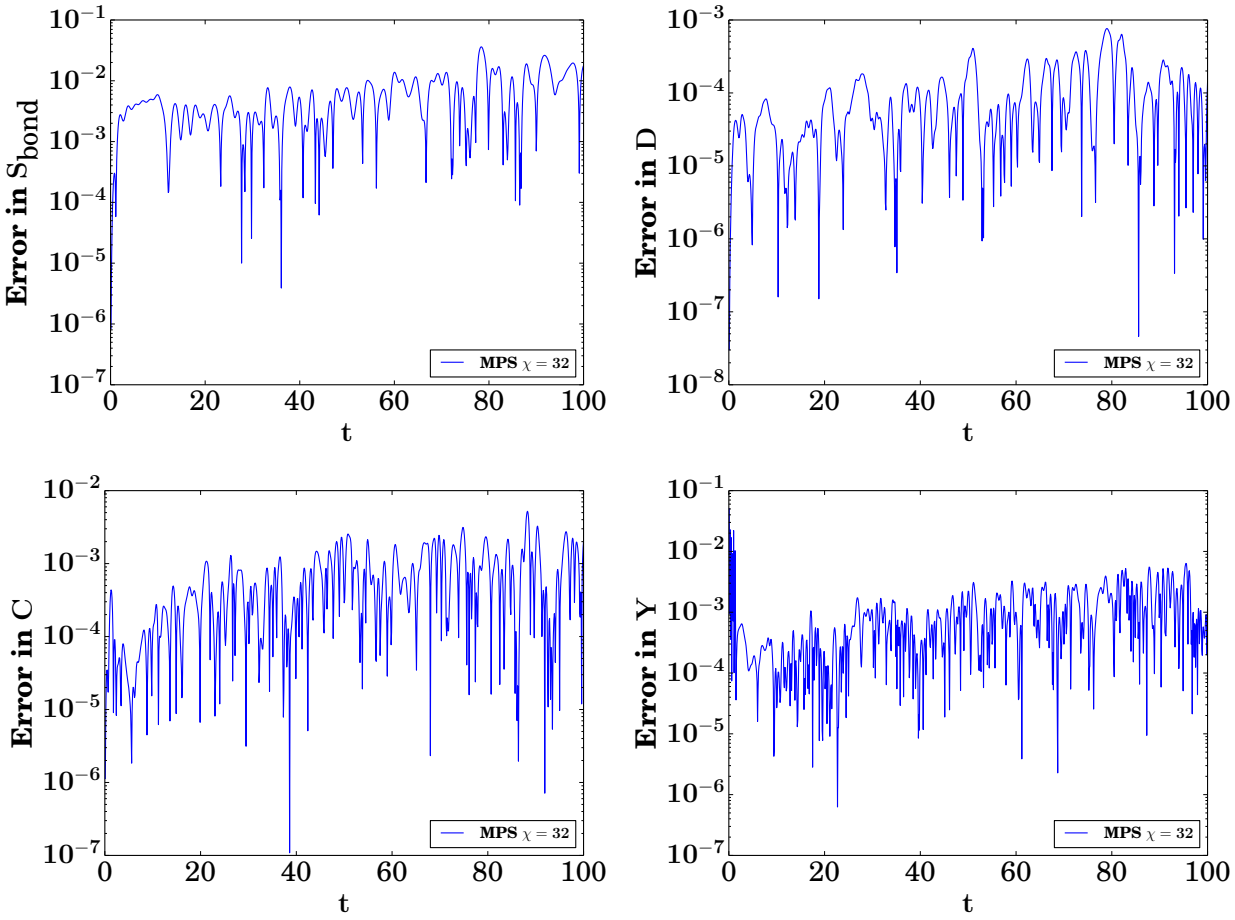

Fig. 5.14: *Error of complexity measures and entanglement measures for OpenMPS simulation of rule 6.* Error in the complex network measures and the central bond entropy for an OpenMPS simulation of an initial condition evolved under the rule 6 Hamiltonian.

automata, for instance multiplying the rule operators by non binary coefficients. In Chapter 6 we will investigate the possibility that some quantum cellular automata can be simulated with OpenMPS by studying the entanglement and complexity generated by 13 quantum cellular automata for 13 initial conditions with Trotter-based time evolution.

CHAPTER 6

COMPLEX DYNAMICS OF QUANTUM CELLULAR AUTOMATA

In this chapter we will study the question "is complexity typically lowly, highly, or both lowly and highly entangled?" and quantify a new physical class of states that are produced by our time evolution schemes displaying high complexity and non-random structure. We also evaluate a set of hypotheses concerning *Goldilocks rules*. Intuitively these are rules that produce activity if there are just the right number of sites in the alive state in the neighborhood of a particular site, not too few, and not too many. For nearest-neighbor unitary-based quantum cellular automata there is only one Goldilocks rule: rule $S = 6$ of [45]. In [45] rule $S = 6$ was found to be the only rule that produced robust and complex dynamics. In our study of next-nearest-neighbor Hamiltonians we focus on quantifying the set of complexity generating rules as quantified by persistent entropy fluctuations with many frequencies, robust dynamical features, and intermediate values of complex network measures applied to quantum mutual information networks. Motivated by the findings of [45] we hypothesize that only Goldilocks rules will be complexity generating. Furthermore, we hypothesize that non-Goldilocks rules tend toward thermalization as quantified by reductions in entropy fluctuations.

We start by introducing our measures of entanglement and complexity. We then study the dynamics of local observables and identify an emergent quantum blinker pattern in the dynamics of $\langle \hat{n}_i \rangle$ for multiple rules. By performing Fourier analysis of network density, clustering coefficient, disparity, and the central bond entropy we quantify the complexity of our dynamics in terms of the number of peaks above a red noise threshold. Next we study the complexity and entanglement generated by our rules at late times by studying late-time averages of the central bond entropy, fluctuations in the central bond entropy, and complex network measures. We conclude with a case study of the long time evolution of a

quantum blinker pattern observed in rule 12. We study how the pattern responds to a linear perturbation and we study the entanglement interactions of two blinker initial conditions.

6.1 Rules, Initial Conditions, and Measures

In this section we define the set of rules and initial conditions that we will study in the rest of the chapter. In this chapter we study next-nearest neighbor ($r = 2$) Hamiltonian-based quantum cellular automata, specifically rules

$$R \in \{2, 3, 4, 6, 7, 10, 12, 14, 15, 17, 21, 23, 28\}$$

where R is defined in Eq. (2.48) and the general form of $\hat{R}_i$ is defined in Eq. (2.47) in Chapter 2. Here we summarize the operators these rules correspond to

$$\hat{R}_i = \hat{\mathcal{N}}_i^{(1)} \Leftrightarrow R = 2\,, \tag{6.1}$$
$$\hat{R}_i = \hat{\mathcal{N}}_i^{(0)} + \hat{\mathcal{N}}_i^{(1)} \Leftrightarrow R = 3\,, \tag{6.2}$$
$$\hat{R}_i = \hat{\mathcal{N}}_i^{(2)} \Leftrightarrow R = 4 \tag{6.3}$$
$$\hat{R}_i = \hat{\mathcal{N}}_i^{(1)} + \hat{\mathcal{N}}_i^{(2)} \Leftrightarrow R = 6\,, \tag{6.4}$$
$$\hat{R}_i = \hat{\mathcal{N}}_i^{(0)} + \hat{\mathcal{N}}_i^{(1)} + \hat{\mathcal{N}}_i^{(2)} \Leftrightarrow R = 7\,, \tag{6.5}$$
$$\hat{R}_i = \hat{\mathcal{N}}_i^{(1)} + \hat{\mathcal{N}}_i^{(3)} \Leftrightarrow R = 10\,, \tag{6.6}$$
$$\hat{R}_i = \hat{\mathcal{N}}_i^{(2)} + \hat{\mathcal{N}}_i^{(3)} \Leftrightarrow R = 12\,, \tag{6.7}$$
$$\hat{R}_i = \hat{\mathcal{N}}_i^{(1)} + \hat{\mathcal{N}}_i^{(2)} + \hat{\mathcal{N}}_i^{(3)} \Leftrightarrow R = 14\,, \tag{6.8}$$
$$\hat{R}_i = \hat{\mathcal{N}}_i^{(0)} + \hat{\mathcal{N}}_i^{(1)} + \hat{\mathcal{N}}_i^{(2)} + \hat{\mathcal{N}}_i^{(3)} \Leftrightarrow R = 15\,, \tag{6.9}$$
$$\hat{R}_i = \hat{\mathcal{N}}_i^{(0)} + \hat{\mathcal{N}}_i^{(4)} \Leftrightarrow R = 17\,, \tag{6.10}$$
$$\hat{R}_i = \hat{\mathcal{N}}_i^{(0)} + \hat{\mathcal{N}}_i^{(2)} + \hat{\mathcal{N}}_i^{(4)} \Leftrightarrow R = 21\,, \tag{6.11}$$
$$\hat{R}_i = \hat{\mathcal{N}}_i^{(0)} + \hat{\mathcal{N}}_i^{(1)} + \hat{\mathcal{N}}_i^{(2)} + \hat{\mathcal{N}}_i^{(4)} \Leftrightarrow R = 23\,, \tag{6.12}$$
$$\hat{R}_i = \hat{\mathcal{N}}_i^{(2)} + \hat{\mathcal{N}}_i^{(3)} + \hat{\mathcal{N}}_i^{(4)} \Leftrightarrow R = 28\,. \tag{6.13}$$

Since the Hamiltonian-based QCA we study in this chapter are all $r = 2$ (next-nearest-neighbor) we write $\hat{\mathcal{N}}_i^{(j)}$ instead of $\mathcal{N}_i^{(j),2}$ as written in Eq. (2.47) in Chapter 2. A Goldilocks rule is defined as a rule which produces activity if the number of sites in the state $|1\rangle$ is

within an interval not including the maximum possible number of living sites, $2r$, or the least possible number of living sites, 0. Thus, of the rules we study, rules 2, 4, 6, 12, and 14 are Goldilocks rules, while rules 3, 7, 10, 15, 17, 21, 23, and 28 are non-Goldilocks rules. In Fig. 6.1 we provide sketches of the rule operators defined in Eqs. (6.1)-(6.13) to illustrate the difference between Goldilocks and non-Goldilocks rules.

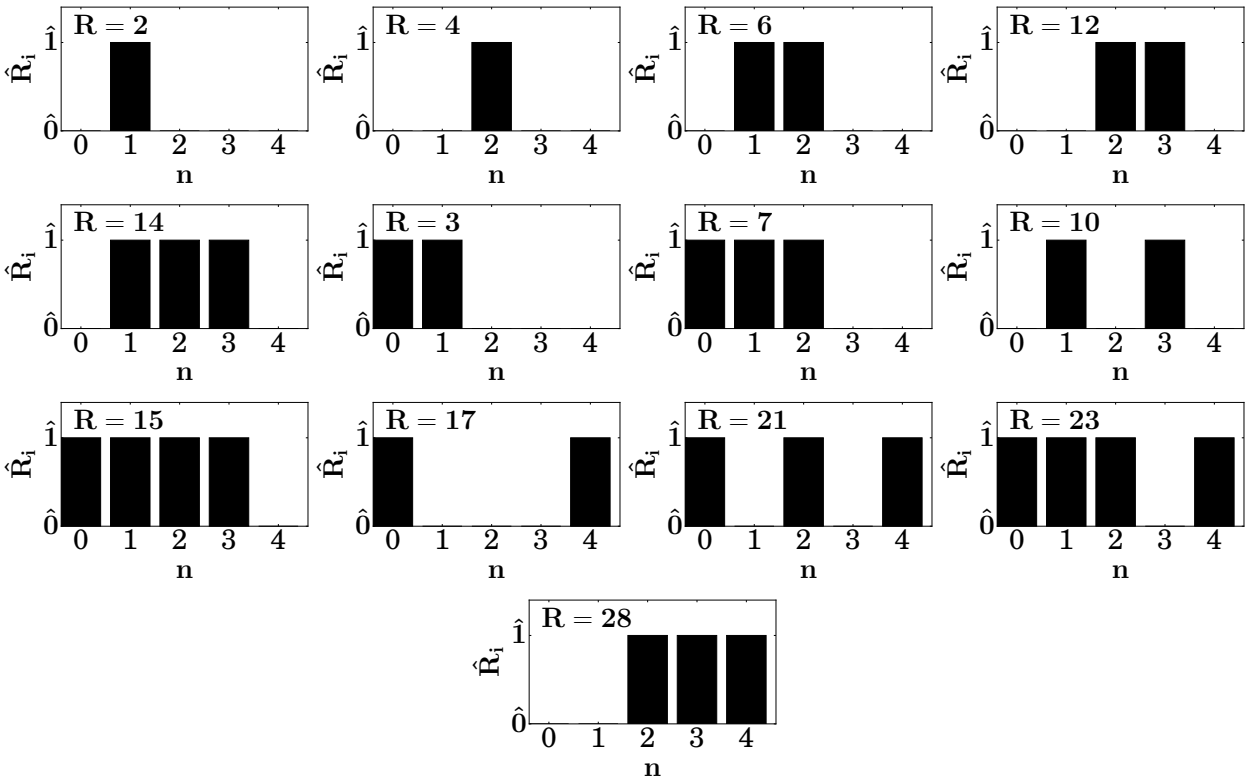

Fig. 6.1: *Sketch of Goldilocks and Non-Goldilocks Rules.* Goldilocks rules are rules that produce activity if there are just the right number of neighbors in the alive state, $|1\rangle$, not too few and not too many. A horizontal line at $\hat{1}$ from n to $n+1$ indicates that a rule produces activity if there are exactly n neighbors in the alive state, $|1\rangle$. A horizontal line at $\hat{0}$ from n to $n+1$ indicates that a rule does not produce activity if there are exactly n neighbors in the alive state, $|1\rangle$. Rules 2, 4, 6, 12, and 14 are Goldilocks rules. Rules 3, 7, 10, 15, 17, 21, 23, and 28 are non-Goldilocks rules.

For most of this chapter we study the properties of next-nearest-neighbor Hamiltonian-based QCA. However, in Sec. 6.5 we perform a follow up study of the nearest-neighbor unitary-based QCA defined in [45] for rules $S \in \{1, 2, 6, 9, 10, 14\}$. The rule number, S, for these nearest-neighbor unitary-based quantum cellular automata is defined in Eq. (2.53) in

Chapter 2. While [45] studied bond entropy fluctuations for nearest-neighbor unitary-based QCA, we study the scaling of the central bond entropy as a function of system size.

For our study of next-nearest-neighbor Hamiltonian-based QCA and our study of nearest-neighbor unitary-based QCA we perform simulations for the following initial conditions:

$$|B\rangle = |0...101...0\rangle \ , \tag{6.14}$$
$$|D_2\rangle = |0...0110...0\rangle \ , \tag{6.15}$$
$$|D_3\rangle = |0...01110...0\rangle \ , \tag{6.16}$$
$$|T_1\rangle = |0...0110110...0\rangle \ , \tag{6.17}$$
$$|T_2\rangle = |0...01100110...0\rangle \ , \tag{6.18}$$
$$|T_3\rangle = |0...011000110...0\rangle \ , \tag{6.19}$$
$$|T_4\rangle = |0...0110000110...0\rangle \ , \tag{6.20}$$
$$|\phi_+\rangle = |0\rangle^{\otimes L/2-1} \otimes \frac{1}{\sqrt{2}} \left(|00\rangle + |11\rangle\right) \otimes |0\rangle^{\otimes L/2-1} \ , \tag{6.21}$$
$$|\phi_-\rangle = |0\rangle^{\otimes L/2-1} \otimes \frac{1}{\sqrt{2}} \left(|00\rangle - |11\rangle\right) \otimes |0\rangle^{\otimes L/2-1} \ , \tag{6.22}$$
$$|S\rangle = \frac{1}{\sqrt{2^{L/2}}} \left(|01\rangle - |10\rangle\right)^{\otimes L/2} \ , \tag{6.23}$$
$$|r_3\rangle \ , \tag{6.24}$$
$$|R_3\rangle \ , \tag{6.25}$$
$$|C\rangle \ . \tag{6.26}$$

The state $|B\rangle$ is the blinker initial condition, $|D_i\rangle$ is a local defect initial condition with i states in the alive state $|1\rangle$, $|T_i\rangle$ is the two defect initial condition with defects separated by i sites, $|\phi_\pm\rangle$ are Bell states, $|S\rangle$ is an array of spin singlets, $|r_i\rangle$ is a random quantum state with normally distributed complex coefficients and random seed i, $|R_i\rangle$ is a random Fock state with probability of placing $|1\rangle$ at any site of $p = 0.5$ and random seed i, and $|C\rangle$ is a cluster state with links between nearest neighbors on the lattice [69]. Although initial condition $|S\rangle$ is an eigenstate of rule 17 we have decided to include it in our study as it is one of the only initial conditions with non-trivial entanglement structure, and it is not a stationary state of any other rule we consider.

We quantify the amount of entanglement in simulations by the central bond entropy S_{bond} defined in Eq. (2.17) of Chapter 2. This quantity is similar to the χ parameter of Chapter 5, for highly entangled simulations $S_{\text{bond}} \approx \log_2(\chi)$. In Sec. 6.7 we study S_{bond} normalized to its maximum value of $S_{\text{max}} = L/2$. We quantify the complexity of our simulations by persistent fluctuations of the central bond entropy as well as complex network measures far from their values for random/well known states. Fluctuations of the central bond entropy are defined as the difference in the central bond entropy between times t and $t - n\Delta t$

$$\Delta S(t)_n = S_{\text{bond}}(t) - S_{\text{bond}}(t - n\Delta t)\,. \tag{6.27}$$

In Sec. 6.2 we study $|\Delta S_1|$ averaged over groups of $\tau = 20$ time steps. We have also considered averages with $\tau = 5, 10$ however we find the same trends as for $\tau = 20$. Analyses of $|\Delta S_n|$ for $n \in [2, 5]$ make similar predictions for the complexity of dynamics as $|\Delta S_1|$ in Sec. 6.4. Therefore we refer to ΔS_1 as ΔS in this chapter. All simulations have a time step of $\Delta t = 0.1$ and final time of $t_f = 100$ except for the long time simulation of the quantum blinker, which has $t_f = 1000$. We have assured the convergence of late-time averages in the time step Δt by comparing to simulations with $\Delta t = 0.1/2^3$ as described in Sec. 6.4. All measures are computed at each time step. In Sec. 6.4 we compute late-time averages of all quantities, and denote the average by a bar over the measure. Late-time averages of a measure are computed by averaging over the last N_{lt} values of that measure for a simulation in order to discard transients. We have set $N_{\text{lt}} = 100$ throughout our study, however we have also assured the convergence of our results in N_{lt} by comparing to analyses with $N_{\text{lt}} = 500$ as described in Sec. 6.4. We study lattices of lengths $L \in \{10, 12, 14, 16, 18, 20\}$.

6.2 Dynamics of Local Observables and Entanglement

In Fig. 6.2 and Fig. 6.3 we provide spacetime plots of the expectation value of the number operator, $\langle \hat{n}_i \rangle$, and the single site von Neumann entropy S_i. In each plot we show the dynamics of initial condition $|B\rangle$ evolved under rules 2, 3, 4, 12, 17, and 23. In these spacetime plots the vertical axis is time t and the horizontal axis is site i of our lattice. We

do not observe robust dynamical features in $\langle \hat{\sigma}_i^y \rangle = i \langle \hat{b}_i - \hat{b}_i^\dagger \rangle$ or $\langle \hat{\sigma}_i^x \rangle = \langle \hat{b}_i + \hat{b}_i^\dagger \rangle$ that are not already present in the dynamics of $\langle \hat{n}_i \rangle$. Although, interestingly only the cluster state initial condition produces dynamics in $\langle \hat{\sigma}_i^x \rangle$ for our Hamiltonians. The dynamics of local observables can identify localized solutions like the quantum blinker patterns shown in Fig. 6.2(c), (d), and (f). These quantum blinker patterns are examples of the robust dynamical features we expect to find in complexity generating rules. Such localized solutions often correspond to simulations that are less highly entangled than simulations without localized solutions. While the blinker structures of rules 12 and 28 are well localized and have a well defined period, the oscillations of rule 4 appear to have additional frequencies. Rule 2 thermalizes to a state with a Gaussian profile in $\langle \hat{n}_i \rangle$, while rule 3 thermalizes to a state with constant $\langle \hat{n}_i \rangle$ throughout the lattice except near the boundaries. Rule 17 produces independently oscillating patterns along the boundaries of the lattice, separated by 7 non-evolving sites. In Fig. 6.3(c) we find that the rule 4 blinker has highly dynamic entanglement of the von Neumann entropy. This contrasts with the blinkers of rules 12 and 28 which have entanglement that slowly diffuses to the boundaries of the lattice. The boundaries of the diffusing entanglement can also be observed in the spacetime plots of $\langle \hat{n}_i \rangle$ suggesting that the local observable $\langle \hat{n}_i \rangle$ correlates with S_i. We also find that the von Neumann entropy of rule 2 equilibrates to a similar pattern as $\langle \hat{n}_i \rangle$, with entanglement in the center of the lattice and less entanglement at the boundaries. Similarly, S_i of rule 3 is lower where $\langle \hat{n}_i \rangle$ equilibrates to lower values, and higher where it equilibrates to higher values. This relationship between a local observable and an entanglement measure is reminiscent of the relation between number fluctuations and von Neumann entropy derived in [86]. The spacetime plot of rule 17 shows that the non-dynamical sites have no entanglement with other sites, implying that rule 17 produces spatially factorized dynamics.

We have identified different behaviors of the late-time central bond entropy as a function of system size, initial condition, and rule number. For some simulations the central bond entropy approaches a constant value near $L/2$ as L is increased. These simulations have

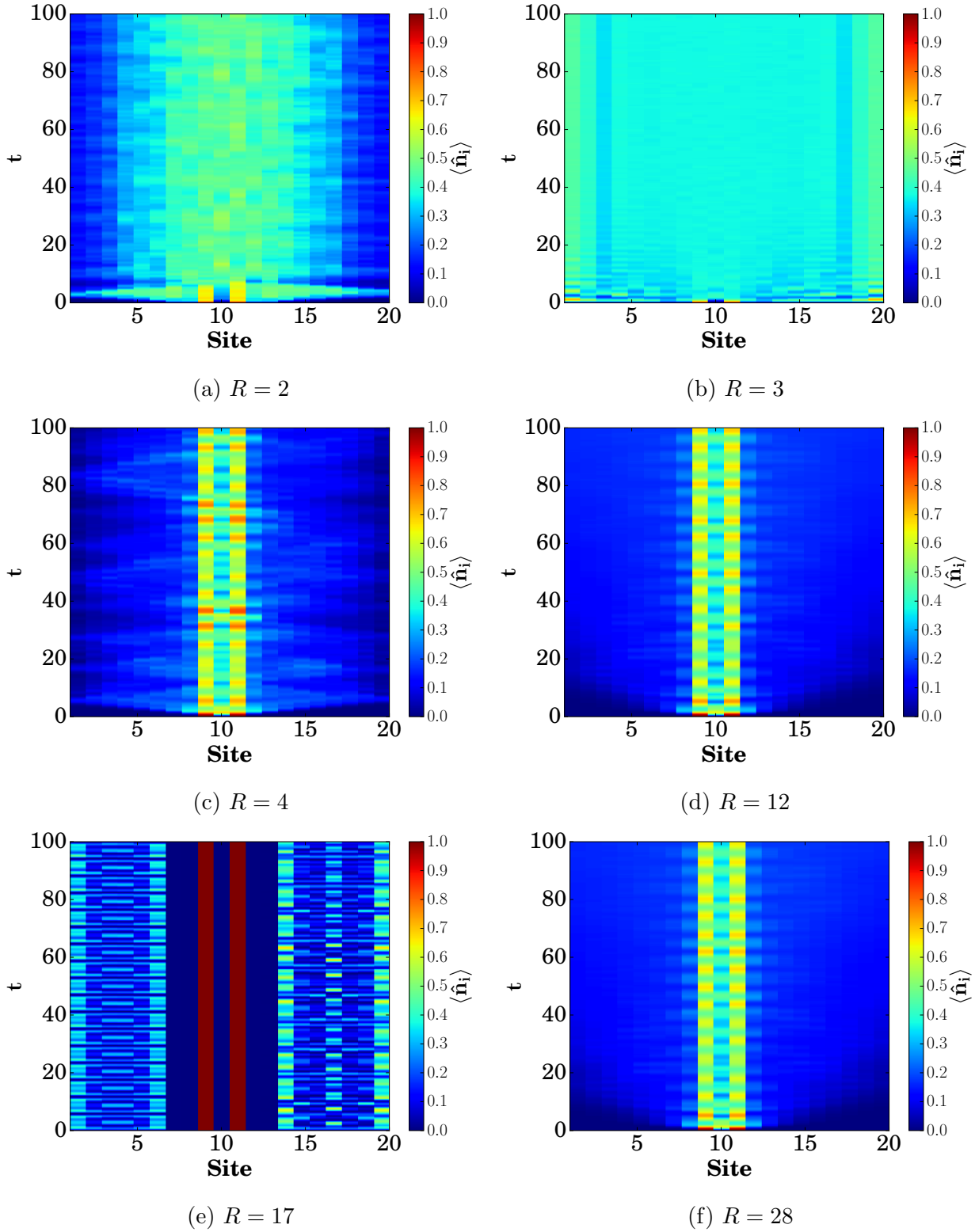

(a) $R = 2$

(b) $R = 3$

(c) $R = 4$

(d) $R = 12$

(e) $R = 17$

(f) $R = 28$

Fig. 6.2: *Spacetime plots of* $\langle \hat{n}_i \rangle$ *for quantum cellular automata evolution of initial condition* $|B\rangle$. Rules 4, 12, and 28 have blinker-like patterns. Rule 2 thermalizes to a state with a Gaussian profile in $\langle \hat{n}_i \rangle$. Rule 3 thermalizes to constant $\langle \hat{n}_i \rangle$ throughout the lattice except for sites near the boundaries. Rule 17 produces two independent oscillating patterns.

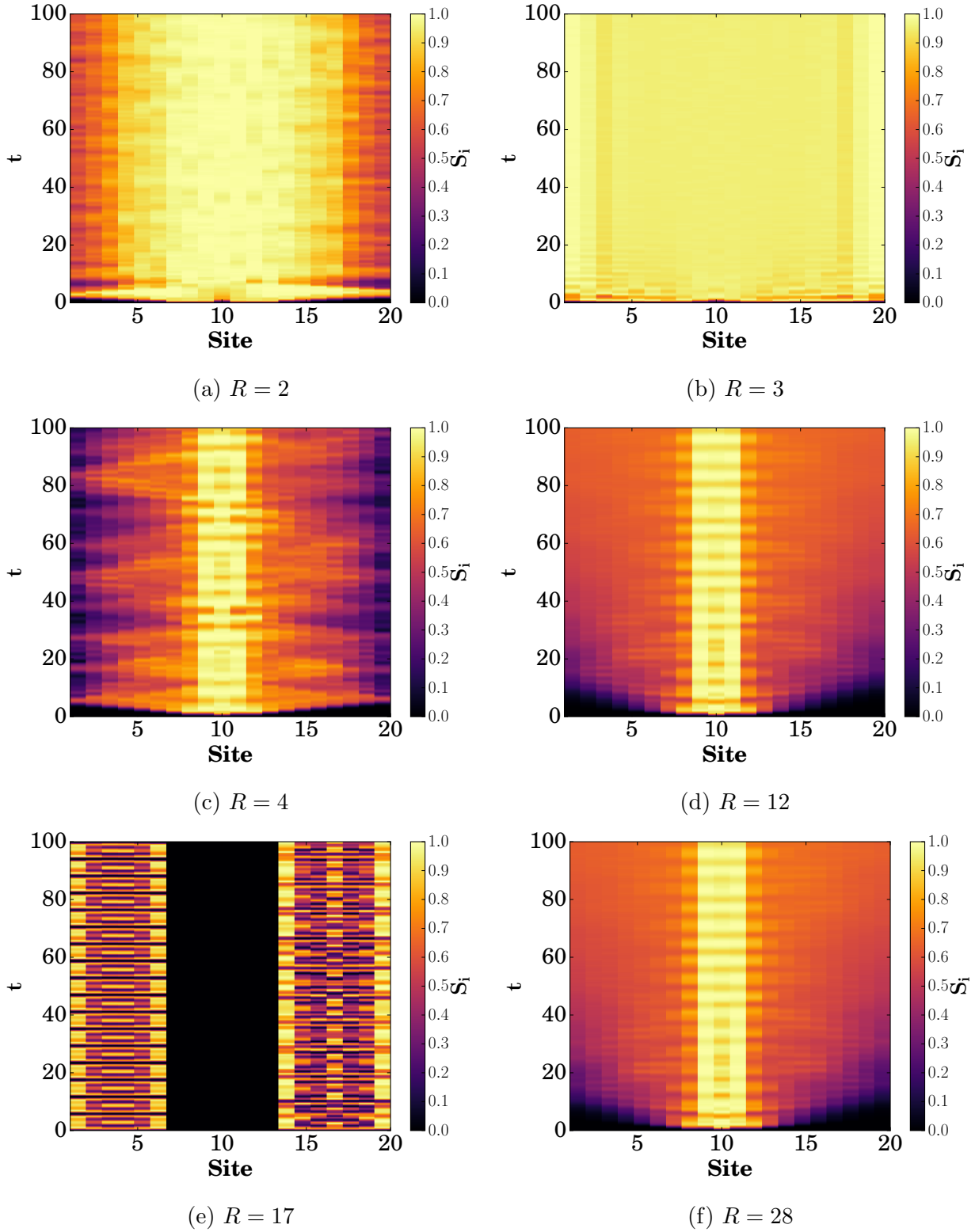

(a) $R = 2$

(b) $R = 3$

(c) $R = 4$

(d) $R = 12$

(e) $R = 17$

(f) $R = 28$

Fig. 6.3: *Spacetime plots of S_i for quantum cellular automata evolution of initial condition $|B\rangle$.* Entanglement propagates at different rates for the blinker structures of rules 4, 12, and 28. Rule 17 produces spatially factorized dynamics. Plots are asymmetric due to the lattice having an even number of sites.

small fluctuations of the central bond entropy as shown for rules 3 and 15 in Fig. 6.4. In other simulations the central bond entropy approaches a constant value less than $L/2$ with larger fluctuations in the central bond entropy as shown for rules 2, 12, and 28 in Fig. 6.4. The quantum blinker patterns of rules 12 and 28 have bond entropy that grows very slowly. However, the average value of the central bond entropy keeps increasing for the entire simulation as shown in Fig. 6.4. Finally, rule 4 produces dynamics whose average value does not increase as a function of L for certain initial conditions. These simulations have large fluctuations of the central bond entropy. We show an example in Fig. 6.4. Rule 17 often produces dynamics that spatially factorize and have zero central bond entropy. However for initial condition $|C\rangle$ we have found that rule 17 generates dynamics that appear to obey an area law. That is, $\overline{S}_{\text{bond}}$ is independent of system size and we do not observe localized solutions in local observables like $\langle \hat{n}_i \rangle$ for initial condition $|C\rangle$ evolved under the rule 17 Hamiltonian.

In Fig. 6.5 we present the results of computing $|\Delta S(t)|$ averaged over $\tau = 20$ time steps for all initial conditions in Eqs. (6.14)-(6.26), all rules in Eqs. (6.1)-(6.13), and $L \in \{10, 20\}$. For $L = 10$ it is difficult to differentiate rules that have persistent fluctuations of the central bond entropy, however for $L = 20$ there are clear differences. The set of initial conditions with average $|\Delta S| \approx 10^{-4}$ for the entire simulation correspond to the random initial condition $|r_3\rangle$. Certain rules have fluctuations that approach levels consistent with this random initial condition, while other rules have fluctuations well above values consistent with the random initial condition. While Fig. 6.5 displays the fluctuations of the central bond entropy for all rules we also provided plots for rules 4 and 7 alone in Fig. 6.6(a) and (b) respectively. Unlike the Goldilocks rule 4, the non-Goldilocks rule 7 has significantly reduced fluctuations of the central bond entropy for all initial conditions. Most rule 7 simulations approach levels consistent with the random initial condition, $|r_3\rangle$. We say that rules with fluctuations above levels consistent with the random initial condition have persistent fluctuations of the central bond entropy. In Sec. 6.4 we quantify this notion more precisely.

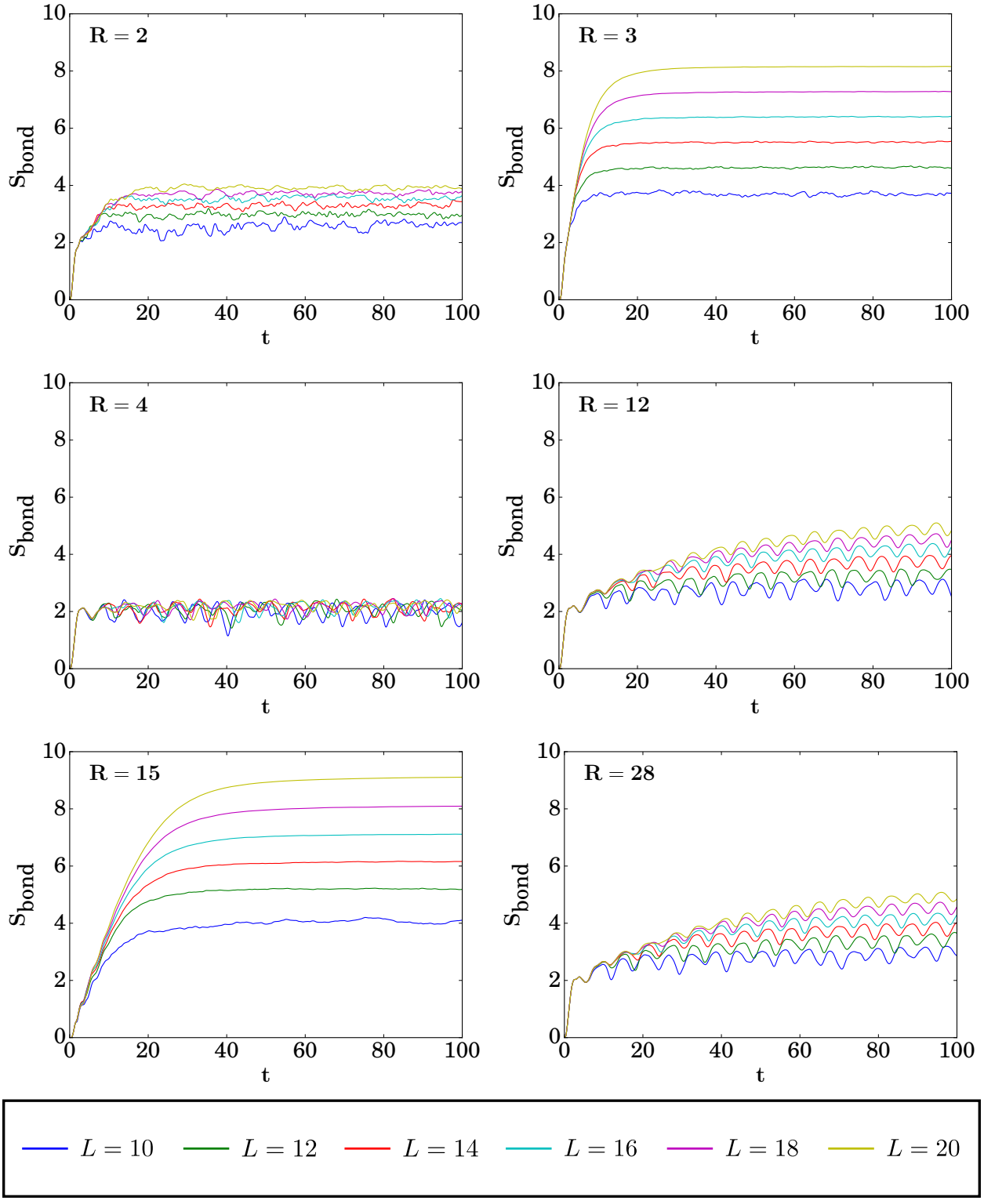

Fig. 6.4: *Bond entropy time series for quantum cellular automata evolution of initial condition* $|B\rangle$. For many rules S_{bond} increases nearly linearly before approaching a constant value dependent on L. Rules producing a blinker-like pattern in $\langle \hat{n}_i \rangle$ have oscillations in S_{bond}. Rule 4 produces dynamics of S_{bond} that fluctuate at a constant independent of L.

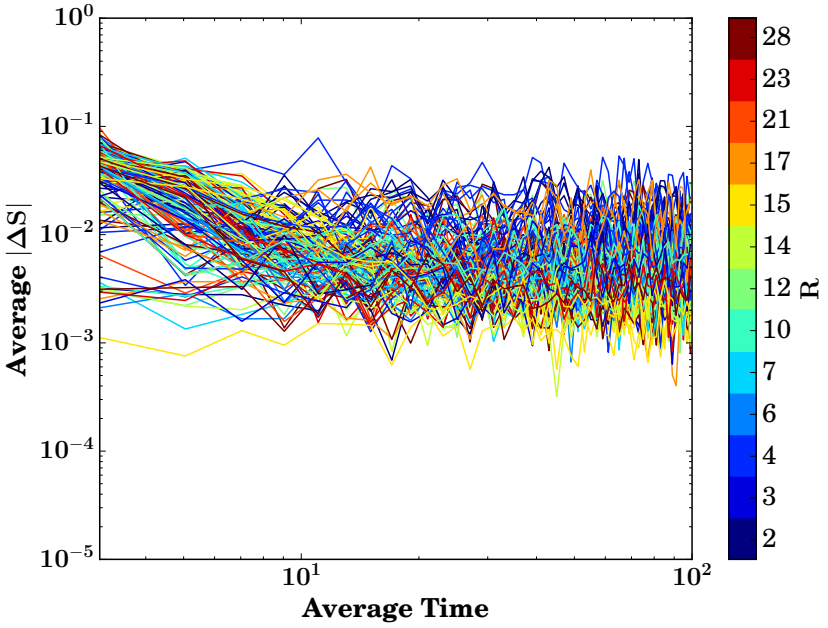

(a) $L = 10$

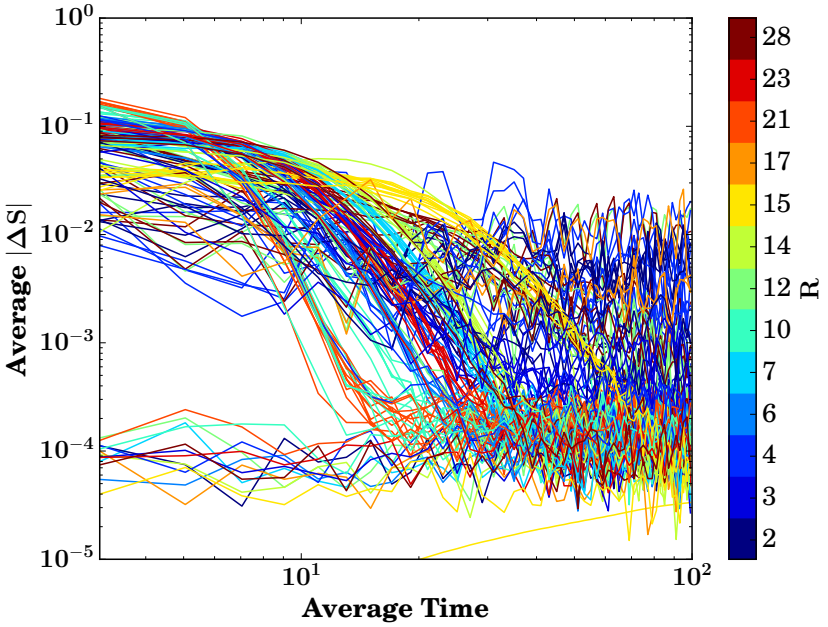

(b) $L = 20$

Fig. 6.5: *Fluctuations of the central bond entropy for quantum cellular automata for all initial conditions and all rules.* Lines are color coded by rule. The simulations with initial fluctuations of the central bond entropy at $\approx 10^{-4}$ are simulations with a random initial condition $|r_3\rangle$. Many rules have a drastic reduction in fluctuations of the central bond entropy as fluctuations approach levels consistent with a random initial condition. Other rules maintain fluctuations of the central bond entropy for the entire simulation.

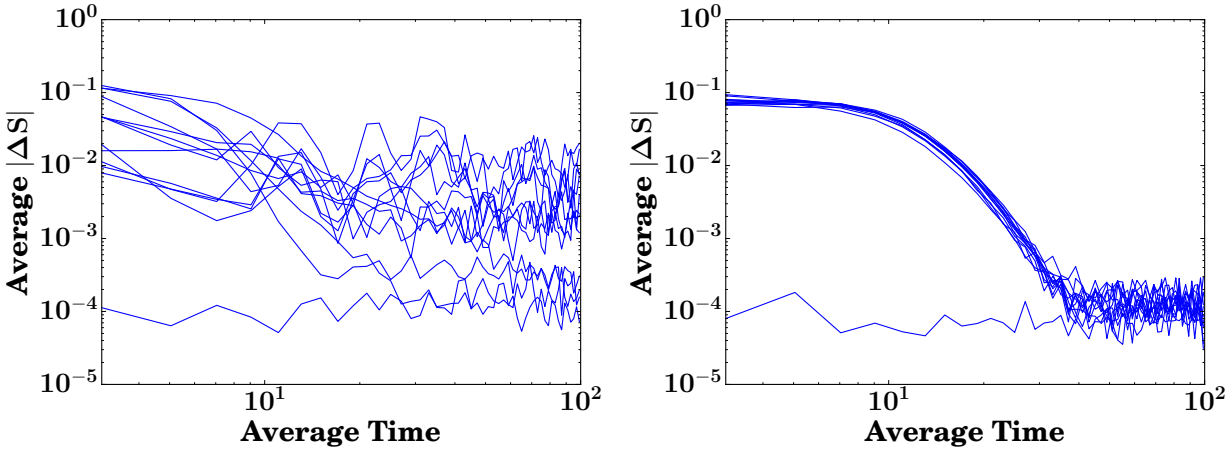

(a) $R = 4$ (b) $R = 7$

Fig. 6.6: *Fluctuations of the central bond entropy for rules 4 and 7 for all initial conditions.* The Goldilocks rule 4 maintains fluctuations at the level of 10^{-3} over the entire simulation for most initial conditions. In contrast, the non-Goldilocks rule 7 has significantly reduced fluctuations of the central bond entropy, thermalizing towards a state consistent with the random initial condition $|r_3\rangle$.

6.3 Fourier Analysis

In his Master's thesis L. Hillberry introduced frequency analysis of complex network measures to characterize entanglement dynamics [45]. He identified significant peaks by computing a 95% confidence red noise spectrum and finding peaks in the power spectra of complex network measures that are above this red noise spectrum [45]. Qualitatively, red noise is noise that has a power spectrum that decreases as frequency is increased. In contrast to white noise, which is uncorrelated in time, red noise is correlated in time. Such power spectra are often observed in time series of complex systems, for example precipitation totals from Earth's atmosphere and solar flares from the Sun [87, 88]. Red noise can be generated from white noise from the first order linear Markov process $x(t) = rx(t - \Delta t) + y(t)$ where $y(t)$ is a white noise term added to the signal at each time step [87]. This is essentially a random walk parameterized by the redness parameter r. If $r = 0$ the signal at time t does not depend on the signal at time $t - \Delta t$ and the signal is white noise. As r is increased the signal at time t does depend on the signal at time $t - \Delta t$ and so the signal will be correlated

in time. The power spectrum of this model of red noise is [87]

$$F_r = \frac{1 - r^2}{1 - 2r\cos(2\pi f \Delta t) + r^2}\,. \tag{6.28}$$

The autocorrelation coefficient between times t and $t - \Delta t$ is equal to the red noise parameter for this model of red noise [87]. Therefore, under the null hypothesis that the time series of our measures are due to such a red noise process we compute the autocorrelation coefficient between times t and $t - \Delta t$ for each time series to estimate its redness parameter. We then construct a normalized red noise spectrum $F_r/|F_r|$ to compare to the normalized power spectrum of the time series $F/|F|$. The norm of a power spectrum is defined as the sum of the power spectrum over all frequencies. Next we multiply the F_r derived for each time series by $\chi^2 = 5.991$ for the χ^2_2 distribution with $p = 0.05$. This sets a 95% confidence level that peaks found above the red noise spectrum are not due to random fluctuations. The peaks of our spectra that are above their 95% confidence level red noise threshold we deem significant. Our criterion for a significant peak in the power spectra of a measure is that it have a greater amplitude than the power spectrum of its corresponding red noise signal. From analyses of power spectra for different system sizes we have found that the power spectra for smaller system sizes tend to be less smooth. The power spectra for larger system sizes typically have the same set of important frequencies as smaller system sizes, however some peaks disappear as the system size is increased. We interpret such disappearing peaks to represent finite-size effects and therefore to be less universal than persistent peaks. Scaling studies up from $L = 10$ reveal that the number of significant peaks decreases as system size is increased for all rules. In Fig. 6.7 we provide an example of our red noise analysis for rules 14 and 21. Rule 14 has hardly any significant peaks for any measure while rule 21 has many significant peaks. The peaks of rule 21 above the 95% confidence level red noise threshold shown in Fig. 6.7(b) indicate that its dynamics are not consistent with the red noise null hypothesis.

In our summary plots of the significant frequencies of our rules we only include peaks for $L = 20$, as much of the data for $L < 20$ is redundant and exhibits finite size effects.

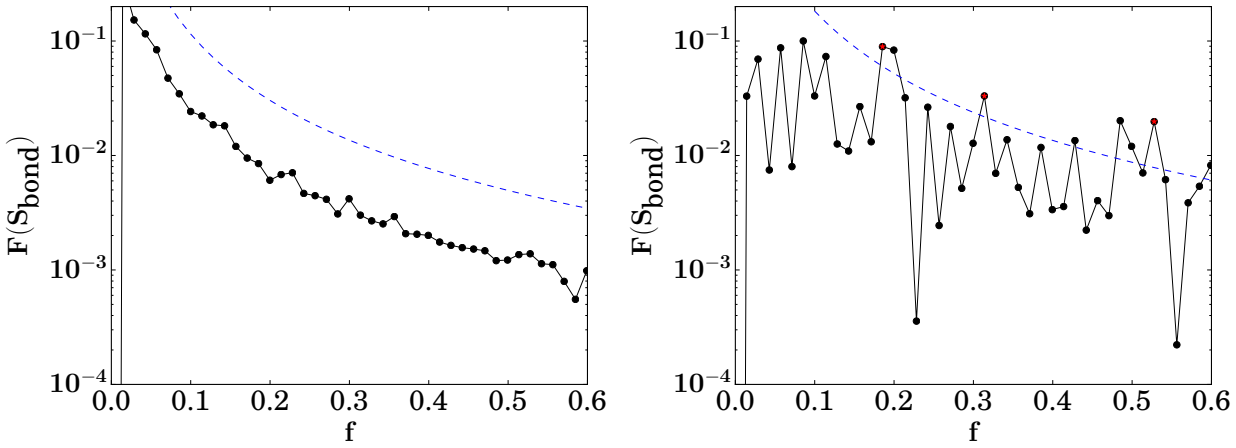

(a) $R = 14$ (b) $R = 21$

Fig. 6.7: *Power spectra of the central bond entropy for evolution of initial condition* $|B\rangle$ *evolved under rules 14 and 21 on a lattice of 20 qubits.* 95% confidence level red noise threshold is indicated by a blue dashed line. The power spectra of the central bond entropy are indicated by black circles. Lines are a guide to the eye. The peaks of rule 21 above this threshold indicate its dynamics are not consistent with red noise. In contrast rule 14 has no peaks above the red noise threshold indicating that its dynamics may be consistent with red noise.

Many peaks are common amongst our various complex network measures. In Fig. 6.8(a) we plot the frequency of significant peaks of the central bond entropy, complex network measures, and the local observable $\langle \hat{n}_{L/2-1} \rangle$ for all initial conditions. In Fig. 6.8(a) we find that clustering and density often have peaks at the same frequencies suggesting they identify similar processes in the dynamics of our networks. Disparity also has similar frequencies for many of its important peaks, however disparity also has many peaks at higher frequencies than either clustering or density for many rules. In Fig. 6.8(b) we find that rules 10, 17, and 21 have many significant peaks for all measures. We remind the reader that all rules are depicted in Fig. 6.1. Rules 2, 3, 4, 6, and 23 also have many significant peaks in the power spectra of complex network measures. Finally, rules 2, 4, 6, 10, 17, and 21 produce more significant peaks in the power spectra of S_{bond} than all other rules. Despite the abrupt thermalization of rule 21 observed in Fig. 6.5, this rule produces more significant peaks in the power spectrum of the central bond entropy than all other rules. That is, despite the

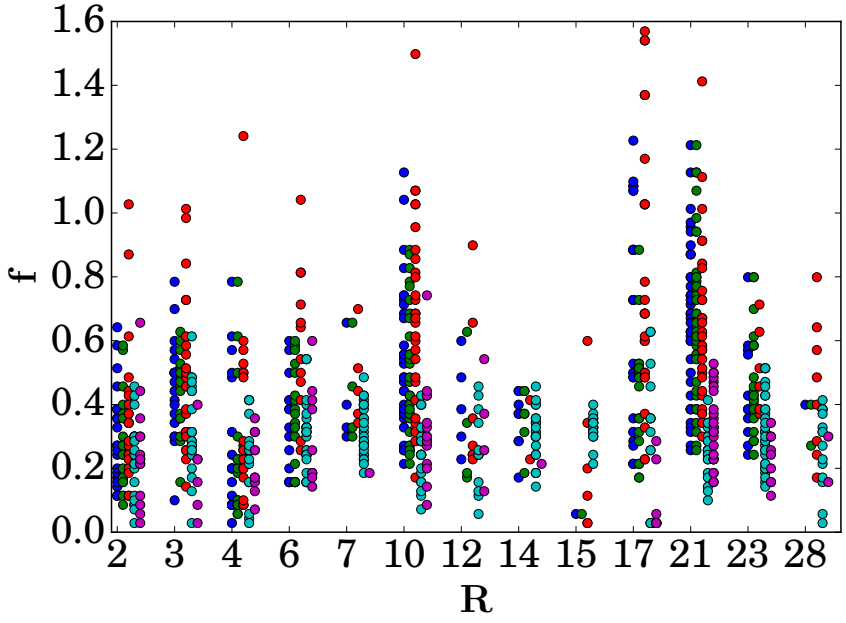

(a)

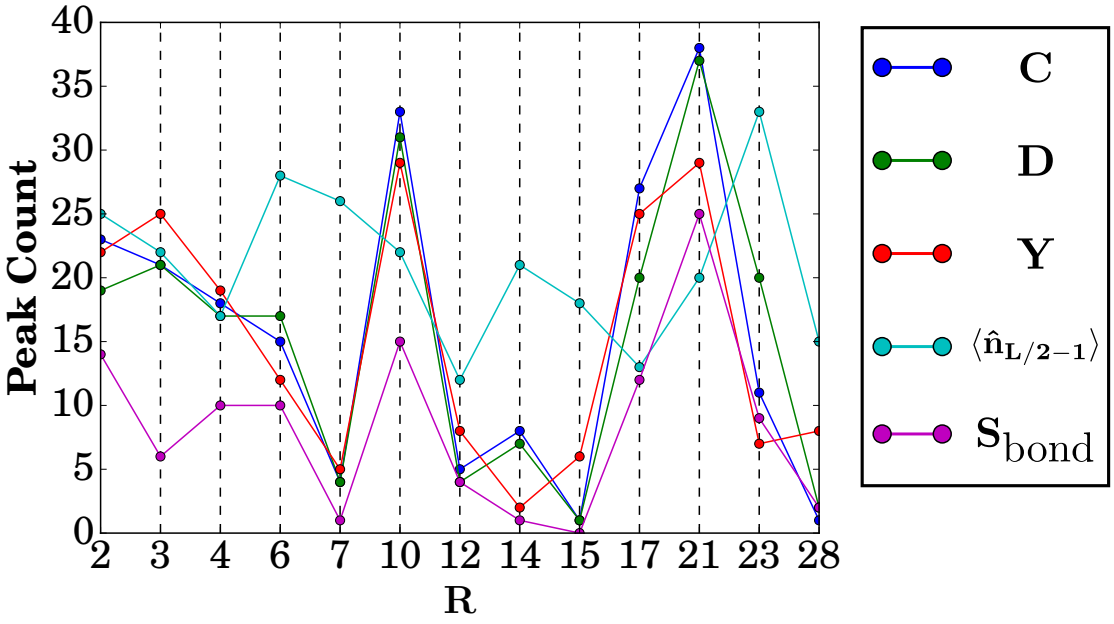

(b)

Fig. 6.8: *Significant peaks in the power spectra of the central bond entropy, complex network measures, and* $\langle \hat{n}_{L/2-1} \rangle$ *for all initial conditions and all rules.* (a) The frequencies of peaks above a red noise spectrum at a 95% confidence level. Different rules produce quantitatively different dynamics in all measures as evidenced by the different frequencies of significant peaks for different rules. (b) Rules 10, 17, and 21 produce many peaks above the red noise threshold for all measures. This indicates the dynamics of these rules are not consistent with red noise. Rules 2, 3, 4, 6 and 23 also have many significant peaks for complex network measures. Rules 2, 4, 6, 10, 17, and 21 produce more significant peaks in the power spectra of S_{bond} than all other rules.

reduced amplitude of fluctuations of the central bond entropy for rule 21, the amplitude of the peaks in its power spectra are often above the red noise threshold. Rule 10, which also thermalizes, has nearly as many significant peaks as rule 21. All other rules have less than 10 significant peaks in the power spectra of the central bond entropy. The significant number of peaks in the power spectra of rule 17 appears to be due to the spatial factorization of rule 17 dynamics for many initial conditions. The spatial factorization produces isolated networks that evolve independently of each other and thus do not interfere with each other. The significant number of peaks in the power spectra of rule 21 are different. Rule 21 dynamics of complex network measures do not exhibit coherent oscillations, they rapidly equilibrate. The power spectra of rule 21 are more irregular. One explanation for this is that the system equilibrates so quickly that it is generating white noise at equilibrium. This would also explain why rules 10 and 21 have significant peaks at higher frequencies than most other rules. Although our red noise analysis allows us to differentiate our dynamics from red noise, it does not quantify the complexity of dynamics as significant peaks may be due to effects of the kind observed in the dynamics of rules 10, 17, and 21. In the next section we study the complexity and entanglement generated by our QCA at late times.

6.4 Late-Time Complexity and Entanglement

In order to understand whether our time evolution schemes generate a new physical class of states displaying high complexity and non-random structure we study the late-time averages of the central bond entropy and complex network measures applied to quantum mutual information networks. In Chapter 3 we studied the quantum mutual information networks of random quantum states and found $D \approx C \approx 3 \times 2^{-L}$, and $Y \approx \frac{1.1}{L-1}$. These formulas allow us to estimate the value of network density, clustering coefficient, and disparity for arbitrary system sizes. To compute late-time averages we average over the last 100 time steps. In Chapter 3 we also found that the central bond entropies of the well characterized entangled states we consider are always equal to 1.

In Fig. 6.9 and Fig. 6.10 we display the late-time averages of our complex network measures for all initial conditions, all system sizes, and all rules as defined in Sec. 6.1. The error bars of the data shown in Fig. 6.9 and Fig. 6.10 are always at least one order of magnitude less than the value of the late-time average. In Fig. 6.11 we study the same data. Instead of averaging the data we now compute histograms. In Fig. 6.9, Fig. 6.10, and Fig. 6.11 we demonstrate that almost all of the quantum states produced by all of our Hamiltonians have network density, clustering coefficient, and disparity above levels consistent with random quantum states. We also find that the quantum states produced by our Hamiltonians are typically highly entangled, with central bond entropy near its maximum. This implies that these states are not like the well characterized entangled states we have considered, the $|GHZ\rangle$, $|W\rangle$, and $|C\rangle$ states, since they have central bond entropy equal to 1 independent of system size. Furthermore, the complex network measures of the quantum states produced by our automata are not consistent with well known quantum states. The values of complex network measures computed on well known quantum state are listed in Eqs. (3.22), (3.24), (3.26), (3.28), and (3.30). The cluster state, the singlet, and the singlet array all have $C = 0$, while the $|W\rangle$ and $|GHZ\rangle$ states have Y that consistent with random states. In Fig. 6.10 we note that Goldilocks rules 2 and 4 generate particularly dense and clustered networks for many initial conditions. However, we also find that the non-Goldilocks rule 17 also produces highly dense and clustered networks for many initial conditions. The outlying data for rule 15 in the C-D plane of Fig. 6.10 may be due to $|S\rangle$ being a near eigenstate of the corresponding Hamiltonian. Inspection of the time series for $|S\rangle$ evolved under the rule 15 Hamiltonian reveals that the clustering changes by less than 2×10^{-4} over the entire simulation. Similarly the network density and disparity of this initial condition are near their initial values of $D = 1/(L-1)$ and $Y = 1$ as described in Eq. (3.26) in Chapter 3. Finally, we do not show outlying data with $C \approx 10^{-16}$ as these points are due to the singlet array being an eigenstate of the rule 17 Hamiltonian. We also exclude a data point with $S_{\text{bond}} \approx 0.4$. This data point is due to a simulation in which rule 17 produces entangled dynamics between sites 9 and

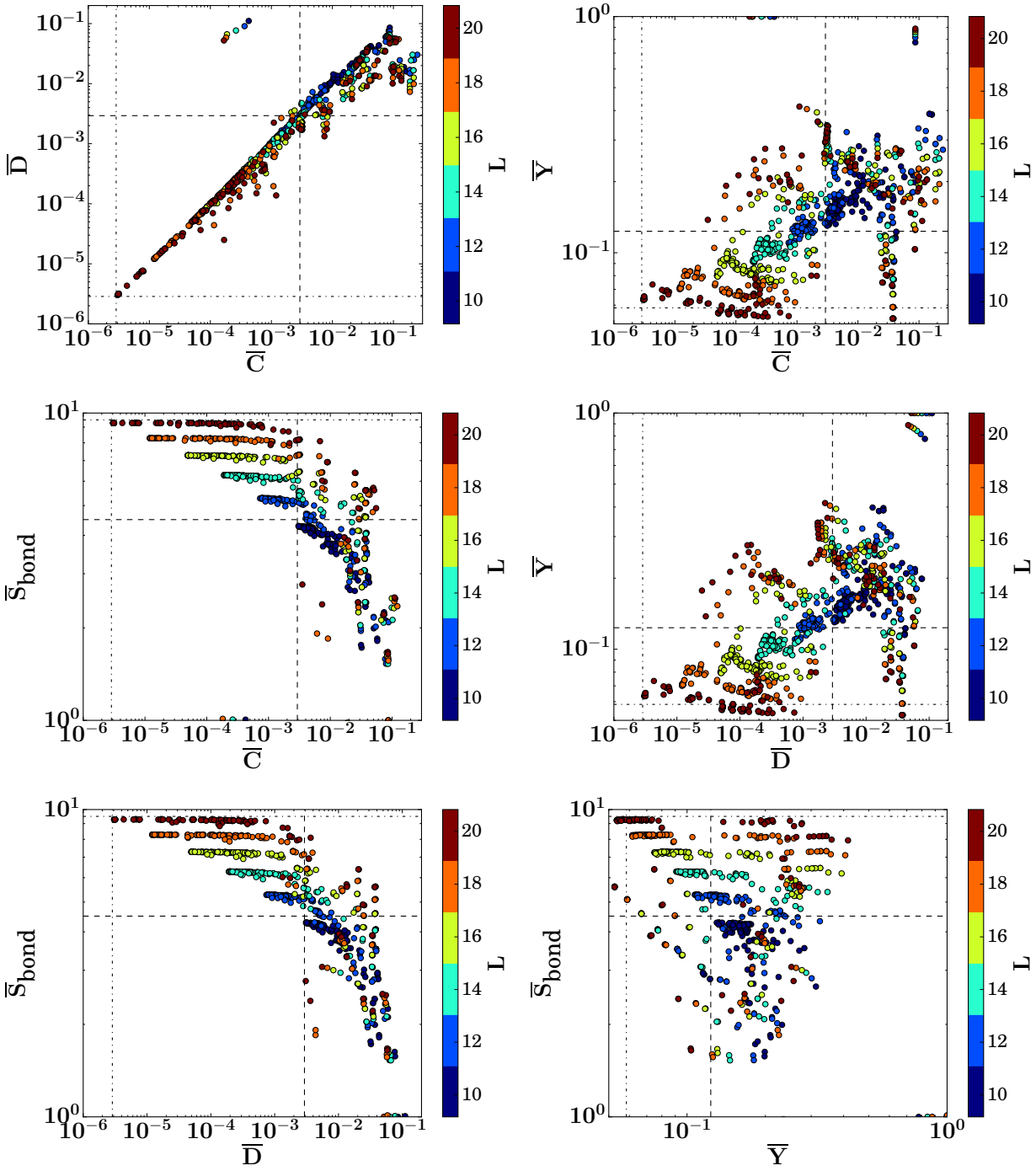

Fig. 6.9: *Late-time averages of complex network measures and the central bond entropy for all system sizes, all initial conditions and all rules color coded by system size.* Prediction for random states of all measures for a lattice of $L = 10$ ($L = 20$) sites are indicated by a dashed (dot-dashed) line. Network density, clustering coefficient, and disparity are far from values consistent with random/well known quantum states. Larger lattices have less clustered and less dense networks. Most simulations are highly entangled at late times with central bond entropy comparable random quantum states.

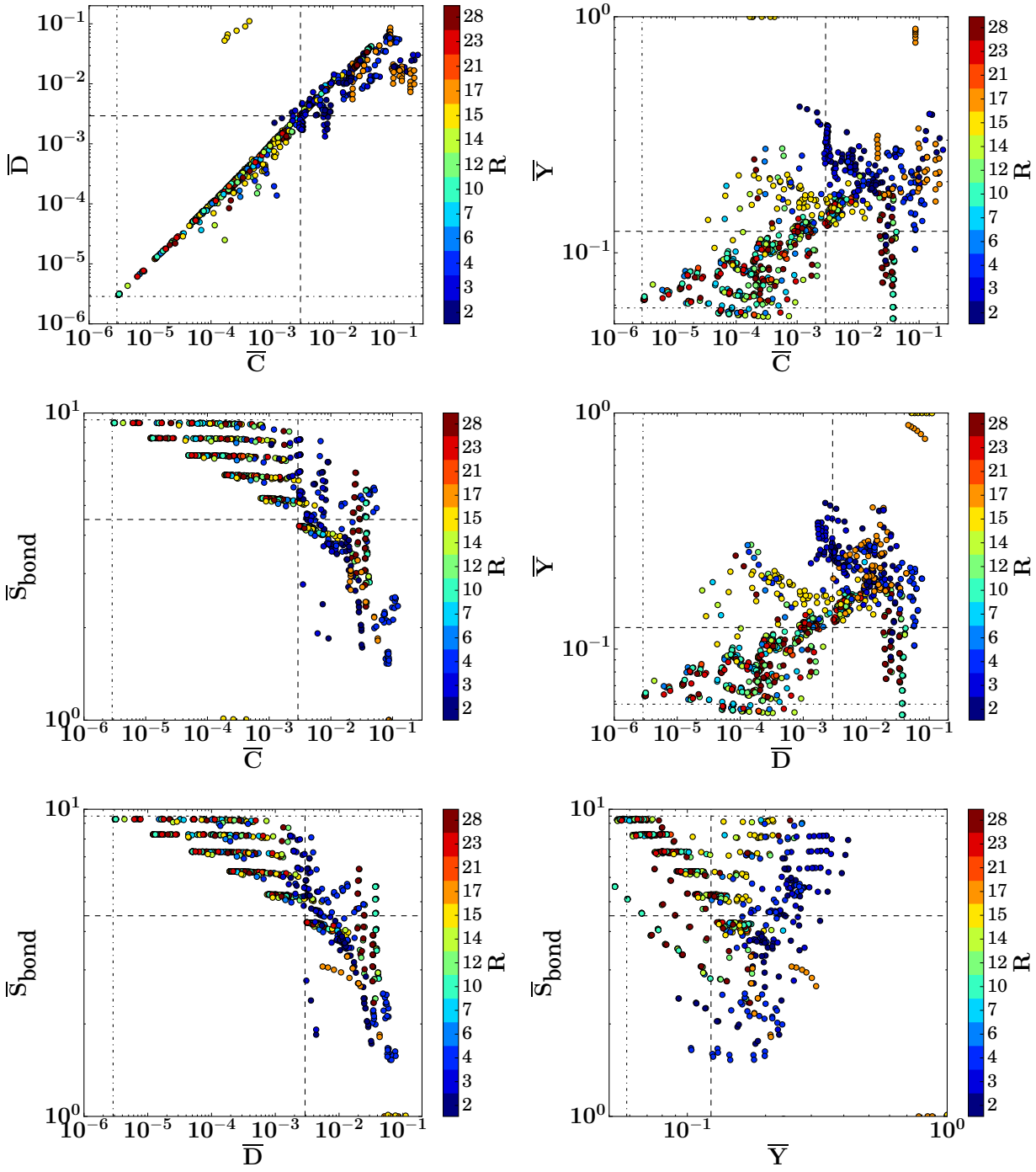

Fig. 6.10: *Late-time values of complex network measures and central bond entropy for all system sizes, all initial conditions and all rules color coded by rule.* Prediction for random states of all measures for a lattice of $L = 10$ ($L = 20$) sites are indicated by a dashed (dot-dashed) line. All rules have complex network measures far from their values for random/well known quantum states. The spatially factorized dynamics of rule 17 produce highly clustered states for most states. Rules 2, 3, and 4 produce highly dense and clustered quantum states.

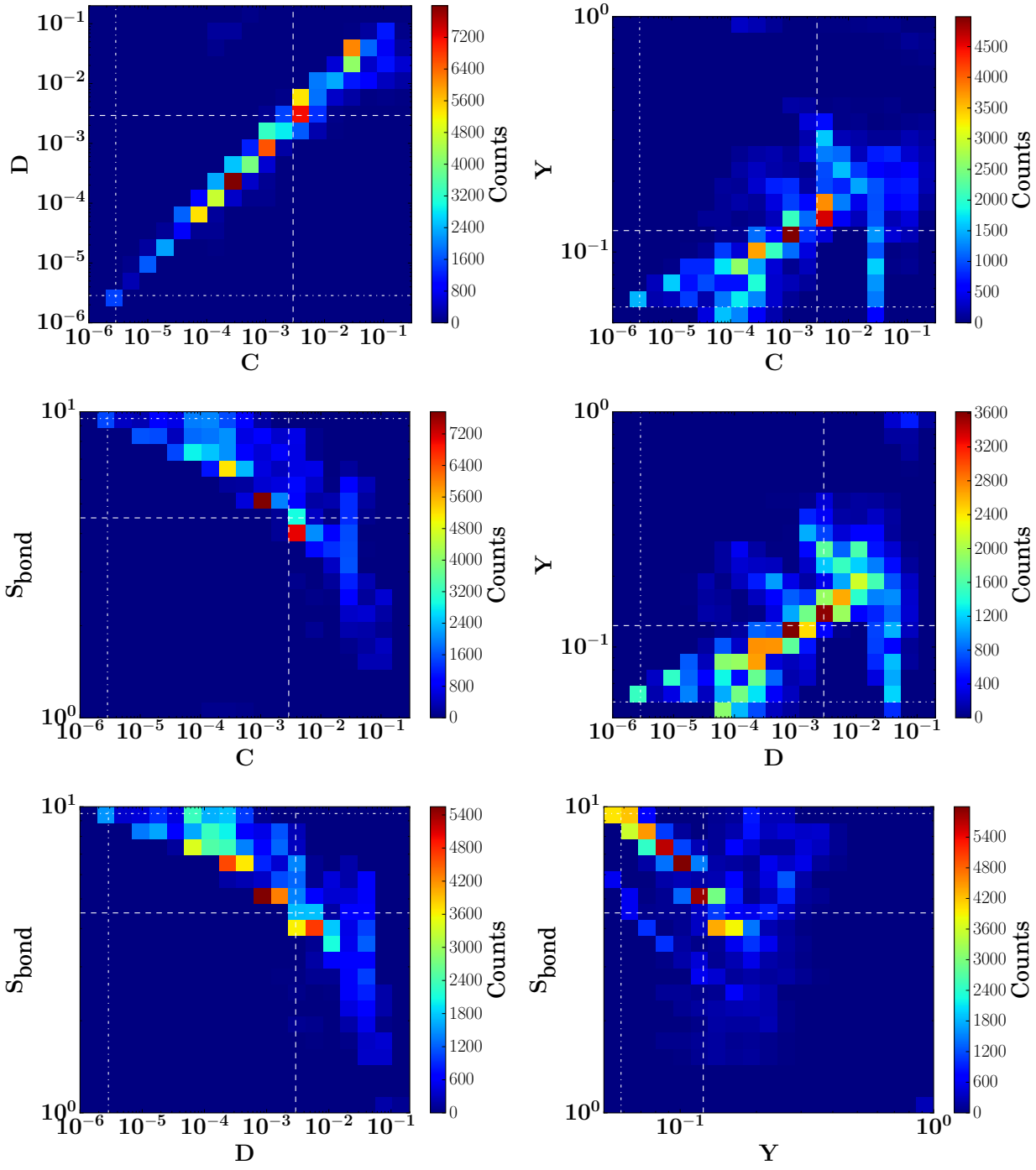

Fig. 6.11: *Histograms of complex network measures and central bond entropy for all system sizes, all initial conditions and all rules over the last 100 time steps of evolution.* Prediction for random states of all measures for a lattice of $L = 10$ ($L = 20$) sites are indicated by a dashed (dot-dashed) line. Almost all simulations equilibrate to values of complex network measures above values consistent with random states. These states are also often highly entangled as quantified by the central bond entropy.

10 on a lattice of 18 qubits. In summary, all rules produce quantum states with complex network measures far from the their values for random/well-known quantum states.

In Chapter 5 we determined that matrix product state methods were not capable of efficiently simulating the dynamics of the BCM Hamiltonian because the BCM Hamiltonian produces too much entanglement and $\chi_{\max}$ is saturated within the first 7 units of simulation time. We then performed a case study of a nearest-neighbor Hamiltonian motivated by rule $S = 6$ of [45]. This case study suggested that it may be possible to simulate certain QCA using OpenMPS. To understand which QCA can be simulated by OpenMPS and to quantify the entanglement generated by our Hamiltonians we study the scaling properties of the late-time central bond entropy $\overline{S}_{\text{bond}}$. In Fig. 6.12 we display $\overline{S}_{\text{bond}}(L)$ for all rules (Eqs. (6.1)-(6.13)). Lines connect simulations of the same initial condition. Most Hamiltonians produce

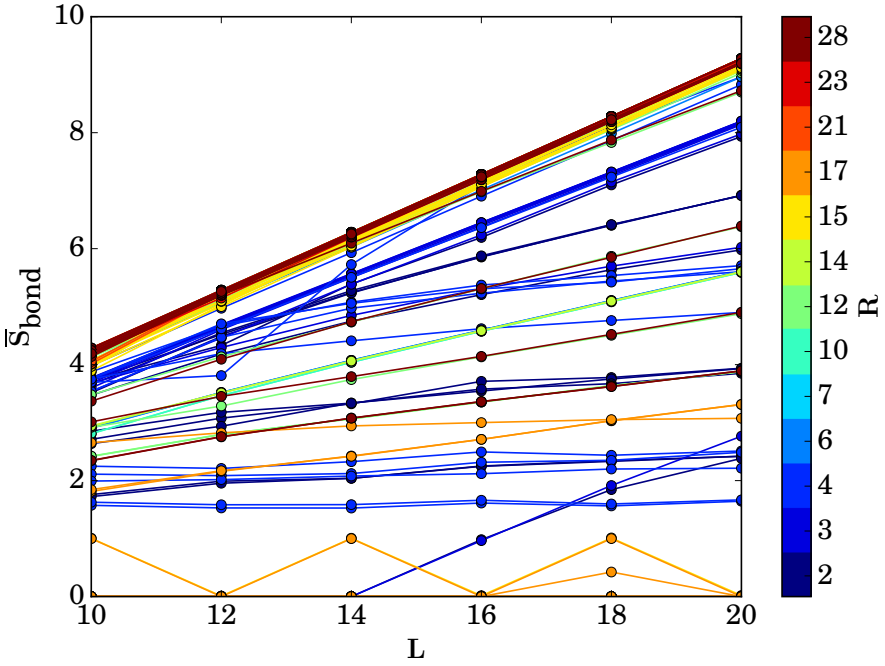

Fig. 6.12: *Scaling of $\overline{S}_{bond}$ for quantum cellular automata for all system sizes, all initial conditions and all rules.* Our Hamiltonian-based QCA typically generate highly entangled quantum states since late-time central bond entropy increases linearly with system size. However, the exceptional rule 4 produces simulations with $\overline{S}_{\text{bond}}$ independent of L for 5 initial conditions. Rule 17 produces simulations with S_{bond} independent of L for initial condition $|C\rangle$. Thus rules 4 and 17 are candidates for simulation in OpenMPS.

late-time bond entropy near the maximum possible value of $L/2$ for many initial conditions. Rules 2, 3, and 4 have late-time bond entropy that increases linearly but with a smaller slope than for many other rules. Rules 12 and 28 also have particular initial conditions for which $\overline{S}_{\text{bond}}$ increases more slowly. These appear to correspond to simulations with blinker-like structures, for which the central bond entropy increases slowly as a function of time. Finally, we find that the Goldilocks rule 4, produces dynamics with S_{bond} independent of system size for five initial conditions: $|B\rangle$, $|D_2\rangle$, $|D_3\rangle$, $|\phi_+\rangle$, and $|\phi_-\rangle$. Interestingly, rule 17, which produces spatially factorized dynamics for many Fock state initial conditions, has dynamics that appear to obey an area law for the cluster state initial condition. This is particularly interesting since rule 17 is the opposite of a Goldilocks rule: it produces activity only when the number of states in the alive state is 0 or 4. The oscillating line for rule 17 is due to $|S\rangle$ being an eigenstate of the rule 17 Hamiltonian.

To demonstrate the convergence of our late-time averages we compare a subset of our simulations to the same simulations with $\Delta t = 0.1/2^3$. Specifically we evolve initial conditions $\{|B\rangle, |D_2\rangle, |D_3\rangle, |T_1\rangle, |T_2\rangle, |T_3\rangle, |T_4\rangle, |\phi_+\rangle, |\phi_-\rangle, |S\rangle\}$ with the BCM Hamiltonian for system sizes $L \in \{10, 12, 14, 16\}$. We denote the absolute difference compared to simulations with $\Delta t = 0.1/2^3$ as ε. The late-time averages of simulations with $\Delta t = 0.1/2^3$ are computed by averaging over the same set of time steps as simulations with $\Delta t = 0.1$. We find that the error in late-time averages is always at least an order of magnitude smaller than the late-time average itself as shown in Fig. 6.13. Furthermore, we find that simulations of larger lattices typically have smaller errors suggesting that the results for lattices of 18 and 20 qubits also have late-time errors at least one order of magnitude smaller than late-time averages. Finally, we also studied the effect of increasing N_{lt} on our late-time averages. We have assured that the late-time averages of all measures are within a factor of 5 of the average computed with $N_{\text{lt}} = 100$ for $N_{\text{lt}} \in \{200, 300, 400, 500\}$.

We also conducted a principal component analysis of our complex network measures over the last 100 time steps for all simulations, we list the principal components in Eqs. (6.29)-

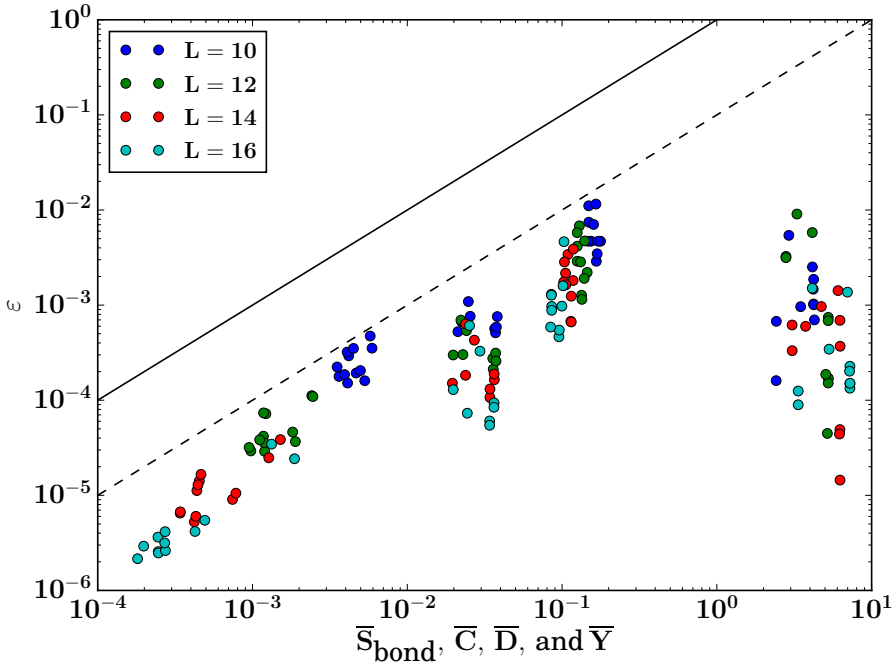

Fig. 6.13: *Error of late-time entanglement and complexity measures for rule 12 evolution of 10 initial conditions.* The error in late-time values of clustering, network density, disparity, and the central bond entropy are at least one order of magnitude smaller than the late-time averages for all simulations.The solid line, $\varepsilon = S_{\text{bond}}$, and the dashed line, $\varepsilon = \frac{1}{10} S_{\text{bond}}$, are plotted to guide the eye.

(6.31). In our principle component analysis we normalize the elements of the covariance matrix by the variances of the individual measures. We find that the first and second principle components of our data set weight network density and disparity approximately equally while clustering is less highly weighted. The third principle component lies almost entirely along the clustering axis. The normalized covariance is greatest along v_1 and v_2. Therefore an ideal set of variables distinguishing different quantum states in terms of complex network measures would lie nearly parallel to the D-Y plane.

$$v_1 = -0.684D - 0.379C - 0.624Y \tag{6.29}$$

$$v_2 = 0.724D - 0.249C - 0.642Y \tag{6.30}$$

$$v_3 = -0.0875D + 0.891C - 0.455Y \tag{6.31}$$

6.5 Late-Time Entanglement of Unitary-Based Quantum Cellular Automata

In contrast to the studies of Sec. 6.4, in this section we will study nearest-neighbor unitary-based quantum cellular automata. These automata are evolved in discrete time as defined in Eq. (2.52) in Chapter 2. In order to quantify the similarities between continuous time Hamiltonian-based QCA and discrete time unitary-based QCA we perform a scaling of the central bond entropy for unitary-based QCA as shown in Fig. 6.14. Instead of the main operator being $\hat{b}_i + \hat{b}_i^\dagger$ as in Sec. 6.4, here the main operator is $\hat{H}_D\hat{P}(\theta)$. Where $\hat{H}_D$ is the Hadamard gate and $\hat{P}(\theta)$. Unitary-based QCA have an additional parameter in the main operator controlling the dynamics of the simulations, the phase gate angle θ. The phase gate angle allows unitary-based QCA to introduce phase to the quantum state over time evolution. Therefore in Fig. 6.14 we also study the effect of θ on the late-time central bond entropy. In [45] rule $S = 6$ was identified as generating the most complex and robust dynamics of all the automata studied. The dynamics were stated to be complex because they exhibited persistent fluctuations of the central bond entropy and robust because these fluctuations were not sensitive to changes in phase gate angle [45]. We find that rule $S = 6$

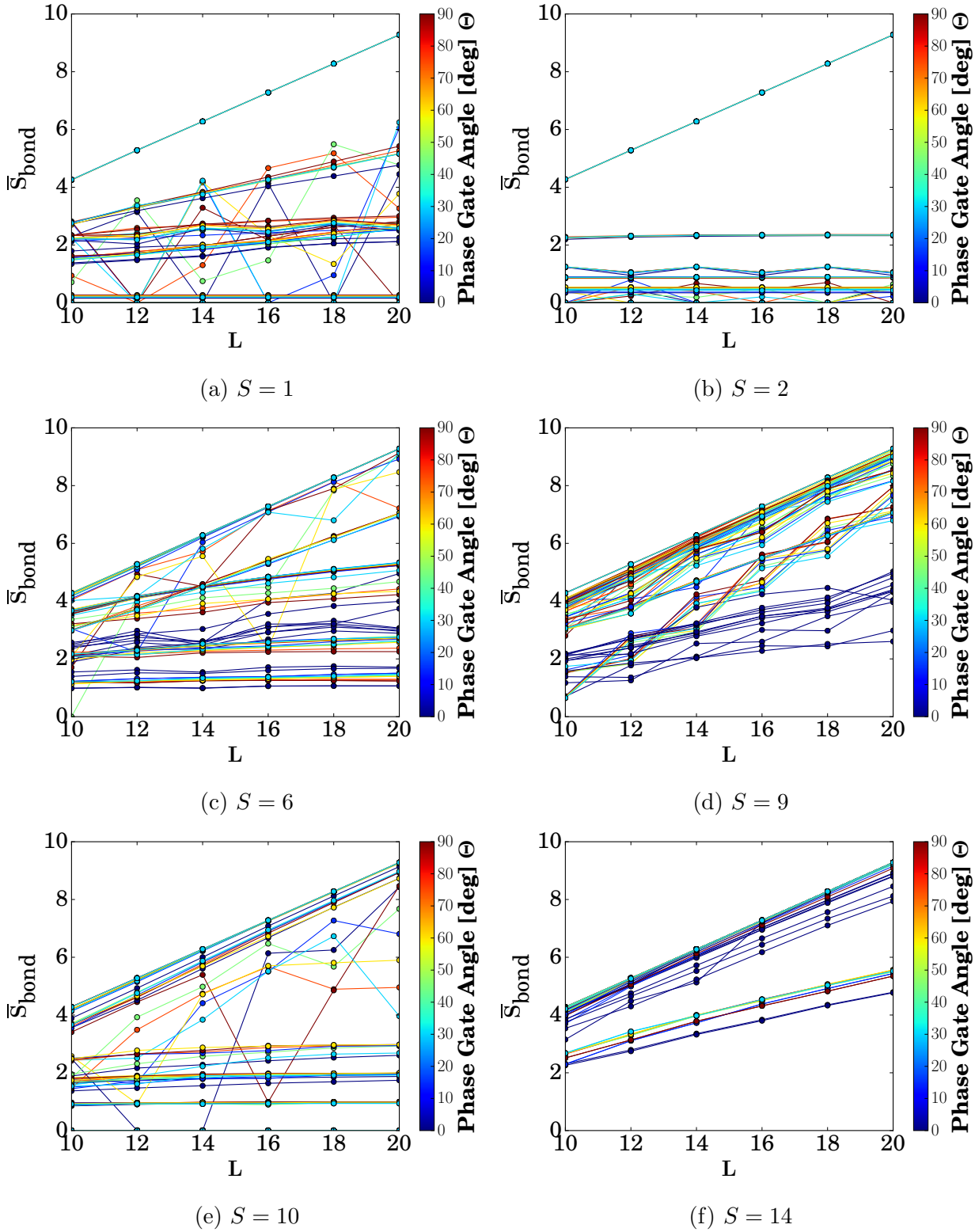

(a) $S = 1$ (b) $S = 2$

(c) $S = 6$ (d) $S = 9$

(e) $S = 10$ (f) $S = 14$

Fig. 6.14: *Scaling of $\overline{S}_{bond}$ for unitary-based QCA for all initial conditions.* Rules $S \in \{6, 9, 14\}$ were identified as complexity generating in [45]. We find that rules 2, 6, and 10 generate $\overline{S}_{\text{bond}}$ that is independent of L. Thus rules 2, 6, and 10 are candidates for simulation with tensor network methods. The erratic lines in (a), (c), and (e) are from initial condition $|R_3\rangle$.

produces dynamics with $\overline{S}_{\text{bond}}$ independent of L for many initial conditions independent of phase gate angle as shown in Fig. 6.12. Rule $S = 2$, which was not found to have persistent bond entropy fluctuations in [45], also produces dynamics with $\overline{S}_{\text{bond}}$ independent of L for certain initial conditions. The amount of entanglement is tunable by the phase gate angle as shown in Fig. 6.14(b). Rule $S = 1$ produces a set of very lowly entangled simulations with constant $\overline{S}_{\text{bond}}$ as a function of L, however most simulations have late-time central bond entropy that increases linearly with system size. Although rules $S = 9$ and $S = 14$ were also identified as complexity generating it was found that the fluctuations of the central bond entropy of these rules was drastically reduced by small changes in the phase gate angle [45]. We find that both of these rules have $\overline{S}_{\text{bond}}$ that increases linearly with L. We also found that the slope of $\overline{S}_{\text{bond}}(L)$is significantly increased for simulations with non-zero phase gate angle for rule $S = 9$.

6.6 Persistent Entropy Fluctuations of Hamiltonian-Based Quantum Cellular Automata

We now return to our study of Hamiltonian-based QCA, studying fluctuations of the central bond entropy at late times for the rules defined in Eqs. (6.1)-(6.13). To quantify persistent fluctuations of the central bond entropy we evolve a random quantum state, $|r_3\rangle$, under all 13 of our Hamiltonians. We then compute the level of fluctuations of the central bond entropy at late times for each of these simulations. We compute the average level of fluctuations for the random initial condition $\overline{\Delta S}(|r_3\rangle)$ at late times by averaging over the $\overline{\Delta S}$ of each of our Hamiltonians for initial condition $|r_3\rangle$. We also compute the standard deviation of the late-time averages $\sigma(\overline{\Delta S}(|r_3\rangle))$. We define any simulation with late-time average fluctuations of the central bond entropy greater than $\Delta S(|r_3\rangle) + \sigma(\Delta S(|r_3\rangle))$ as displaying persistent fluctuations of the central bond entropy. In Fig. 6.15(a) we plot the level of late-time fluctuations for each of our simulations of non-random initial conditions organized by rule. From Fig. 6.15(a) we can see that there are two types of rules, rules that generate late-time average fluctuations of the central bond entropy that span orders

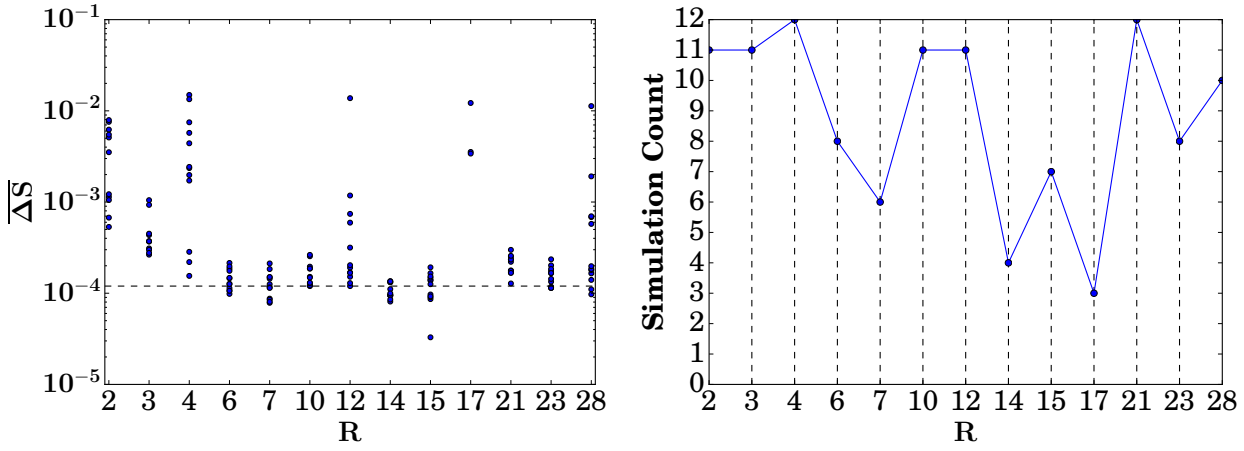

(a) (b)

Fig. 6.15: *Fluctuations of the central bond entropy at late times for a lattice of 20 qubits.* (a) The dashed line corresponds to $\overline{\Delta S}$ for initial condition $|r_3\rangle$ averaged over all rules plus one standard deviation. Simulations with $\overline{\Delta S}$ above this line exhibit persistent fluctuations of the central bond entropy (b) Count of the number of simulations with fluctuations above levels consistent with initial condition $|r_3\rangle$ for each rule. Rules 2, 3, 4, 10, 12, 21, and 28 have persistent fluctuations of the central bond entropy for almost all initial conditions. This indicates these rules may be complexity generating.

of magnitude with $\overline{\Delta S} > 10^{-3}$ for at least one simulation (rules 2, 4, 12, 17, and 28) and rules that do not (rules 3, 6, 7, 10, 14, 15, 21, and 23). Interestingly, this is not the same as the set of rules that consistently generate dynamics above levels consistent with random quantum states. In Fig. 6.15(b) we count the number of simulations displaying persistent fluctuations of the central bond entropy for each rule. Rules 2, 3, 4, 10, 12, 21, and 28 generate dynamics above levels consistent with random quantum states for nearly all initial conditions. Goldilocks rules 2 and 4 are particularly notable for producing dynamics with fluctuations above 10^{-3} for many initial conditions. Because the dynamics of rule 17 often spatially factorize it usually has fluctuations below levels consistent with random quantum states. However rule 17 is still notable in terms of fluctuations of the central bond entropy; specifically it generates persistent fluctuations of the central bond entropy for the cluster state initial condition. In summary, we find that both Goldilocks and non-Goldilocks rules produce simulations with persistent entropy fluctuations. We also find that both Goldilocks

rules and non-Goldilocks rules produce entropy fluctuations at late times that span orders of magnitude over different initial conditions. Finally, we find that Goldilocks rules 2 and 4 produce more dynamic entanglement in simulations than all other rules as quantified by fluctuations of the central bond entropy greater than 10^{-3} for many simulations.

6.7 Blinker Case Study

In Sec. 6.2 we found that rules 4, 12, and 28 produce a quantum blinker pattern for initial condition $|B\rangle$. This initial condition displayed persistent fluctuations in bond entropy for all three rules, indicating that their dynamics exhibit a robust dynamical feature. In that section we also noted that the blinker initial condition does not approach a constant value of the central bond entropy for rules 12 and 28 with $L = 20$ and $t_f = 100$. Its average value continued to grow during the entire simulation. In this section we show that the blinker initial condition evolved under rule 12 displays long term logarithmic growth of the central bond entropy, we study how the dynamics of the blinker responds to a perturbing potential, and we study the late-time central bond entropy as a function of the distance between two blinkers. To assess whether the central bond entropy saturates over accessible time scales we simulated the blinker initial condition with $t_f = 1000$. The blinker initial condition clearly displays long term logarithmic growth of the central bond entropy as shown in Fig. 6.16, logarithmic growth of the central bond entropy is also found in models of many-body localization [89].

To assess the response of the blinker pattern to a perturbing potential we add a linear perturbation to the rule 12 Hamiltonian,

$$H' = a \sum_{i=1}^{L} \hat{n}_i i \,. \tag{6.32}$$

In Fig. 6.17(a) we show that as the slope of the perturbing potential is increased the bond entropy transitions between coherent oscillations and simple fluctuations. A certain value of the perturbing slope appears to maximize $\overline{S}_{\text{bond}}$. We confirm this in Fig. 6.17(b). The late-time bond entropy is maximized for a value of the perturbing slope $a \leq 0.2$ for all system sizes. The value of the perturbing slope that maximizes the central bond entropy decreases

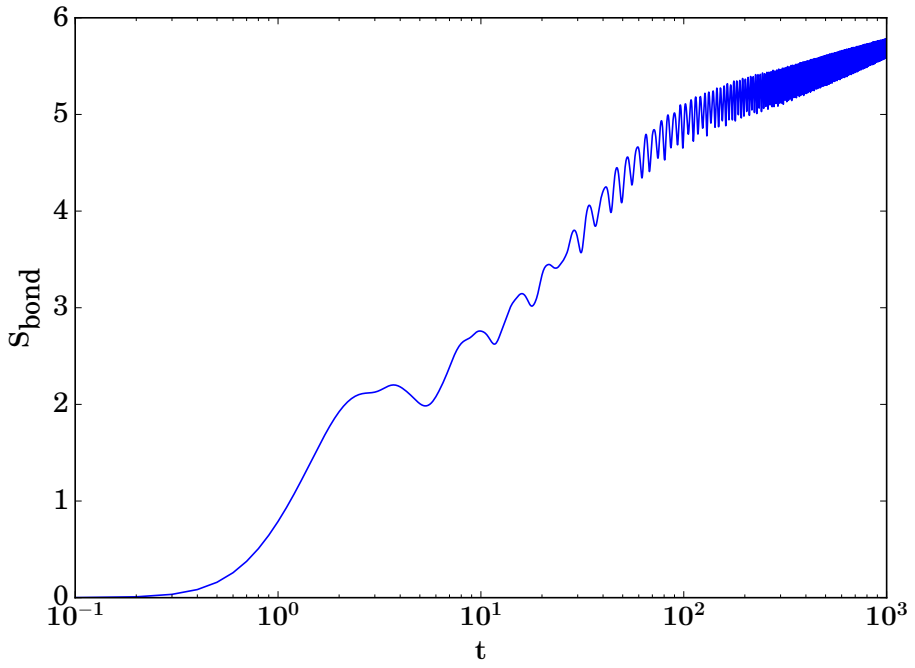

Fig. 6.16: *Long time simulation of the quantum blinker of rule 12.* Initial condition $|B\rangle$ displays long term logarithmic growth of the central bond entropy. This is different than all other simulations, which either equilibrate to a constant value of the central bond entropy within the first 100 units of time or fluctuate about a constant value of the central bond entropy.

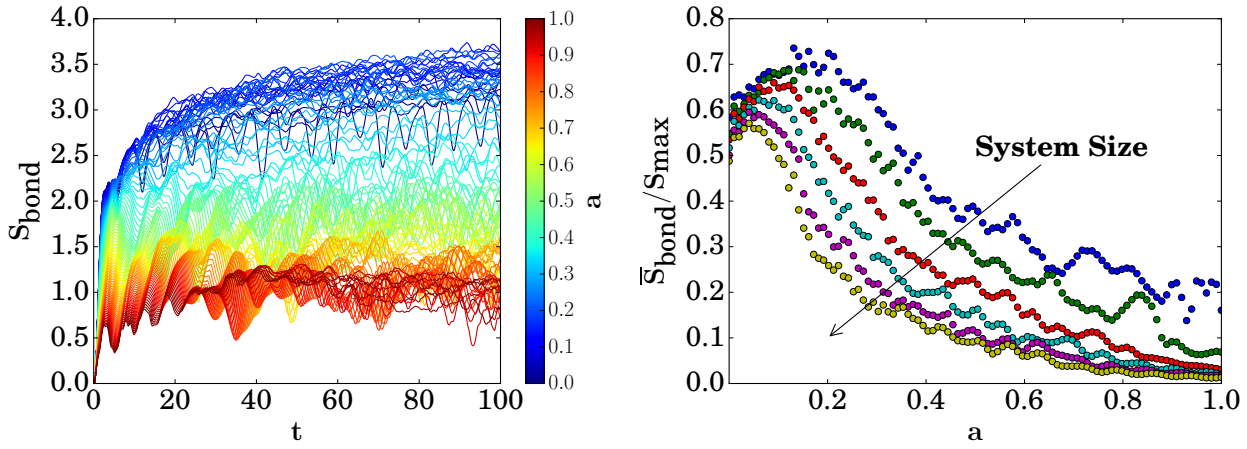

(a) (b)

Fig. 6.17: *Response of the quantum blinker evolved under rule 12 on a lattice of 20 qubits to a perturbing potential.* (a) The unperturbed blinker displays coherent oscillations in the bond entropy. For small values of the perturbation gradient the blinker initial condition no longer displays coherent oscillations and saturates to a higher bond entropy. (b) The late-time bond entropy is maximized for a value of the perturbing slope $0.1 \lesssim a \lesssim 0.2$. Increasing the slope past this point leads to an abrupt decrease in the late-time bond entropy and a return to coherent oscillations in the bond entropy. As system size is increased the value of the perturbing field maximizing the late-time bond entropy decreases. The subsequent decrease of $\overline{S}_{\text{bond}}$ as a function of a is also more sudden for larger system sizes.

as a function of system size, however the maximum value of the central bond entropy also approaches the value of the unperturbed blinker. After this maximum is reached $\overline{S}_{\text{bond}}$ rapidly decreases as a function of the perturbing slope. The decrease in $\overline{S}_{\text{bond}}$ is more abrupt for larger system sizes. However, Fig. 6.16 suggests that these results would likely change substantially for longer simulation times, at least for simulations exhibiting coherent dynamics in S_{bond}.

Because we found that the entanglement properties of a single blinker can be tuned via its interaction with an external perturbation we also study the interactions between two blinkers in Fig. 6.18. Two blinker initial conditions are defined as

$$|...0101\rangle \otimes |0\rangle^{\otimes n} \otimes |1010...\rangle \ . \tag{6.33}$$

That is, two blinkers are separated by n sites in the dead state $|0\rangle$. Two blinker initial

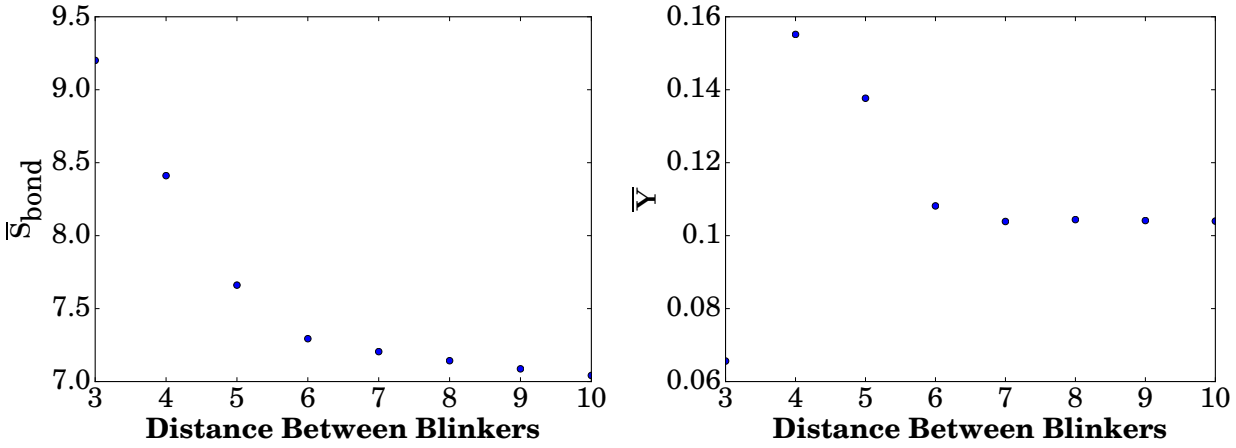

(a) (b)

Fig. 6.18: *Late-time Entanglement and disparity of two blinker initial conditions evolved under rule 12 on a lattice of 20 qubits.* (a) The amount of entanglement can be tuned by the initial condition, for blinkers separated by three sites $\overline{S}_{\text{bond}}$ is greater than 9, however for blinkers separated by 10 sites the $\overline{S}_{\text{bond}}$ is reduced to 7. (b) $\overline{Y}$ quickly approaches a constant value as the distance between two blinkers becomes greater than 6 sites and blinkers become well localized.

conditions do not display fluctuations in the central bond entropy. Instead the central bond entropy saturates near its maximum value when blinkers are separated by only three sites

and near 0.7 when blinkers are separated by 10 sites. Unlike single blinker initial conditions, two blinker initial conditions saturate to a constant bond entropy for $t < 100$. We found that the late-time average values of network density, clustering coefficient, and disparity are not consistent with random quantum states for any distance between two blinkers. Inspection of the space-time plots of two blinker initial conditions (not shown) reveals that blinkers stabilize into independently oscillating patterns when separated by 5 or more sites. This together with the results on $\overline{Y}$ shown in Fig. 6.18 demonstrate that the effective size of blinkers is about 7 sites.

In this chapter we have studied the 13 Hamiltonian-based quantum cellular automata defined in Eqs. (6.1)-(6.13). From our different lines of analysis we find that rule 4 best meets our definition of a complexity generating rule. It consistently produces persistent fluctuations of the central bond entropy, has many significant peaks in the power spectra of the central bond entropy, has complex network measures far from their values for random/well-known quantum states, and exhibits a robust dynamical feature, the quantum blinker. We have thus verified the hypothesis that only Goldilocks rules are complexity generating. Furthermore, we found that the 6 of the 8 non-Goldilocks rules studied have significantly reduced fluctuations of the central bond entropy. This confirms our hypothesis that non-Goldilocks rules tend toward thermalization. Finally, our of the scaling properties of $\overline{S}_{\text{bond}}$ revealed that Hamiltonian-based QCA typically generate highly entangled quantum states. However we also found exceptional initial conditions for which both Goldilocks and non-Goldilocks rules generate $\overline{S}_{\text{bond}}$ that is independent of system size. In our study of nearest-neighbor unitary-based QCA in Sec. 6.5 we also found that both the Goldilocks rule $S = 6$ and the non-Goldilocks rules $S = 2$, 10 generate $\overline{S}_{\text{bond}}$ that is independent of system size. Combinations of initial condition and rule that produce lowly entangled dynamics at late-times are candidates for simulation with OpenMPS.

CHAPTER 7

CORRELATION BETWEEN STUDENT COLLABORATION NETWORK CENTRALITY AND ACADEMIC PERFORMANCE

In this chapter we present our complex network analysis of student collaboration networks of upper-division physics students enrolled at the Colorado School of Mines. This work was done in collaboration with Ariel Bridgmen[2], David Schmidt[3], and Pat Kohl[4].

7.1 Introduction

Physics education research has enjoyed a great deal of success in identifying and clarifying misconceptions about physics concepts, developing problem solving methods, and structuring the knowledge that is taught to students [90, 91, 92, 93, 94]. Such studies have allowed researchers to make quantitative statements about students' misconceptions, in contrast to traditional physics education that relied on anecdotal information [91]. A powerful tool for analysis in the social sciences is complex network theory [95, 4]. Surprisingly, this tool has almost entirely been overlooked in education research [96, 50]. Using complex network theory we study how the collaboration of students evolves between semesters, and how nodal centrality measures correlate with homework vs. exam grades. Furthermore, we compute the differences in correlation strengths between our measures, allowing us to quantify which measures are telling us the most about student grades. Finally, we also compare the network centrality of students between the collaboration networks of different types of homework assignments within a single course, allowing us to assess the similarity of roles adopted by students in response to different assignments.

Complex network measures provide succinct summaries of the order present in complex networks. Often such measures are aggregate summaries of the entire structure of a network

[2]Secondary researcher and Secondary author
[3]Secondary researcher and Secondary Author
[4]Secondary author

and are useful because the structure of connectivity can determine the efficiency of processes taking place on the network as observed in social, neural, communication, and transportation networks [4, 66]. Furthermore, the nodal centrality measures we review in section 7.4 tell us how well connected students are in the context of their homework collaboration networks [67, 64]. A simple measure of how well connected a node is is encapsulated by the *out-strength* of a node. Out-strength is simply the number of other students a students helps with homework, and is thus a natural measure of the influence of student in a collaboration network. Parallel to out-strength is *in-strength*, the number of students that help a particular student with homework. While out-strength can be thought of as a coarse measure of the influence of a student on the collaboration network, in-strength is a measure of how a student gathers information from different parts of the network. A more sophisticated measure of how well connected a node is is *closeness centrality*, which measures the average distance of a student to all other students in the network. Thus, closeness centrality is a more refined measure of how widely a student collaborates across the network, and measures a student's access to the reasoning of others. In contrast to closeness centrality, *betweenness centrality* quantifies the importance of a student by their ability to control information flow between other students, and not by their ability to influence the network directly. The variety of complex network measures we consider provide us with different perspectives of the students forming our collaboration networks. The correlation of each measure with student grade indicates that a distinct form of optimal collaboration is linked to higher grades. The aggregate correlation of our measures with student grade provides a clear picture of how strongly and in what manner collaboration is central to the educational process.

We note only two previous studies utilizing complex network-based methods in education research [96, 50], despite the thousands of applications in the areas of the physical, biological, and social sciences [4]. In the first, the epistemic framework of students is analyzed [96]. In the second, a preliminary baseline is established in introductory physics courses in Denmark: collaboration amongst the general student population engaged in such courses correlates with

their grades. In contrast, our study focuses on the discipline specific population endemic to upper division physics courses [50]. Using a wide variety of complex network measures we obtain detailed information about the role of different collaboration strategies in problem sets, exams, and student performance trajectories over time. As social relationships are integral to student collaboration, we encourage more research to be done on the collaborative networks at other universities. This will provide additional context for such studies and help us identify what forms of collaboration are universal predictors of grades, and which measures are particular to certain networks.

At the most basic level we are trying to address the question: Do well-connected students have good grades? Perhaps students with access to the reasoning of many of their peers are better equipped to complete homework assignments, but then again it may be that excessive participation in a collaboration network can stifle the ability of a student to perform well on their own work. It seems intuitive that collaboration should improve student performance on homework, but will the benefits of collaboration extend to exams, where a student does not have access to their collaborators? Finally, how stable are these measures in different contexts? That is, do students tend to take on different roles in response to different types of assignments? Are student's collaboration strategies static? Maybe they are formed in response to a student's performance, or maybe the collaboration network of a student facilitates improvements in grades.

7.2 Data Collection

The Colorado School of Mines (Mines) is a public research university in Golden, Colorado. The university, which has close to six thousand undergraduate and graduate students, focuses on engineering and the applied sciences. Additionally, it is one of very few institutions that awards more than 50 Physics Bachelors per year, and has averaged fifty five such degrees between 2012 and 2014, placing it in the top ten of all Ph.D. granting departments in the U.S. [97]. The physics department has research focus areas in condensed matter, subatomic, optical, renewable energy, theoretical, and computational physics.

The data for our networks was collected over two semesters: Fall 2012 and Spring 2013. Students in their junior year in engineering physics take classical mechanics during the Fall semester and both quantum mechanics and electromagnetism during the Spring semester. The course in classical mechanics covers Lagrangian and Hamiltonian mechanics. The course in quantum mechanics introduces the formalism of quantum mechanics, the solutions of a particle in a box, scattering from a potential well, etc.. We summarize the course information for the three courses in Fig. Fig. 7.1. Prior to their junior year at Mines, physics majors are encouraged to collaborate in a physics studio setting, a setting in which students work in groups of three to complete homework-like assignments and labs. Additionally, the summer before their junior year Mines physics majors participate in a physics field session in which groups of ten students move between sections on computing, vacuum systems, machining, and lasers. In all of these sections students are encouraged to collaborate, and in some of them students are split into groups of three to complete assignments. Thus collaboration is a strong part of Mines' lower-division program already, and is strongly encouraged.

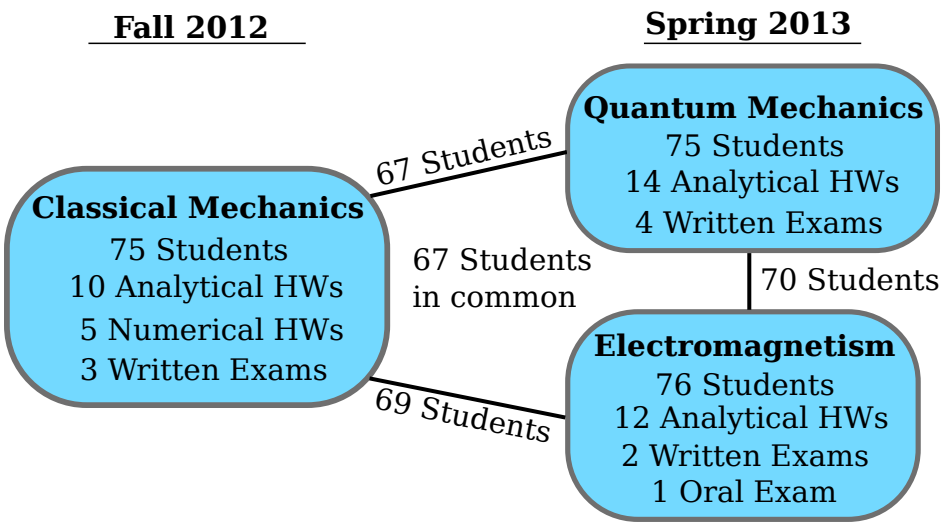

Fig. 7.1: *Course information for classical mechanics, quantum mechanics, and electromagnetism.* Lines connecting two courses indicate the number of students common to both courses. There were 67 students enrolled in all three courses.

There were two forms of data collection: paper forms during Fall 2012 and electronic spreadsheets during Spring 2013. In the paper form of data collection students were provided with a form for each assignment in which they were to list any students they helped or received help from for each assigned problem. In the electronic form of data collection, students provided the same data by entering the names of their collaborators into question/answer boxes on Blackboard [98]. In both cases, students were required to complete the surveys described above in order to receive credit for their homework assignments. This policy incentivized survey completion and ensured a nearly complete set of data. Student names were then immediately replaced with a set of randomly generated three letter codes to anonymize the data prior to analysis.

The data from the surveys above was compared with student grades in the three courses. The course in classical mechanics had ten analytical homework assignments, five numerical homework assignments, and three written exams. For numerical assignments, students were asked to simulate various physical scenarios using Mathematica. For the course in classical mechanics, we computed three measures of a student's performance: the sum of their analytical homework grades, the sum of their numerical homework grades, and the sum of their exam grades. For the course in quantum mechanics we measured a student's performance by the sum of their homework grades and the sum of their exam grades, and for the course in electromagnetism, we measured a student's performance by the sum of their homework grades and the sum of their exam grades. It is important to note that in classical mechanics the teaching assistants grade exams with subsequent review by the instructor. In quantum mechanics and electromagnetism the instructors graded all exams themselves. Finally, the instructors of quantum mechanics and classical mechanics both applied curves to exam grades, while the instructor of electromagnetism did not.

7.3 Methodology for Converting Data into Networks

From the data collected in the surveys above we constructed directed networks for each homework assignment using the following procedure. A network is a collection of nodes and

links. Nodes are any object that can be connected to any other object by some relation. Links are the connections between nodes. In our networks, nodes correspond to students, and a link corresponds to providing or receiving assistance. Note that this is not a symmetric relation, as i helps j does not imply j helps i. This is the defining feature of a directed network; its connections are asymmetrical. For directed networks, one says that a link goes from node i to node j to indicate the direction of the link. For the k^{th} network a link is placed from node i to node j if and only if (iff) student i helped student j with homework assignment k. Summarizing our network in terms of the entries of an adjacency matrix,

$$A_{ij}^{k} = \begin{cases} 1 \text{ iff student } i \text{ helped student } j \text{ with homework assignment } k \\ 0 \text{ otherwise.} \end{cases} \tag{7.1}$$

However, we found that it was necessary to resolve discrepancies in the reports provided by students. For example, student i may claim that they helped student j, but student j's survey indicates that they did not receive help from student i. These discrepancies may be due to forgetfulness or conflicting perceptions of interactions. To resolve the discrepancies in student reports, we employed a *Maximal* discrepancy resolving technique [99, 100]. Applying an element wise logical OR to the adjacency matrices arrived at from each student's survey to arrive at a final network. That is, every reported interaction is considered to have happened even if one student does not report it. Discrepancies can occur in either direction of an interaction, and A_{ij} is resolved separately from A_{ji}. Other discrepancy sorting cases were investigated but yielded quite sparse adjacency matrices [99, 100]. For each course, we then compute a weighted adjacency matrix by summing the adjacency matrices corresponding to the homework assignments in that course,

$$A_{ij} = \sum_{k=1}^{N_{\text{HW}}} A_{ij}^{k} \,. \tag{7.2}$$

Where N_{HW} is the number of homework assignments in the relevant course. Thus if two students i and j collaborated frequently on homework assignments they will have a heavily weighted connection in one of the weighted networks depicted in Fig. Fig. 7.2. In Fig. Fig. 7.2

nodes are indicated by circles and the links connecting nodes are indicated by the arrows between nodes. The direction of the arrow indicates the direction of assistance. For the course in classical mechanics, we also construct networks for the numerical homework assignments and the analytical homework assignments separately. This procedure results in two networks for the course in classical mechanics: a network constructed from the collaboration networks on analytical assignments A_A^{CM} and a network constructed from the collaboration networks on numerical assignments A_N^{CM}. We denote the network for the course in quantum mechanics by A^{QM}, and the network for the course in electromagnetism as A^{EM}.

7.4 Complex Network Analysis

Using NetworkX network analysis software [62], as well as some of our own independently developed network analysis code, we study the networks described in the previous section by computing various nodal centrality measures and other measures of the structure of a node's connections. We then compute the correlation between these measures and different estimators of student performance. Nodal centrality measures are measures of a node's importance to the structure of the network. As they are quantitative measures of each student's role in the collaboration network, nodal centrality measures are ideal for our study. Our selection of standard complex network measures includes out-strength, in-strength, out-disparity, in-disparity, local clustering, closeness centrality, harmonic centrality, and betweenness centrality. The local clustering coefficient is only defined on undirected networks. Before computing the local clustering coefficient we first convert our directed networks into undirected networks as such that, $A_{ij}^{\mathrm{undirected}} = \max\left(A_{ij}, A_{ji}\right)$.

The *out-strength* of a node is the sum of its outgoing connections to other nodes and is defined as

$$s_i^{\mathrm{out}} = \sum_{j=1}^{L} A_{ij}\,. \tag{7.3}$$

A node can have high out-strength if it has outgoing connections to many other nodes, or if it has strong connections to only a few other nodes. Stated simply, students who help many

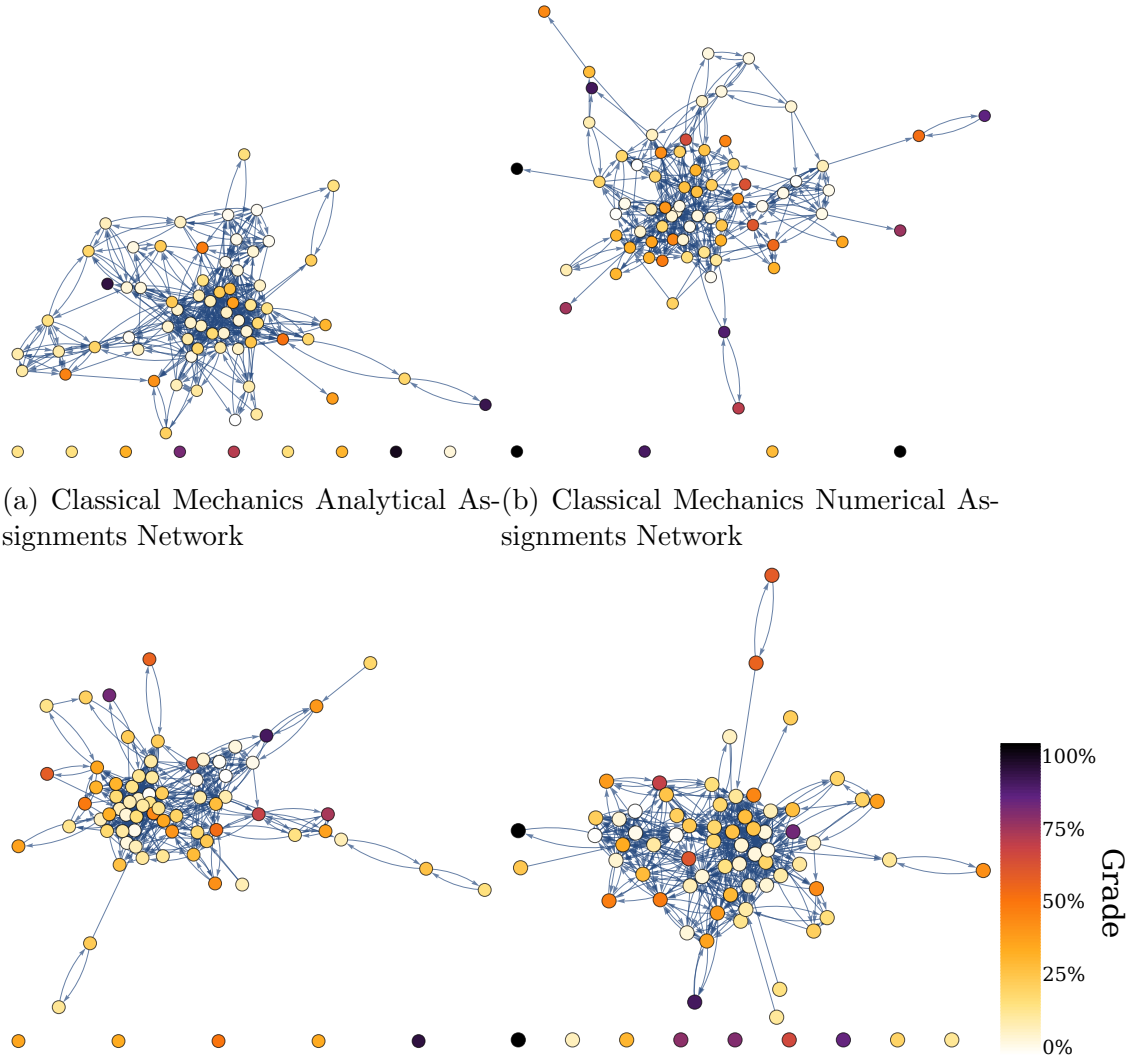

(a) Classical Mechanics Analytical Assignments Network

(b) Classical Mechanics Numerical Assignments Network

(c) Quantum Mechanics Assignments Network

(d) Electromagnetism Assignments Network

Fig. 7.2: *Student collaboration networks for three upper level physics courses.* Student collaboration networks constructed from surveys given to students in three upper-division courses, classical mechanics, quantum mechanics, and electromagnetism. Nodes correspond to students and the direction of each arrow indicates the direction of assistance on homework assignments. The color of a node indicates the grade of a student on homework assignments. Although we do not normalize grades in our analysis we present grades as a percentage here to illustrate multiple courses simultaneously.

of their peers and students who frequently help a smaller set of peers both can have a high out-strength. The *in-strength* is similarly defined and distinguishes a node by the number of incoming connections

$$s_i^{\text{in}} = \sum_{j=1}^{L} A_{ij}^T \,, \tag{7.4}$$

or the number of instances in which a student received help. We also study the *net out-strength*

$$s_i^{\text{net}} = s_i^{\text{out}} - s_i^{\text{in}} \,. \tag{7.5}$$

Students with high net out-strength correspond to students that help many other students but are not helped by many students.

The *out-disparity* of a node's connections is a measure of the non-uniformity of the outgoing connection strengths. If a node has a single strong connection in addition to other, much weaker connections, the node has high out-disparity. If the connection strengths of a node are all approximately equal strength, then it has a low out-disparity. Out-disparity is defined as [61, 14]

$$Y_i^{\text{out}} \equiv \frac{1}{\left(s_i^{\text{out}}\right)^2} \sum_{j=1}^{L} \left(A_{ij}\right)^2 = \frac{\sum_{j=1}^{L} \left(A_{ij}\right)^2}{\left(\sum_{j=1}^{L} A_{ij}\right)^2} \,. \tag{7.6}$$

Nodes with high disparity correspond to students that collaborate with certain nearest neighbors much more often than they collaborate with other nearest neighbors. Nodes with low disparity correspond to students that collaborate equally with all students that they collaborate with. Analogously, *in-disparity* measures the non-uniformity of the incoming connection strengths. To compute Y_i^{in} one makes the substitution $A \to A^T$ in Eq. (7.6), resulting in

$$Y_i^{\text{in}} \equiv \frac{1}{\left(s_i^{\text{in}}\right)^2} \sum_{j=1}^{L} \left(A_{ij}^T\right)^2 = \frac{\sum_{j=1}^{L} \left(A_{ij}^T\right)^2}{\left(\sum_{j=1}^{L} A_{ij}^T\right)^2} \,. \tag{7.7}$$

The *Local Clustering Coefficient* is a measure of the transitivity of connections of individual nodes, that is, the likelihood that a is connected to c, given that a is connected to b

and b is connected to c. The local clustering coefficient is defined as

$$c_i^L \equiv \frac{[A^3]_{ii}}{\sum_{j\neq i,k\neq i} A_{ij}A_{ik}}\,. \tag{7.8}$$

One divides the total number of triangles in which node i is a vertex by the total number of connected triples centered on node i. Nodes with low local clustering correspond to students whose collaborators do not tend to collaborate with each other. Nodes with high local clustering correspond to students whose collaborators frequently collaborate with each other, such as in tight-knit study groups.

In a weighted network one can define a distance between any pair of nearest-neighbor nodes. For our analysis, we define the distance between nearest neighbors i and j to be the inverse of the weight connecting them

$$D_{ij} = \frac{1}{A_{ij}}\,. \tag{7.9}$$

If nodes i and j are not directly connected by a link then $D_{ij} = \infty$. This definition of the distance between nearest-neighbor nodes is then used to define the shortest-path distance between any two nodes d_{ij}. A path connecting node i to node j is a sequence of links along which one may walk to traverse the network from node i to node j when one walks along links in the direction of the link. The shortest-path distance between two nodes is the sum of the nearest-neighbor weights D_{ij} along the shortest path connecting two nodes, that is,

$$d_{ij} = \min_P \sum_{(l,k)\in P} D_{lk}\,, \tag{7.10}$$

where P is a path connecting node i to node j.

Closeness centrality is a measure of how close a node is on average to other nodes when one must travel along directed links in the direction of the link. Closeness centrality is defined as

$$c_i^C = \frac{n-1}{|A|-1}\frac{1}{\sum_{j\neq i} d_{ij}}, \tag{7.11}$$

where n is the number of nodes reachable from node i, and $|A|$ is the number of nodes in the network defined by the adjacency matrix A[62, 64]. Reachable means that one can travel

from node i to node j by walking along links in the direction of the link. Any nodes that are not reachable from node i are neglected in the sum of Eq. (7.11). In the context of social networks, closeness centrality can be thought of as a measure of independence as described in [64]. This is because a node with a large closeness centrality does not have to rely on other nodes to transmit messages across the network [64]. In the context of student collaboration networks closeness centrality is a measure of both the frequency with which a student assists others and how widely a student collaborates.

Harmonic centrality is also a measure of how close a node is to other nodes in the network when one must travel along directed links in the direction of the link. Harmonic centrality is defined as

$$c_i^H = \sum_{j \neq i} \frac{1}{d_{ij}}, \tag{7.12}$$

where $d(i, j)$ is the shortest path distance from node i to j [62, 65]. Harmonic centrality has a similar definition to closeness centrality, both being defined in terms of the inverse distances between nodes. The intuition for the two measures is the same. Nodes that are close to other nodes are more central as measured by closeness centrality and harmonic centrality. However, when computing harmonic centrality, if node j is not reachable from node i, the distance between the two nodes is set to $d_{ij} = \infty$. The corresponding term in the sum is then set to zero, $1/d_{ij} = 1/\infty \equiv 0$. This may be preferable to the procedure used to calculate closeness centrality as this procedure has been shown to introduce a bias towards nodes in small components [65].

Betweenness centrality is measure of how important a node is as a go-between for message transmission between nodes in a network, assuming that information travels along paths of shortest distance[3]. Betweenness centrality is defined as

$$c_i^B = \sum_{j,k \in V} \frac{\sigma(j, k|i)}{\sigma(j, k)}, \tag{7.13}$$

where $\sigma(j, k|i)$ is the number of shortest paths from node j to node k that pass through node i and where $\sigma(j, k)$ is the number of shortest paths from node j to node k [62, 67]. Nodes with

high betweenness centrality correspond to students with the most control over information transfer throughout the network. Therefore, the weight of the links in our networks do not modify betweenness centrality directly, but only indirectly through the path lengths they contribute to.

7.5 Results

We now correlate each measure with students' homework assignment or exam scores. Note that before computing correlations we first drop from our data set any students that missed an exam, did not submit a numerical assignment, or did not submit more than 2 analytical homework assignments. Such students typically correspond to students that dropped the course. In Fig. Fig. 7.3 we display the results of these calculations.

The error bars of our measures indicate a 95% confidence level and are calculated via bootstrap resampling with 10,000 resamplings of each correlation coefficient [105]. Most measures correlate with analytical homework grades at about the same level to within error for all courses as shown in Fig. Fig. 7.3. One consequence of this is that both out-strength and in-strength have statistically compatible correlations with homework grades. Therefore, getting and receiving help both correlate with improved performance equally well within our measurement resolution. While many measures correlate with homework grades, in both quantum mechanics and electromagnetism we find that only the net out-strength correlates with exam grades. Thus collaborative benefits to grades appear to be limited to homework. The exception is that students that help more frequently than they are helped perform well on exams. While most measures correlate with grades, there are important exceptions. For example, in-disparity does not correlate with analytical homework grades for any of our courses. Thus receiving assistance from a subset of your collaborators more frequently than others does not improve your grades. This adds nuance to the correlations of closeness centrality, harmonic centrality, and out and in strength with analytical homework grade which all suggest the maxim: collaborate widely and collaborate often. We also find that betweenness centrality has weaker correlations with analytical homework grades than many

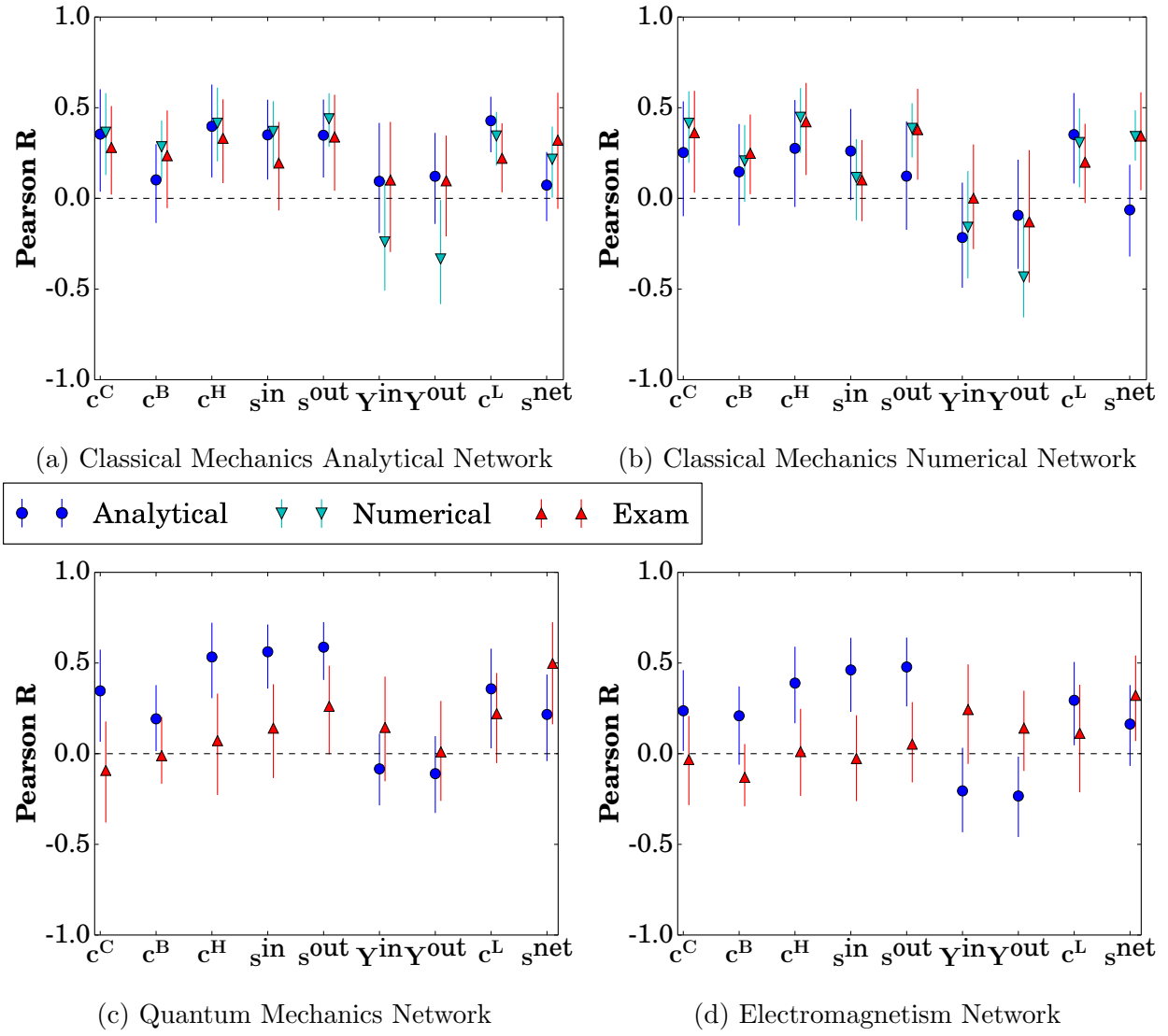

(a) Classical Mechanics Analytical Network

(b) Classical Mechanics Numerical Network

(c) Quantum Mechanics Network

(d) Electromagnetism Network

Fig. 7.3: *Correlation of nodal centrality measures with student grades in three upper level physics courses.* Correlation of complex network measures with student grades for three courses: classical mechanics, quantum mechanics, and electromagnetism. Correlations are shown with 95% confidence intervals as 95% confidence intervals are the standard for statistical quantities in social network analysis [101, 102, 103, 104]. Measures whose confidence intervals do not overlap with zero are considered to correlate with student grade. Most complex network measures correlate equally well with homework grades within their confidence intervals. In both quantum mechanics and electromagnetism, only the net out-strength correlates with exam grades. Students that help more than they are helped perform better on exams.

other measures. In contrast to other nodal centrality measures, betweenness is a more passive measure of the importance of a node to the network. That is, a student has high betweenness centrality from their ability to control the flow of information between other students. This suggests that students that are more actively engaged in the collaborative process achieve higher grades. In contrast, students that are not actively seeking out their collaboration with other students, and mostly function as a go-between, will not achieve higher grades.

Going beyond cases of non-correlation, we also quantify the differences in the correlation of out-strength with the correlations of clustering coefficient for both analytical and numerical assignments in classical mechanics. Of the analytical network centrality measures, clustering coefficient seems to correlate best with analytical homework grades. While amongst numerical network centrality measures, out-strength correlates well with numerical homework grades. However, we find the differences in the correlation of out-strength and clustering coefficient in both the numerical and the analytical cases are statistically compatible with zero. So, while it is tempting to draw further conclusions from the differences in correlation between network measure, we find that these differences are not statistically significant.

In our study, we have two simultaneous networks composed of the same students: the analytical and numerical networks for classical mechanics. We take advantage of this by correlating the centrality measures between the two networks, student to student. This allows us to quantify the stability of the roles taken by students in response to different types of homework assignments. We find that essentially all centrality measures correlate between the two types of network. Thus the students engaged in one collaboration network tend to be the same students that are engaged in another collaboration network, independent of assignment type.

Finally, in Fig. Fig. 7.4 we summarize the performance trajectories of students in both grades and collaboration strategy, specifically between low and high grades, and low and high out-strength between the Fall and Spring semesters, over what is for most participants

their junior year. A student with high out-strength (grades) is taken as at or above the median out-strength (grades). Students with low out-strength (grades) are students below the median. For our study this results in slightly more students with high out-strength (grades) than low out-strength (grades). This allows us to separate each course into four groups: group I has high grades and high out-strength; group II has high grades but low out-strength; group III has low grades and low out-strength; and group IV has low grades but high out-strength. We study the transitions of students between these groups from fall 2012 enrollment in classical mechanics to spring 2013 in electromagnetism and quantum mechanics. We compute transitions for both analytical homework grades and exam grades.

We emphasize that the diagrams describing the transition to electromagnetism only pertain to the students enrolled in both electromagnetism and classical mechanics. Similarly the diagrams describing the transition from classical mechanics to quantum mechanics only pertain to the students enrolled in both classical mechanics and quantum mechanics. First, we note that groups I and III, computed for analytical grades, start with more students than groups II and IV. For example, group I starts with 17 students for the network pertaining to students in common with electromagnetism and 15 students for quantum mechanics. In comparison, group IV starts with only 10 students in electromagnetism and 8 students in quantum mechanics. This reinforces our findings that out-strength correlates with student homework grade. These groups also exhibit the most common transition we observe, namely students who help many others and have high grades will continue to help many other and have high grades in future semesters. For example, 15 of the 17 students that start with high grades and high out-strength in classical mechanics maintain both in their transition to electromagnetism, we highlight this dominant transition by a blue arrow in Fig. 7.4(a). Depressingly, we also find that students who do not help many others and have low homework grades often maintain low homework grades and still help few in future semesters. We highlight the self-transitions of groups I and III in other diagrams as they are consistently greater than the self transitions observed in groups II and IV. For example, 9 of the 13

students that start in group III in classical mechanics remain in this group in quantum mechanics. Next, for exams, we observe that while many students start in groups I and III in classical mechanics, 15 for students in common with electromagnetism and 17 for students in commmon with quantum, 8 transition away in students' transition to electromagnetism and 9 transition away in quantum mechanics. This contrasts with the transitions for analytical assignments where 15 of the 18 students in group I remain their in transition to electromagnetism and 12 of the 15 students in group I remain their in their transition to quantum mechanics. helping to explain the differences in the level of correlations observed in classical mechanics vs. quantum mechanics and electromagnetism.

Finally, considering the four transition networks in aggregate, the most consistent transition we observe between groups is the transition between groups III and II. When base-lined against the transition from IV to I, we find that students more often make the transition from III to II. We highlight this finding by the blue coloring of the arrows from groups III to II in our diagrams. For example, in transitioning from classical mechanics to electromagnetism, 7 students transition from group III to group II, while only 2 students transition from group IV to group I. Consistently helping few others seems to facilitate the transition from low to high grades between semesters, as opposed to helping many others when one has low grades. Combining this result with the consistent self-transitions of group I suggests that those we help provide us with an inertia: helping many others when one has high grades results in one maintaining high grades. Helping few others when one has low grades allows one to make the transition to high grades. Such conclusions are preliminary due to the statistics, < 18 for groups I-IV. The trajectory of collaboration strategy presents an excellent avenue of future research to further refine our results. Additonally, the variable group size across groups makes it difficult to establish meanigful baselines for our transitions.

For each of the networks studied in Fig. Fig. 7.3 we also computed principal components of our network measures and correlated these with student grades. However, we found that these did not correlate any better with student grade than the out-strength centrality. It

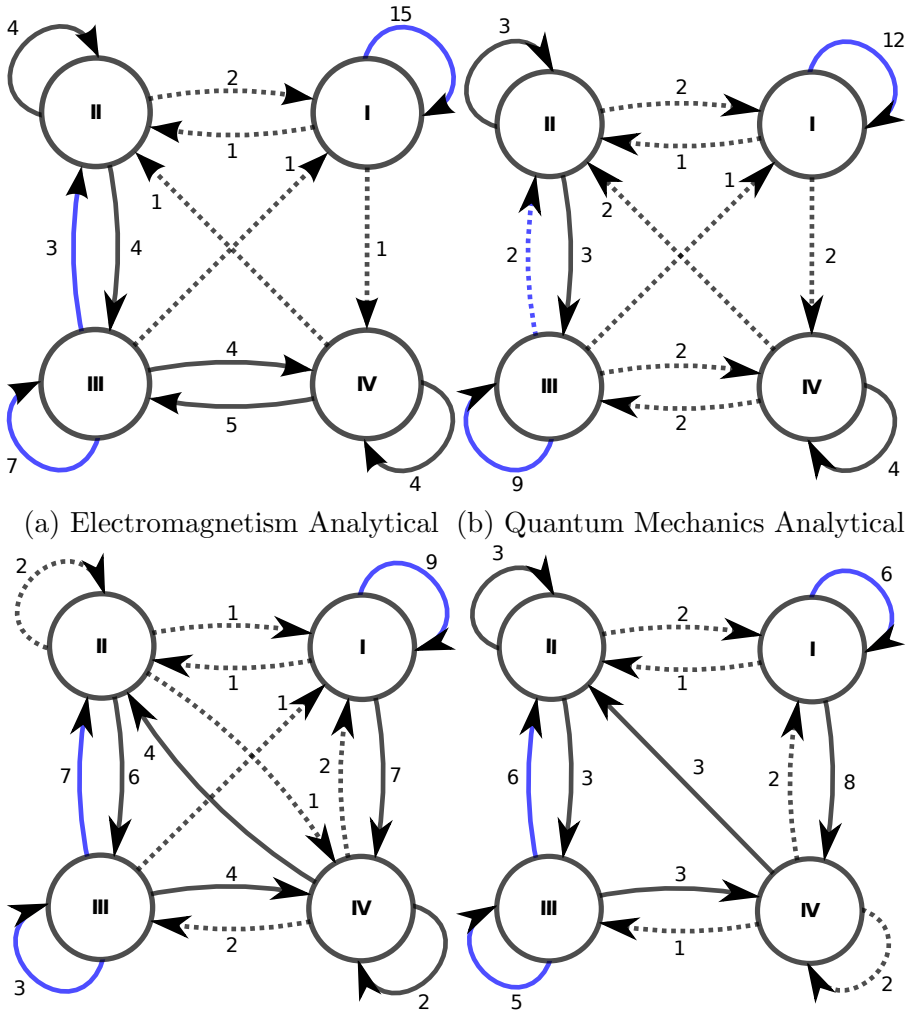

(a) Electromagnetism Analytical (b) Quantum Mechanics Analytical

(c) Electromagnetism Exam (d) Quantum Mechanics Exam

Fig. 7.4: *Changes in student grade and collaboration between semesters.* Students in classical mechanics fall into four groups: group I has high grades and high out-strength; group II has high grades but low out-strength; group III has low grades and low out-strength; and group IV has low grades and high out-strength. Arrows are transitions between groups from Fall 2012 to Spring 2013. Numbers indicate how many students transition between groups. Transitions of only 1 or 2 students have dashed arrows. Most students start in groups I and III, and remain there between semesters. We emphasize the self transitions of these groups by blue coloring because they always occur more often than the self transitions of groups II and IV. We highlight the fact that students consistently transition from low out-strength to high grades at constant out-strength more often than students with high out-strength by blue arrows from III to II in each diagram. Improved grades do not require changes to collaboration strategies.

is important to note that although network centrality measures correlate well with student grade this does not imply that the role students play in collaboration networks causes students to have higher grades. For example, it is not clear if helping many other students improves a student's grades, or if students who get good grades are more likely to be asked for or offer their assistance.

7.6 Conclusion

We find that while many nodal centrality measures correlate with student grades, not all do. The general picture painted by harmonic centrality, closeness centrality, and in/out strength is that is is important to collaborate widely, and to collaborate often. The non-correlation of disparity and betweenness centrality adds nuance to our understanding of student collaboration networks. A student must be actively engaged with the collaboration network in order to see benefits to their grades, and not just serve as a go-between for homework help. Our study of the grade and out-strength transition of students between semesters suggests there may be an inertia inherent in helping other students: those who help many and have high grades maintain high grades. In contrast, if a student has low grades, it is more beneficial to consistently help few others in order to transition to high grades. However, the transitions often only consist of a few students, and so these results could be due to fluctuations. The most clear trend in our data is that while many nodal centrality measures correlate well with homework grades, the benefits of collaboration do not extend to exams. In both quantum mechanics and electromagnetism we find the only measure that correlates with exam grades is the net out-strength of a student. Students who help more than they are helped do well on exams. Overall, our analysis suggests that students should be encouraged to actively collaborate with other students on homework assignments, and not passively occupy a position in the network.

7.7 Acknowledgments

The authors acknowledge the efforts of Esteban Chavez for developing the code that sorted reporting discrepancies in the survey data we collected. Esteban Chavez was funded under the NSF grant 0836937. We would also like to thank Pat Kohl for his logistical efforts, PER-related advisement, and general support. We would like to thank both Pat Kohl and Mark Lusk, for sharing course data with us. Lastly we would like to thank all of the students that participated in our study.

CHAPTER 8

SUMMARY AND OUTLOOK

In this chapter we summarize the results of our studies of connectivity in quantum phase transitions, quantum cellular automata, and student collaboration networks. We also discuss future research directions for each. Our work has taken a first step towards establishing a quantitative theory of quantum complexity. Via complex network analysis of quantum mutual information we were able to reproduce known properties of quantum statics, quantify the complexity of quantum cellular automata, and identify the complexity-generating Goldilocks rule 4. Such analysis goes beyond near-equilibrium quantum dynamics by identifying robust dynamical features like the quantum blinker. Our analysis of student collaboration networks revealed that some of the same network measures capable of identifying emergent features in quantum systems when applied to quantum mutual information networks also correlate with student grade when applied to student collaboration networks. Overall, our work on quantum complexity not only provides a new theoretical tool for fundamental physics, but also acts as a bridge between fundamental physics and complex systems research.

8.1 Connectivity in Quantum Phase Transitions, Quantum Cellular Automata, and Student Collaboration Networks

In Chapter 4 we studied three quantum phase transitions, identifying critical points and boundaries via complex network analysis of quantum mutual information complex networks. We found that the ferromagnetic phase is characterized by networks with high network density, high clustering, and low disparity. In the paramagnetic phase, as the ground state approaches a product state, we found that disparity increases while network density and clustering decrease. At the critical point of the transverse Ising model and the Berezinskii-Kosterlitz-Thouless (BKT) transition point of the Bose-Hubbard model we found that our complex network measures took on intermediate values between the extremes of either phase.

This suggests that quantum mutual information networks are most complex near criticality as the ground states of either model are well characterized in the strong and weak coupling limits ($g, (J/U) \ll 1$, and $g, (J/U) \gg 1$). We found that the first derivative, second derivative, and other features, of network density, clustering coefficient, disparity, and Pearson R correlation show systematic finite size scaling towards the critical points of the transverse Ising and Bose-Hubbard models. Using Open Source Matrix Product States (OpenMPS) [49] we were able to simulate lattices of hundreds of qubits, allowing us to verify the critical point of the transverse Ising model to within 0.001% of its known value. Furthermore, we found that complex network analysis could identify the Berezinskii-Kosterlitz-Thouless critical point of the Bose-Hubbard to within 3.6% of its accepted value. Finally, we found that by extremizing complex network quantities we could identify the Mott lobe separating the Mott Insulator phase from a superfluid phase in the Bose-Hubbard model. This was a proof of principle study quantifying the ability of complex network analysis of quantum mutual information networks to reproduce known quantum statics. Our complex network approach performs better than methods based on the Bethe ansatz [106], the Luttinger liquid parameter [107], fidelity [108], and 3rd order perturbation theory [109]. Thus Chapter 4 was a step in developing tools that go beyond the analysis of the near-equilibrium quantum dynamics of the Kibble-Zurek mechanism [110]. In Chapters 5 and 6 we applied these tools to non-equilibrium quantum dynamics.

In Chapter 5 we performed a convergence study of the quantum many body dynamics generated by the Bleh, Calarco, Montangero (BCM) Hamiltonian. We evolved hundreds of random Fock state initial conditions and local-defect initial conditions under this Hamiltonian using one of the latest time evolution methods for OpenMPS [57]. We found that OpenMPS was not able to compute converged estimates of quantum states for any of the initial conditions studied according to the internal convergence parameters $\chi_{\max}$ and ϵ. We found that $\chi_{\max}$ was quickly saturated for all simulations due to the rapid growth of entanglement, even for lattices with as few as 26 qubits. Since after saturation of $\chi_{\max}$ we no longer

have a converged estimate of the quantum state this represents the failure of OpenMPS to accurately simulate the dynamics of the BCM Hamiltonian. We also studied the effect of less stringent convergence criteria on the saturation of $\chi_{\max}$ by increasing ϵ. We found that while increasing ϵ does lead to simulations that do not saturate $\chi_{\max}$ the OpenMPS estimates of complex network quantities become unreliable. After our convergence study of the BCM Hamiltonian we compared our simulation results to the simulations reported in the paper defining the BCM Hamiltonian [40]. Specifically, in [40] a quantum blinker pattern was reported in the dynamics of $\langle \hat{n}_i \rangle$. Such emergent features are important because they indicate that the BCM Hamiltonian can generate complex dynamics. We found that our simulation results do not agree with the results reported in [40]; specifically, we did not observe a quantum blinker pattern for the initial condition specified in [40]. We noted that while the blinker initial condition specified in [40] is symmetric, the resulting dynamics of the figure in [40] are asymmetric. This contrasts with our results that maintain left-right symmetry over much longer time scales. We then simulated the BCM blinker initial condition using a Trotter-based time evolution method on a lattice of 20 qubits and still did not observe a quantum blinker pattern. We concluded that the original BCM paper is in error, the initial condition specified in [40] does not produce a quantum blinker. Although this initial condition does not produce a quantum blinker, the qualitative idea in [40] is correct: we did find an initial condition that does and termed it the blinker initial condition, $|B\rangle$. For the blinker initial condition we found that OpenMPS is able to reliably converge network density, clustering coefficient, and disparity to the results of our Trotter-based evolution scheme. However, OpenMPS was unable to converge the central bond entropy of that blinker initial condition. Despite OpenMPS not accurately converging the central bond entropy of the blinker initial condition it did accurately compute the amplitude and frequency of fluctuations of the central bond entropy. This suggested that OpenMPS is able to compute the complexity of quantum many body dynamics of local objects like blinkers, but not the entanglement. Finally, we performed a case study of a Hamiltonian motivated by rule 6 of [45].

We found that OpenMPS was able to accurately compute both the central bond entropy and complex network measures for the blinker initial condition evolved under this Hamiltonian. The results on the blinker initial condition evolved under the BCM Hamiltonian and the rule 6 Hamiltonian suggest that the dynamics of a few Hamiltonian-based quantum cellular automata (QCA) can be efficiently simulated with OpenMPS while the dynamics of most others cannot. Hamiltonian-based QCA that generate too much entanglement cannot be efficiently simulated in OpenMPS because they abruptly saturate $\chi_{\max}$. These results thus motivated the scaling study of the late-time entanglement properties of Hamiltonian-based QCA performed in Chapter 6.

In Chapter 6 we studied the entanglement and complexity generated by 13 Hamiltonian-based quantum cellular automata defined in (6.1)-(6.13) with $b_i+b_i^\dagger$ as the main operator. We quantified the complexity of their dynamics in terms of persistent fluctuations of the central bond entropy, network measures far from their values for random/well known quantum states, and significant peaks in the power spectra of the central bond entropy. We found that rules 4, 12, and 28 exhibit robust dynamical features in the dynamics of $\langle \hat{n}_i \rangle$, specifically quantum blinkers. The quantum blinker of rule 4 can be considered robust if one considers rules 12 and 28 as perturbations of this rule, since the blinker pattern still appears in the dynamics of these rules. Next we found that rules 10, 17, and 21 produced many peaks above the red noise threshold for all measures. We also noted that rules 2, 3, 4, 6, and 23 produced many significant peaks for complex network measures. We found that rules 2, 4, 6, 10, 17, and 21 produced more significant peaks in the central bond entropy than all other rules. Interestingly rules 12 and 28 do not have many significant peaks in the the power spectra of entanglement or complexity measures. This may be due to the exact periodicity of the blinker dominating the power spectrum. As discussed in [87], such exact periodicities can reduce the effectiveness of the red noise fit at other frequencies. We found that rules 2, 4, 10, 12, 21, and 28 produce persistent fluctuations in the central bond entropy for almost all initial conditions as quantified by the number of simulations with fluctuations above levels

consistent with a random initial condition. Rules 2 and 4 produced particularly persistent fluctuations of the central bond entropy, with $S_{\text{bond}} \approx 10^{-2}$ for many initial conditions. We found that our Hamiltonian-based QCA typically generate highly entangled quantum states with quantum mutual information networks that are not structured like random or well-characterized quantum states. However, the Goldilocks rule 4 and non-Goldilocks rule 17 had exceptions to this typical behavior. Both rules generated quantum states with late-time central bond entropy independent of system size for at least one initial condition. From all of these different analyses it became clear that rule 4 best met all of our criteria for a complexity generating rule. We illustrate which criteria for complexity each rule meet in the Venn diagram presented in Fig. 8.1. This rule exhibited a robust dynamical feature, had

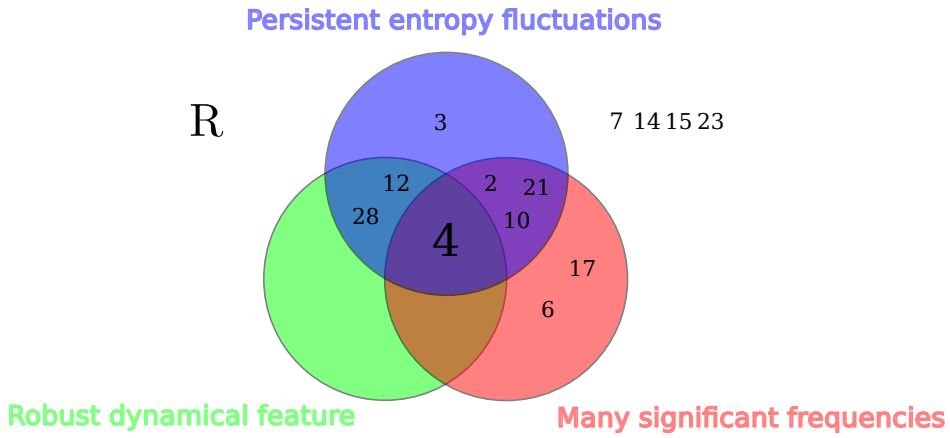

Fig. 8.1: *Criteria for complexity generating rules.* All rules generate quantum states with complex network measures far from their values for random quantum states. Rule 4 best meets the three other criteria for a complexity generating rule. It has a robust dynamical feature, persistent entropy fluctuations, and these entropy fluctuations have many significant frequencies.

persistent fluctuations in the central bond entropy, and had many significant peaks in the power spectra of the central bond entropy. Since rule 4 is a Goldilocks rule we confirmed that only Goldilocks rules are complexity generating for the initial conditions we have studied. Furthermore, of the 8 non-Goldilocks rules we have studied we find that 6 of them, rules 3, 7, 10, 15, 21, and 23, display significantly reduced fluctuations of the central bond entropy for all initial conditions. Therefore, our hypothesis on non-Goldilocks rules also appears to

be correct: non-Goldilocks rules tend toward thermalization.

While almost all of the quantum states generated by our automata have are highly entangled, for a few initial conditions rules 4 and 17 generate lowly entangled quantum states. These states were lowly entangled but still had complex structure in their quantum mutual information networks. We found that the highly entangled states generically produced by our automata also had complex network structure. While we have very little data for lowly entangled quantum states, it appears that a feature of classical complexity, complex network structure, may exist in quantum systems across a range of entanglement. By quantifying the relationship between complexity and entanglement we begin to understand what forms of quantum complexity are accessible by classical simulation methods like tensor networks and what forms are only accessible with a quantum computer. Since our Hamiltonian-based QCA typically generate highly entangled quantum states, most Hamiltonian-based quantum cellular automata can not be simulated with Open Source Matrix Product States for the initial conditions we have studied and would require a quantum computer to simulate them.

We concluded Chapter 6 with a case study of the emergent quantum blinker pattern of rule 12. Our case study of the quantum blinker pattern revealed that the entanglement produced by quantum cellular automata can be tuned by the slope of a linear perturbation. We also found that the late-time bond entropy is maximized for a particular value of the perturbing slope and that this value decreases as a function of system size. We studied two blinker initial conditions and found that we could tune the level of entanglement and complexity of our simulations via the initial distance between blinkers and determined the effective size of blinkers to be about 7 sites.

In Chapter 7 we studied the homework collaboration networks of students enrolled in three courses at the Colorado School of Mines: classical mechanics, quantum mechanics, and electromagnetism. We began our complex network analysis by correlating nodal measures with homework and exam grades and found that most nodal centrality measures correlate with students homework grades in these three courses. Measures like out-strength, close-

ness centrality, and harmonic centrality quantified the importance of collaborating widely and collaborating often on homework. Students that did so did well on homework. Not all measures we studied correlated with grades. The lack of correlation of betweenness centrality and in-disparity helped us understand the importance of being actively engaged in the collaboration network. It is not enough to simply occupy an important position in the collaboration network; successful students actively collaborate widely across the collaboration network. Interestingly, we found that the benefits collaboration brings to student grades on homework assignments do not transfer to exams, where students do not have their collaborators available to them. The only measure that we found correlates with exam grades in electromagnetism and quantum mechanics was out-strength. Students who help more than they are helped perform well on exams. Comparing the networks formed from the collaboration of students on different types of homework assignments we found most measures correlate student to student between such networks. This suggests that students adopt similar collaboration strategies in response to different types of assignments. Finally, our analysis of the change in student collaboration strategies between semesters drew more limited conclusions, due to the sparse statistics of our data set, once divided into groups of high and low grades and high and low out-strength. Our most certain finding is that students who help many others and have high grades will tend to continue to help many others and have high grades. Similarly, those who have low grades and who help few others will continue to in future semesters. In summary, our analysis of student collaboration networks suggests students should actively collaborate with other students on homework assignments instead of passively occupying a position in the network.

In Chapter 7 we correlated nodal centrality measures computed on student collaboration networks with student course performance for students enrolled in three courses: classical mechanics, quantum mechanics, and electromagnetism. We found that out-strength was consistently the best performing network measure, correlating best with student grades in all 3 courses. Students who collaborate widely have higher grades. We also found that both

the in-strength and local clustering coefficient correlate well with student grades in all three courses. We find that although harmonic centrality and closeness centrality have very similar definitions, only closeness centrality correlates well with student grades on numerical assignments and therefore suggest that the local clustering coefficient is the more reliable meaure, even though closeness centrality sometimes outperforms the local clustering coefficient. We also correlated student grades with principal components of our complex network measures, however we found that these did not correlate as well with student grades as out-strength. Finally, while our analysis does not imply that the collaborations of a student cause them to have higher grades, we have demonstrated that collaboration is an important part of the educational process. Course designers may consider conducting surveys of student programming experience in physics courses emphasizing numerical methods. Instructors could then consult with students with prior programming experience to learn about and clarify the misconceptions of other students. Instructors can also emphasize our results on clustering in the syllabi of their courses, encouraging students to join collaboration groups, as we have shown that being in a clustered region of student collaboration networks correlates with having good grades.

8.2 Future Work: Complex Networks in Quantum Information, Quantum Many Body Dynamics, and Student Collaboration Networks

In this section we offer directions for future research for quantum mutual information complex networks, quantum cellular automata, and student collaboration networks. Our proposed directions for future research of quantum mutual information complex networks explore the interface between complex network analysis and quantum information. In contrast, our future research directions for quantum cellular automata are focused on addressing the limitations of our study in chapter 6. Finally, our future research directions for student collaboration networks focus on extending the analysis of Chapter 7 with the existing data.

Future work studying quantum mutual information complex networks may consider using the measures defined in [111]. That work quantifies the importance of various weighted

network motifs that may be appear in weighted networks. A direction for future research on quantum mutual information networks is to study the space of three qubit quantum states. According to [112] almost all tripartite pure states are uniquely determined by their two site reduced density matrices. May complex network measures of quantum mutual information networks offer a useful parameterization of this space? As is noted in [113], three qubits can be entangled in two different ways. Can these different types of entanglement be distinguished via complex network analysis of quantum mutual information networks? Finally, in connection with quantum information theory it is interesting to observe that cluster states are parameterized by networks. Is there a simple connection between the network structure defining a cluster state and the network structure induced in its entanglement?

While we have confirmed that rule 4 best meets our criteria for a complexity generating rule other rules might have been classified as complexity generating if more initial conditions were considered. For instance rule 21 meets all the criteria for a complexity generating rule except that it does not exhibit a robust dynamical feature. Therefore a future research direction is to gather more statistics by studying many more initial conditions than the 13 considered in Chapter 6. This is a generic feature of complex systems: they have astronomically large probability spaces only a small fraction of which is ever explored. This work considered many different classes of initial conditions: random Fock states, local defects, singlets, singlet arrays, and cluster states. The cluster state evolved under rule 17 was notable for producing $\overline{S}_{\text{bond}}$ independent of system size with no obvious localization occurring in any local observable. In contrast to all other initial conditions studied this initial condition has equal probability of being in any state of the measurement basis. Using such states as initial conditions may produce less biased results in the dynamics of such automata since cluster states will not produce factorized dynamics for any rule. Since cluster states are known to have similar entanglement properties as the eigenstates of quantum many body Hamiltonians [114] they may be more natural states to study using OpenMPS.

In our study of the fluctuations of the central bond entropy at late times we quantified the fluctuations of a typical random quantum state by averaging over the late-time fluctuations produced by each of our Hamiltonians for a single random initial condition. A more thorough study may consider averaging over the late-time fluctuations produced by many random initial conditions. In our study of late-time values of complex network measures we quantified randomness in terms of the values of our measures computed on random quantum states. However, there are other definitions of randomness. For instance, instead of generating random quantum states by generating random coefficients, one could evolve each initial condition under a set of random Hermitian operators as the main operator of a QCA. Therefore a future study may consider quantifying randomness by replacing the $\hat{b}_i + \hat{b}_i^\dagger$ term in our quantum cellular automata with a random Hermitian operator. Another direction to consider for future research is to evaluate the sensitivity of OpenMPS to perturbations in the definition of quantum cellular automata, for instance multiplying the rule operators by non-binary coefficients.

In our Fourier analysis we found that rules with exact periodicities like the quantum blinker have power spectra that are dominated by a single frequency, impairing the effectiveness of the red noise fit. In [87] a "pre-whitening" procedure is mentioned as a means of addressing such dominant frequencies of power spectra. Future work may consider employing such a procedure to improve the quality of the red-noise analysis of QCA. Finally, even in simulations without dominant frequencies the simulation may be generating white noise. Thus another important procedure to implement is to test simulations against a white noise null hypothesis.

Finally, the long term logarithmic growth of the central bond entropy establishes a connection between Hamiltonian-based quantum cellular automata and many body localization [89]. We only observed long-term logarithmic growth of the central bond entropy for the blinker initial condition evolved under the rule 12 Hamiltonian. This suggests that many body localization may be rare for Hamiltonian-based QCA. A future study could explore the

conditions under which many body localization occurs in Hamiltonian-based QCA. That is, what combination of rules and initial conditions gives rise to many body localization? The blinker like structures we observe are not likely due to the integrability of our systems as they do not have any obvious conserved quantities. However, future studies may consider studying the integrability of quantum cellular automata.

In Chapter 7 we analyzed weighted networks that summarized the collaboration of students over an entire semester of homework assignments. We have data for each homework assignment individually. Therefore one future direction for research is to study how students collaboration habits evolve between assignments and semesters. Do students choose their collaborators based on course performance? Another direction for study is to quantify the correlation between student course performance and the performance of their closest peers, that is, do collaborators of students that perform well also tend to perform well as quantified by student grades?

REFERENCES CITED

[1] M. Gell-Mann and S. Lloyd. Information measures, effective complexity, and total information. *Complexity*, 2:44, 1996.

[2] J. A. Dunne, R. J. Williams, and N. D. Martinez. Network structure and biodiversity loss in food webs: Robustness increases with connectance. *Ecology Letters*, 5:558, 2002.

[3] M. E. J. Newman. *Networks: An Introduction*. Oxford University Press, Inc., New York, 2010.

[4] M. E. J. Newman. The structure and function of complex networks. *SIAM Review*, 45:167, 2003.

[5] D. Chu, R. Strand, and R. Fjelland. Theories of complexity: Common denominators of complex systems. *Complexity*, 8:19, 2003.

[6] *The National Academies Keck Futures Initiative: Complex Systems: Task Group Summaries*. The National Academies Press, Washington, D.C., 2009.

[7] R. Albert and A.-L. Barabási. Statistical mechanics of complex networks. *Reviews of Modern Physics*, 74:47, 2002.

[8] L. D. Carr, D. Demille, R. V. Krems, and J. Ye. Cold and ultracold molecules: Science, technology, and applications. *New Journal of Physics*, 11:055049, 2009.

[9] R. Blatt and C. F. Roos. Quantum simulations with trapped ions. *Nature Physics*, 8:277, 2012.

[10] R. Loew, H. Weimer, J. Nipper, J. B. Balewski, B. Butscher, H. P. Buechler, and T. Pfau. An experimental and theoretical guide to strongly interacting Rydberg gases. *Journal of Physics B-Atomic Molecular and Optical Physics*, 45, 2012.

[11] H. J. Kimble. The quantum internet. *Nature*, 453:1023, 2008.

[12] P. Grassberger. Toward a quantitative theory of self-generated complexity. *International Journal of Theoretical Physics*, 25:907, 1986.

[13] D. J. Watts and S. H. Strogatz. Collective dynamics of 'small-world' networks. *Nature*, 393:440, 1998.

[14] E. Almaas, B. Kovács, T. Vicsek, Z. N. Oltvai, and A.-L. Barabási. Global organization of metabolic fluxes in the bacterium Escherichia coli. *Nature*, 427:839, 2004.

[15] G. Bianconi. Superconductor-insulator transition on annealed complex networks. *Physical Review E - Statistical, Nonlinear, and Soft Matter Physics*, 85:1, 2012.

[16] S. Perseguers, M. Lewenstein, A. Acín, and J. I. Cirac. Quantum complex networks. *Nature Physics*, 6:539, 2010.

[17] S. Perseguers, G. J. Lapeyre, D. Cavalcanti, M. Lewenstein, and A. Acín. Distribution of entanglement in large-scale quantum networks. *Reports on Progress in Physics*, 76:096001, 2013.

[18] M. Cuquet and J. Calsamiglia. Entanglement percolation in complex quantum networks. *Physical Review Letters*, 103:240503, 2009.

[19] C.-P. Chou and M.-C. Chung. Network topology: Detecting topological phase transitions in the Kitaev chain and the rotor plane. *ArXiv e-prints*. arXiv:1308.0255v6, 2014.

[20] H. Yi and M.-S. Choi. Effect of quantum fluctuations in an Ising system on small-world networks. *Physical Review E*, 67:056125, 2003.

[21] A. Halu, L. Ferretti, A. Vezzani, and G. Bianconi. Phase diagram of the Bose-Hubbard model on complex networks. *EPL*, 99:18001, 2012.

[22] A. Halu, S. Garnerone, A. Vezzani, and G. Bianconi. Phase transition of light on complex quantum networks. *Physical Review E*, 87:1, 2013.

[23] B. Groisman, S. Popescu, and A. Winter. Quantum, classical, and total amount of correlations in a quantum state. *Physical Review A*, 72:032317, 2005.

[24] M. M. Wolf, F. Verstraete, M. B. Hastings, and J. I. Cirac. Area laws in quantum systems: Mutual information and correlations. *Physical Review Letters*, 100:070502, 2008.

[25] E. Bullmore and O. Sporns. Complex brain networks: Graph theoretical analysis of structural and functional systems. *Neuroscience*, 10:186, 2009.

[26] J. P. Crutchfield. Between order and chaos. *Nature Physics*, 8:17, 2011.

[27] C. G. Langton. Computation at the edge of chaos: Phase transitions and emergent computation. *Physica D: Nonlinear Phenomena*, 42:12, 1990.

[28] L. D. Carr and B. L. Lev. An arrested implosion. *Physics*, 9:55, 2016.

[29] M. Lewenstein, A. Sanpera, V. Ahufinger, B. Damski, A. Sen De, and U. Sen. Ultracold atomic gases in optical lattices: Mimicking condensed matter physics and beyond. *Advances in Physics*, 56:243, 2007.

[30] J. W. Britton, B. C. Sawyer, A. C. Keith, C. C. J. Wang, J. K. Freericks, H. Uys, M. J. Biercuk, and J. J. Bollinger. Engineered two-dimensional Ising interactions in a trapped-ion quantum simulator with hundreds of spins. *Nature*, 484:489, 2012.

[31] B. Yan, S. A. Moses, B. Gadway, J. P. Covey, K. R. A. Hazzard, A. M. Rey, D. S. Jin, and J. Ye. Observation of dipolar spin-exchange interactions with lattice-confined polar molecules. *Nature*, 501:521, 2013.

[32] R. Coldea, D. A. Tennant, E. M. Wheeler, E. Wawrzynska, D. Prabhakaran, M. Telling, K. Habicht, P. Smeibidl, and K. Kiefer. Quantum criticality in an Ising chain: Experimental evidence for emergent E8 symmetry. *Science*, 327:177, 2010.

[33] I. Bloch. Ultracold quantum gases in optical lattices. *Nature Physics*, 1:23, 2005.

[34] S. Sachdev. *Quantum Phase Transitions*. Cambridge University Press, New York, 2011.

[35] M. Greiner, O. Mandel, T. Esslinger, T. W. Hänsch, and I. Bloch. Quantum phase transition from a superfluid to a Mott insulator in a gas of ultracold atoms. *Nature*, 415:39, 2002.

[36] A. Osterloh, L. Amico, G. Falci, and R. Fazio. Scaling of entanglement close to a quantum phase transition. *Nature*, 416:608, 2002.

[37] T. J. Osborne and M. A. Nielsen. Entanglement in a simple quantum phase transition. *Physical Review A*, 66:032110, 2002.

[38] A. Anfossi, P. Giorda, A. Montorsi, and F. Traversa. Two-point versus multipartite entanglement in quantum phase transitions. *Physical Review Letters*, 95:056402, 2005.

[39] L. Amico, A. Osterloh, and V. Vedral. Entanglement in many-body systems. *Reviews of Modern Physics*, 80:517, 2008.

[40] D. Bleh, T. Calarco, and S. Montangero. Quantum game of life. *EPL*, 97, 2012.

[41] M. Gardner. The fantastic combinations of John Conway's new solitaire game life. *Scientific American*, 224:112, 1971.

[42] R. P. Feynman. Simulating physics with computers. *International Journal of Theoretical Physics*, 21:467, 1982.

[43] Andrew Adamatzky, editor. *Game of Life Cellular Automata*. Springer London, London, 2010.

[44] B. Chopard and M. Droz. *Cellular Automata Modeling of Physical Systems*. Collection Alea-Saclay: Monographs and Texts in Statistical Physics. Cambridge University Press, Cambridge, 1998.

[45] L. Hillberry. *Entanglement and complexity in quantum elementary cellular automata*. Master's thesis, Colorado School of Mines, 2016.

[46] U. Schollwoeck. The density-matrix renormalization group in the age of matrix product states. *Annals of Physics*, 326:96, 2011.

[47] A. Adams, L. D. Carr, T. Schäfer, P. Steinberg, and J. E. Thomas. Strongly correlated quantum fluids: Ultracold quantum gases, quantum chromodynamic plasmas and holographic duality. *New Journal of Physics*, 14:115009, 2012.

[48] J. Eisert, M. Cramer, and M. B. Plenio. Colloquium: Area laws for the entanglement entropy. *Reviews of Modern Physics*, 82:277, 2010.

[49] M. L. Wall and L. D. Carr. Out of equilibrium dynamics with matrix product states. *New Journal of Physics*, 14:125015, 2012.

[50] J. Bruun and E. Brewe. Talking and learning physics: Predicting future grades from network measures and force concept inventory pretest scores. *Physical Review Special Topics - Physics Education Research*, 9:020109, 2013.

[51] T. M. Cover and J. A. Thomas. *Elements of Information Theory*. John Wiley & Sons, New York, 1991.

[52] E. Altman, E. Demler, and M. D. Lukin. Probing many-body states of ultracold atoms via noise correlations. *Physical Review A*, 70:013603, 2004.

[53] H. Ollivier and W. H. Zurek. Quantum discord: A measure of the quantumness of correlations. *Physical Review Letters*, 88:017901, 2002.

[54] J. Cardy. *Scaling and Renormalization in Statistical Physics*. Cambridge University Press, Cambridge, first edition, 1996.

[55] M. Vojta. Quantum phase transitions. *Reports on Progress in Physics*, 66:2069, 2003.

[56] S. Wolfram. Universality and complexity in cellular automata. *Physica D: Nonlinear Phenomena*, 10:1, 1984.

[57] M. P. Zaletel, R. S. K. Mong, C. Karrasch, J. E. Moore, and F. Pollmann. Time-evolving a matrix product state with long-ranged interactions. *Physical Review B*, 91:1, 2015.

[58] M. L. Wall, D. Jaschke, A. Dhar, A. Glick, D. Larue, K. Maeda, D. L. Vargas, and L. D. Carr. Matrix Product State Simulations. https://sourceforge.net/projects/openmps/.

[59] P. Calabrese and J. Cardy. Evolution of entanglement entropy in one-dimensional systems. *Journal of Statistical Mechanics: Theory and Experiment*, 2005:P04010, 2005.

[60] M. A. Nielsen and I. L. Chuang. *Quantum Computation and Quantum Information: 10th Anniversary Edition*. Cambridge University Press, New York, 10th edition, 2011.

[61] S. Boccaletti, V. Latora, Y. Moreno, M. Chavez, and D. Hwang. Complex networks: Structure and dynamics. *Physics Reports-Review Section of Physics Letters*, 424:175, 2006.

[62] A. H. Aric, A. S. Daniel, and J. S. Pieter. Exploring network structure, dynamics, and function using NetworkX. In *Proceedings of the 7th Python in Science Conference (SciPy2008)*, page 11, Pasadena, CA USA, 2008.

[63] S. E. Ahnert, D. Garlaschelli, T. M. A. Fink, and G. Caldarelli. Ensemble approach to the analysis of weighted networks. *Physical Review E*, 76:016101, 2007.

[64] L. C. Freeman. Centrality in social networks conceptual clarification. *Social Networks*, 1:215, 1979.

[65] P. Boldi and S. Vigna. Axioms for centrality. *Internet Mathematics*, 10:222, 2014.

[66] V. Latora and M. Marchiori. Efficient behavior of small-world networks. *Physical Review letters*, 87:198701, 2001.

[67] L. C. Freeman. A set of measures of centrality based on betweenness. *Sociometry*, 40:35, 1977.

[68] S. Van Der Walt, S. C. Colbert, and G. Varoquaux. The NumPy array: A structure for efficient numerical computation. *Computing in Science and Engineering*, 13:22, 2011.

[69] M. A. Nielsen. Cluster-state quantum computation. *Reports on Mathematical Physics*, 57:147, 2006.

[70] J. I. Cirac, P. Zoller, H. J. Kimble, and H. Mabuchi. Quantum state transfer and entanglement distribution among distant nodes in a quantum network. *Physical Review Letters*, 78:3221, 1997.

[71] M. Rigol. Scaling of the gap, fidelity susceptibility, and Bloch oscillations across the superfluid-to-Mott-insulator transition in the one-dimensional Bose-Hubbard model. *Physical Review A*, 87:043606, 2013.

[72] M. L. Wall. *Quantum Many Body Physics of Ultracold Molecules in Optical Lattices: Models and Simulation Methods*. PhD thesis, Colorado School of Mines, 2012. http://physics.mines.edu/lcarr/theses/wall_thesis_2012.pdf.

[73] L. D. Carr, M. L. Wall, D. G. Schirmer, R. C. Brown, J. E. Williams, and C. W. Clark. Mesoscopic effects in quantum phases of ultracold quantum gases in optical lattices. *Physical Review A*, 81:013613, 2010.

[74] V. Vedral. Quantifying entanglement in macroscopic systems. *Nature*, 453:1004, 2008.

[75] E. Jones, T. Oliphant, P. Peterson, et al. SciPy: Open source scientific tools for Python, 2001. http://www.scipy.org/.

[76] S. Ejima, H. Fehske, and F. Gebhard. Dynamic properties of the one-dimensional Bose-Hubbard model. *EPL*, 93:30002, 2011.

[77] P. Arrighi and J. Grattage. The quantum game of life. *Physics World*, 25:23, 2012.

[78] M. Rigol. Quantum quenches and thermalization in one-dimensional fermionic systems. *Physical Review A*, 80:053607, 2009.

[79] B. Pozsgay, M. Mestyán, M. A. Werner, M. Kormos, G. Zaránd, and G. Takács. Correlations after quantum quenches in the XXZ spin chain: Failure of the generalized Gibbs ensemble. *Physical Review Letters*, 113, 2014.

[80] M. Fagotti, M. Collura, F. H. L. Essler, and P. Calabrese. Relaxation after quantum quenches in the spin-$\frac{1}{2}$ Heisenberg XXZ chain. *Physical Review B*, 89:125101, 2014.

[81] S. R. Manmana, S. Wessel, R. M. Noack, and A. Muramatsu. Strongly correlated fermions after a quantum quench. *Physical Review Letters*, 98:210405, 2007.

[82] D. Rossini, A. Silva, G. Mussardo, and G. E. Santoro. Effective thermal dynamics following a quantum quench in a spin chain. *Physical Review Letters*, 102:127204, 2009.

[83] P. Barmettler, M. Punk, V. Gritsev, E. Demler, and E. Altman. Relaxation of antiferromagnetic order in spin-1/2 chains following a quantum quench. *Physical Review Letters*, 102:1, 2009.

[84] J. S. Caux and R. M. Konik. Constructing the generalized gibbs ensemble after a quantum quench. *Physical Review Letters*, 109:1, 2012.

[85] F. H. L. Essler, S. Evangelisti, and M. Fagotti. Dynamical correlations after a quantum quench. *Physical Review Letters*, 109:1, 2012.

[86] H. F. Song, S. Rachel, and K. Le Hur. General relation between entanglement and fluctuations in one dimension. *Physical Review B*, 82:012405, 2010.

[87] D. L. Gilman, F. J. Fuglister, and J. M. Mitchell. On the power spectrum of "red noise". *Journal of the Atmospheric Sciences*, 20:182, 1963.

[88] V. Letfus. Autocorrelation analysis of some solar indices. *Contributions of the Astronomical Observatory Skalnate Pleso*, 6:255, 1976.

[89] J. H. Bardarson, F. Pollmann, and J. E. Moore. Unbounded growth of entanglement in models of many-body localization. *Physical Review Letters*, 109:017202, 2012.

[90] L. C. McDermott and E. F. Redish. Resource letter: PER-1: Physics education research. *American Journal of Physics*, 67:755, 1999.

[91] L. C. McDermott. Research on conceptual understanding in mechanics. *Physics Today*, 37:24, 1984.

[92] A. Van Heuvelen. Learning to think like a physicist. *American Journal of Physics*, 59:891, 1991.

[93] F. Reif. Scientific approaches to science education. *Physics Today*, 39:48, 1986.

[94] E. F. Redish and R. N. Steinberg. Teaching physics: Figuring out what works. *Physics Today*, 52:24, 1999.

[95] S. P. Borgatti, A. Mehra, D. J. Brass, and G. Labianca. Network analysis in the social sciences. *Science*, 323:892, 2009.

[96] M. Bodin. Mapping university students' epistemic framing of computational physics using network analysis. *Physical Review Special Topics - Physics Education Research*, 8:010115, 2012.

[97] AIP Statistical Research Center. `http://www.aip.org/statistics`.

[98] Blackboard Inc. Blackboard. `http://www.blackboard.com`, (2013).

[99] D. Schmidt, A. Bridgeman, and P. Kohl. Student collaborative networks and academic performance. In *APS Meeting Abstracts*, 2013.

[100] D. Schmidt, A. Bridgeman, and P. Kohl. Student collaborative networks and academic performance in physics. In *PERC 2013*, 2013.

[101] G. Kossinets and D. J. Watts. Empirical analysis of an evolving social network. *Science*, 311:88, 2006.

[102] D. Centola. The spread of behavior in an online social network experiment. *Science*, 329:1194, 2010.

[103] P. S. Dodds, R. Muhamad, and D. J. Watts. An experimental study of search in global social networks. *Science*, 301:827, 2003.

[104] S. Aral and D. Walker. Identifying influential and susceptible members of social networks. *Science*, 337:337, 2012.

[105] L. Wasserman. *All of Statistics: A Concise Course in Statistical Inference*. Springer, New York, 2004.

[106] W. Krauth. Bethe ansatz for the one-dimensional boson Hubbard model. *Physical Review B*, 44:9772, 1991.

[107] T. D. Kühner, S. R. White, and H. Monien. One-dimensional Bose-Hubbard model with nearest-neighbor interaction. *Physial Review B*, 61:12474, 2000.

[108] P. Buonsante and A. Vezzani. Ground-State Fidelity and Bipartite Entanglement in the Bose-Hubbard Model. *Physical Review Letters*, 98:110601, 2007.

[109] J. K. Freericks and H. Monien. Strong-coupling expansions for the pure and disordered Bose-Hubbard model. *Physical Review B*, 53:2691, 1996.

[110] J. Dziarmaga. Dynamics of a quantum phase transition and relaxation to a steady state. *Advances in Physics*, 59:1063, 2010.

[111] J.-P. Onnela, J. Saramäki, J. Kertész, and K. Kaski. Intensity and coherence of motifs in weighted complex networks. *Physical Review E*, 71:065103, 2005.

[112] B. Zeng, X. Chen, D.-L. Zhou, and X.-G. Wen. *Quantum Information Meets Quantum Matter – From Quantum Entanglement to Topological Phase in Many-Body Systems*. Springer, New York. arXiv:1508.02595, 2015.

[113] W. Dür, G. Vidal, and J. I. Cirac. Three qubits can be entangled in two inequivalent ways. *Physical Review A*, 62:062314, 2000.

[114] V. Vedral. Quantum entanglement. *Nature Physics*, 10:256, 2014.

APPENDIX - CONTINUUM QUANTUM CELLULAR AUTOMATA

Directly below we place a derivation that allows us to rewrite the BCM Hamiltonian in terms of the activity term $\left(\hat{b}_i + \hat{b}_i^\dagger\right)$, and sums of powers of the total number of sites in the alive state in the neighborhood of site i, $\hat{T}_i \equiv \sum_{j\in N_i} \hat{n}_j$. Where $N_i \equiv \{i-2, i-1, i+1, i+2\}$. The BCM Hamiltonian is defined as,

$$\hat{H} = \sum_{i=3}^{L-2} \left(\hat{b}_i + \hat{b}_i^\dagger\right) \left(\hat{\mathcal{N}}_i^{(3)} + \hat{\mathcal{N}}_i^{(2)}\right) . \tag{A.1}$$

Where $\hat{\mathcal{N}}_i^{(2)}$ is the projection operator onto the subspace spanned by number eigen-states in which site i has two living neighbors. This is all permutations of $|\psi_{[1:i-3]}\rangle \otimes |0_{i-2}\rangle \otimes |0_{i-1}\rangle \otimes |1_{i+1}\rangle\, |1_{i+2}\rangle \otimes |\psi_{[i+3:L]}\rangle$. Where we permute the placement of the living sites in order to treat each site symmetrically. Similarly $\hat{\mathcal{N}}_i^{(3)}$ is the projection operator onto the subspace spanned by number eigen-states in which site i has three living neighbors. This is a projection on to the space spanned by all permutations of $|\psi_{[1:i-3]}\rangle \otimes |0_{i-2}\rangle \otimes |1_{i-1}\rangle \otimes |1_{i+1}\rangle\, |1_{i+2}\rangle \otimes |\psi_{[i+3:L]}\rangle$. Note that site i is purposefuly not included in the above tensor products. Explicitly,

$$\hat{\mathcal{N}}_i^{(2)} = \sum_\sigma \hat{\bar{n}}_{\sigma(i)} \hat{\bar{n}}_{\sigma(i-1)} \hat{n}_{\sigma(i+1)} \hat{n}_{\sigma(i+2)} \tag{A.2}$$

and

$$\hat{\mathcal{N}}_i^{(3)} = \sum_\pi \hat{\bar{n}}_{\pi(i)} \hat{n}_{\pi(i-1)} \hat{n}_{\pi(i+1)} \hat{n}_{\pi(i+2)} \, . \tag{A.3}$$

The sums over σ and π denote the sum over all permutations of the site indices and where $\hat{\bar{n}}_i = \hat{1} - \hat{n}_i$. This amounts to $\binom{4}{2} = 12$ terms for $\hat{\mathcal{N}}_i^{(2)}$, and $\binom{4}{3} = 4$ terms for $\hat{\mathcal{N}}_i^{(3)}$. I observe the remaining classical possibilities are zero, one, and four particles in the subset of sites $i-2, i-1, i+1, i+2$, so that we may express the identity operator as

$$\hat{1} = \hat{\mathcal{N}}_i^{(0)} + \hat{\mathcal{N}}_i^{(1)} + \hat{\mathcal{N}}_i^{(2)} + \hat{\mathcal{N}}_i^{(3)} + \hat{\mathcal{N}}_i^{(4)} \tag{A.4}$$

$$\Rightarrow \hat{\mathcal{N}}_i^{(2)} + \hat{\mathcal{N}}_i^{(3)} = \hat{1} - (\hat{\mathcal{N}}_i^{(0)} + \hat{\mathcal{N}}_i^{(1)} + \hat{\mathcal{N}}_i^{(4)}) \tag{A.5}$$

$$= \hat{1} - (\hat{\bar{n}}_{i-2}\hat{\bar{n}}_{i-1}\hat{\bar{n}}_{i+1}\hat{n}_{i+2} + \hat{\bar{n}}_{i-2}\hat{\bar{n}}_{i-1}\hat{n}_{i+1}\hat{\bar{n}}_{i+2} + \tag{A.6}$$

$$\hat{\bar{n}}_{i-2}\hat{n}_{i-1}\hat{\bar{n}}_{i+1}\hat{\bar{n}}_{i+2} + \hat{n}_{i-2}\hat{\bar{n}}_{i-1}\hat{\bar{n}}_{i+1}\hat{\bar{n}}_{i+2}) - \hat{n}_{i-2}\hat{n}_{i-1}\hat{n}_{i+1}\hat{n}_{i+2} \tag{A.7}$$

Rewriting this solely in terms of the $\hat{n}$ operators and noting that $[\hat{n}_i, \hat{n}_j] = 0$ results in,

$$\hat{\mathcal{N}}_i^{(2)} + \hat{\mathcal{N}}_i^{(3)} = \sum_{k<j}\sum_{j\in N_i} \hat{n}_k\hat{n}_j - 2\sum_{\ell<k}\sum_{k<j}\sum_{j\in N_i} \hat{n}_\ell\hat{n}_k\hat{n}_j + 2\hat{n}_{i-2}\hat{n}_{i-1}\hat{n}_{i+1}\hat{n}_{i+2} \tag{A.8}$$

Observing that $\hat{n}_i^2 = \hat{n}_i$ leads to the following equation

$$(\hat{n}_i + \hat{n}_j)^2 = \hat{n}_i^2 + 2\hat{n}_i\hat{n}_j + \hat{n}_j^2 = \hat{n}_i + 2\hat{n}_i\hat{n}_j + \hat{n}_j\,. \tag{A.9}$$

This equation generalizes to

$$\left(\sum_{j\in N_i}\hat{n}_j\right)^2 = \sum_{j\in N_i}\hat{n}_i^2 + 2\sum_{k<j}\sum_{j\in N_i}\hat{n}_k\hat{n}_j = \sum_{j\in N_i}\hat{n}_j + 2\sum_{k<j}\sum_{j\in N_i}\hat{n}_k\hat{n}_j\,. \tag{A.10}$$

This implies

$$\sum_{k<j}\sum_{j\in N_i}\hat{n}_k\hat{n}_j = \frac{1}{2}\left[\left(\sum_{j\in N_i}\hat{n}_j\right)^2 - \sum_{j\in N_i}\hat{n}_j\right]\,. \tag{A.11}$$

Furthermore, since

$$\left(\sum_{j\in N_i}\hat{n}_j\right)^3 = \left[\left(\sum_{j\in N_i}\hat{n}_j\right)^2 + \left(2\sum_{k<j}\sum_{j\in N_i}\hat{n}_k\hat{n}_j\right)\sum_{j'\in N_i}\hat{n}_{j'}\right] \tag{A.12}$$

$$= 4\sum_{k<j}\sum_{j\in N_i}\hat{n}_k\hat{n}_j + 6\sum_{l<k}\sum_{k<j}\sum_{j\in N_i}\hat{n}_l\hat{n}_k\hat{n}_j\,. \tag{A.13}$$

We have

$$\sum_{l<k}\sum_{k<j}\sum_{j\in N_i}\hat{n}_l\hat{n}_k\hat{n}_j = \frac{1}{6}\left[\left(\sum_{j\in N_i}\hat{n}_j\right)^3 - 3\left(\sum_{j\in N_i}\hat{n}_j\right)^2 + 2\sum_{j\in N_i}\hat{n}_j\right]\,. \tag{A.14}$$

Finally, a similar calculations lead to the following equation

$$\sum_{m<l}\sum_{l<k}\sum_{k<j}\sum_{j\in N_i}\hat{n}_m\hat{n}_l\hat{n}_k\hat{n}_j = \tag{A.15}$$

$$= \frac{1}{24}\left[\left(\sum_{j\in N_i}\hat{n}_j\right)^4 - 6\left(\sum_{j\in N_i}\hat{n}_j\right)^3 + 11\left(\sum_{j\in N_i}\hat{n}_j\right)^2 - 6\sum_{j\in N_i}\hat{n}_j\right]. \tag{A.16}$$

We define

$$\hat{T}_i \equiv \sum_{j\in N_i}\hat{n}_j\,, \tag{A.17}$$

$$D_2^i \equiv \sum_{k<j}\sum_{j\in N_i}\hat{n}_k\hat{n}_j\,, \tag{A.18}$$

$$D_3^i \equiv \sum_{l<k}\sum_{k<j}\sum_{j\in N_i}\hat{n}_l\hat{n}_k\hat{n}_j\,, \tag{A.19}$$

and

$$D_4^i \equiv \sum_{m<l}\sum_{l<k}\sum_{k<j}\sum_{j\in N_i}\hat{n}_m\hat{n}_l\hat{n}_k\hat{n}_j\,. \tag{A.20}$$

We can write a succint set of formulas

$$D_2^i = \frac{1}{2}\left(\hat{T}_i^2 - \hat{T}_i\right)\,, \tag{A.21}$$

$$D_3^i = \frac{1}{6}\left(\hat{T}_i^3 - 3\hat{T}_i^2 + 2\hat{T}_i\right)\,, \tag{A.22}$$

$$D_4^i = \frac{1}{24}\left(\hat{T}_i^4 - 6\hat{T}_i^3 + 11\hat{T}_i^2 - 6\hat{T}_i\right)\,. \tag{A.23}$$

This allows us to rewrite the quantum game of life Hamiltonian as

$$\hat{H} = \frac{1}{3}\sum_{i=3}^{L-2}\left(\hat{b}_i + \hat{b}_i^\dagger\right)\left[-5\hat{T}_i + \frac{29}{4}\hat{T}_i^2 - \frac{5}{2}\hat{T}_i^3 + \frac{1}{4}\hat{T}_i^4\right] \tag{A.24}$$

$$= \frac{1}{12}\sum_{i=3}^{L-2}\left(\hat{b}_i + \hat{b}_i^\dagger\right)\left(\hat{T}_i - 5\right)\left(\hat{T}_i - 4\right)\left(\hat{T}_i - 1\right)\hat{T}_i\,. \tag{A.25}$$

This Hamiltonian naturally suggests the following generalized form

$$\hat{H} = \sum_{i=3}^{L-2}\left(\hat{b}_i + \hat{b}_i^\dagger\right)f(\hat{T}_i)\,. \tag{A.26}$$

as well as a simplification of the Hamiltonian that is more true to the game of life, namely the polynomial $t(1-t)(4-t)$. This rule treats a total number of particles equal to 2 differently than it treats a total number of particles equal to 3. This may be one direction for future study. The operators $\hat{T}_i$ only have integer eigenvalues, $\lambda_i \in \{0, 1, 2, 3, 4\}$. However in Fig. A.1 we plot continuous polynomials as this suggests another direction for future study, continuous QCA. One may consider writing down a set of non-linear Schrödinger type equations in a mean field approximation. The function f described in Fig. A.1 refers to the polynomial of Equation (A.24).

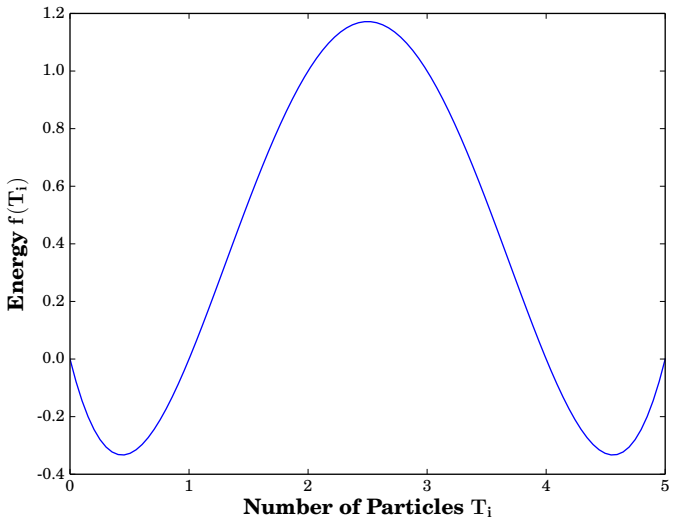

Fig. A.1: *Polynomial of quantum game of life rule.* The operator $\hat{T}_i$ has strictly integer eigenvalues, all of which are smaller than five. None-the-less, the quantum game of life Hamiltonian references outside of this interval implicitly in its definition, since we see that one term in the Hamiltonian is of the form $(\hat{T}_i - 5)$.